Novel Methods for Enhanced Free Electron Laser Output

PhD Thesis

Jenny Morgan

Department of Physics

University of Strathclyde, Glasgow

Cockcroft Institute, Daresbury

August 4, 2021

This thesis is the result of the author's original research. It has been composed by the author and has not been previously submitted for examination which has led to the award of a degree.

Signed:

Date:

Abstract

An emerging area of free electron laser development concerns tailoring the transverse and phase profile of the light, which can result in the radiation acquiring orbital angular momentum. This thesis studies the development of novel techniques for free electron lasers with consideration of the generation of higher-order orbital angular momentum modes acting as a starting point for this research. Three new techniques are presented in this thesis. The first examines altering mode competition in a free electron laser to induce radiation of a dominant orbital angular momentum mode. The next is a scheme to produce light with spatially varying states of polarisation - obtained through the overlap of different coherent transverse light distributions. The third technique produces trains of short radiation pulses where the properties of the pulses alternate. The goal of this research is to increase the diversity of radiation from free electron lasers in order to offer something new and unlock new areas of scientific research.

Preface/Acknowledgements

Many thanks to my supervisor Brian M^{c}Neil for his guidance and patience throughout this process. Thanks to the Strathclyde Strategic Parnership funding and STFC Grant Science and Technology Facilities Council for providing funding. I also thank Alison Yao for her time. Thanks must go to Erik Hemsing for welcoming me when I visited SLAC and his support and collaboration on much of the work contained in this thesis.

Love and gratitude go to my family for their support and encouragement throughout my life and studies. Finally, to Ramsay - thank you for everything.

Contents

List of Figures

List of Figures

List of Tables

List of Tables

Chapter 1

Introduction

Free electron lasers, FELs, provide radiation with properties that are not available through alternative sources. FELs are widely tuneable devices operating at wavelengths that range from microwaves to x-rays. FELs operating at x-ray wavelengths, notably, provide x-ray radiation which is billions of times brighter and thousands of times shorter than other x-ray sources [1]. The development of these radiation sources has had a significant impact on research capabilities, driving progress in numerous scientific areas, from imaging to studying matter in extreme conditions [2].

It has been just over a decade since the first successful demonstration of x-ray FELs [3], in which time FEL technology has seen significant advancement allowing FEL operation at ever increasing brightness and powers as well as shortening wavelengths. Techniques that customise the FEL output have been and continue to be developed, including control over the polarisation of the light [4], ultra-short pulse generation [5] and multi-colour operation [6]. There is much interest in tailoring the FEL output to new exotic regimes with the expectation that this will enable new scientific research.

This thesis presents novel FEL techniques which further diversify FEL radiation with an emphasis on the tailoring of the transverse intensity and phase profile of the light, which can result in the radiation acquiring Orbital Angular Momentum, OAM. The current literature demonstrating OAM generation in a FEL is covered in Chapter 4 and acts as a starting point for the new research in this thesis.

1.1 Thesis Outline

The subsequent sections of this chapter are used to give a brief outline of FEL operation followed by an historical overview of the development of FELs. Chapters 2-4, introduce the physics on which this thesis is based. New research is included in Chapters 5-7 where three novel FEL techniques are presented. A summary of each chapter is now included.

Chapter 2 sets out the basic theory of FELs. The chapter starts by deriving the motion of a single electron propagating through an undulator with a given magnetic field. The path of the electrons determines the properties of the radiation spontaneously emitted by the electron. Using the derived motion of an electron, the resonant wavelength is derived and the spectrum of emission is discussed. The FEL equations are then derived in this chapter and used to form a description of the underlying FEL mechanisms.

Chapter 3 develops an introduction to the physics of light which carries orbital angular momentum. The Laguerre-Gaussian and Hermite-Gaussian modes are introduced in this chapter as solutions to the paraxial wave equation.

Chapter 4 reviews existing methods for the generation of FEL radiation which carries orbital angular momentum. The off-axis harmonic emission from helical undulators is investigated and shown to carry orbital angular momentum.

Chapter 5 investigates a scheme to produce light with orbital angular momentum at the fundamental wavelength of the undulator. It is demonstrated - using FEL simulations - that selected longitudinal and transverse-rotational shifts repeated between the FEL's undulator sections will a cause dominant orbital angular momentum mode to self-select for amplification.

Chapter 6 presents a scheme where the higher-order transverse modes emitted in harmonic undulator radiation are superimposed to generate light where the polarisation state of the radiation varies transversely across the photon beam. Beams with structured polarisation are called Poincaré beams; a theoretical description of this light

is developed and FEL simulations are presented.

Chapter 7 presents a method for generating pulse trains where the properties of the pulses alternate. This is demonstrated for a pulse train with alternating orthogonal linear or circular polarisation. The chapter concludes with a discussion of how this can be adapted to create pulse trains where the pulse trains carry OAM with alternating handedness.

Chapter 8 concludes the thesis and discusses future work.

Appendix A lists the publications arising from the work contained in this thesis.

1.2 FEL Operation

When a relativistic charged particle's path is altered by a magnetic field it will radiate electromagnetic radiation which is termed synchrotron radiation. There are many light sources that use this effect to provide researchers with radiation over a wide range of wavelengths. The free electron laser, FEL, is one of these sources which converts the energy from a relativistic electron beam into electromagnetic radiation.

FELs pass relativistic electron beams through a periodic magnetic field from a magnetic undulator or wiggler. Simple undulator designs are planar and helical undulators; these undulators cause electrons propagating through them to travel a sinusoidal or helical path. The transverse oscillations of the electrons in the undulator induce radiation emission from the electrons. Since the electrons travel at relativistic velocity, the wavelength of the forward emission from electrons is contracted. This effect is called Doppler frequency shifting, where the frequency of the light being observed is higher than the frequency of light being emitted. The frequency up-shifting allows FELs to generate radiation at wavelengths as short as hard x-rays; current facilities operate at wavelengths as short as 0.5Å [7].

Near the start of the undulator, the radiation emitted after multiple undulator periods is monochromatic, however, since the electrons are randomly distributed in the electron beam, the light is not coherent and therefore low energy. Coherence in a FEL is achieved by a positive feedback process between the electrons and the radiation. As the electrons are travelling close to the speed of light, they co-propagate with the radiation

field and interact with the field via electrons' transverse oscillations. This interaction causes the electrons to exchange energy with the field. There is a modulation of the electron beam energy where some electrons then gain and some lose energy. As the electrons propagate, the energy modulation is converted to density modulation at the scale of the radiation wavelength, which is termed micro-bunching. The electrons are periodically grouped together which causes them to emit with greater coherence as illustrated in Figure 1.1. There is a self-consistent process: as the electrons bunch together the intensity of the light they radiate grows, which in turn increases the micro-bunching.

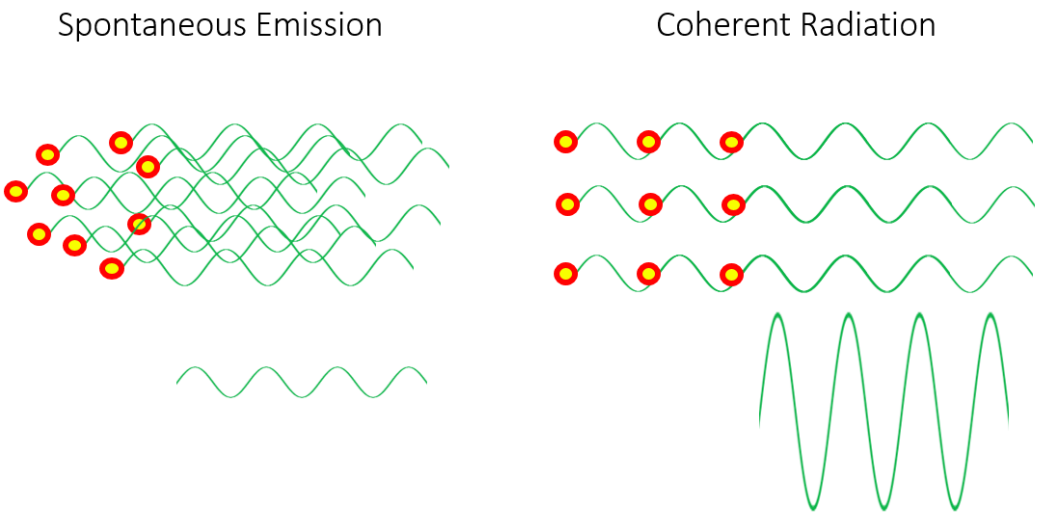

Figure 1.1: Schematic showing how self-organisation of the electrons leads to amplification of the radiation. Left: electrons are randomly distributed and the radiation emitted is low intensity. Right: electrons are micro-bunched at the resonant wavelength. The radiation emitted is coherent and constructively interferes and is therefore high intensity.

The self-organisation of electrons enables FELs to generate x-ray pulses many times brighter than other synchrotron radiation, with multi-GW peak powers. The wavelength of the FEL is controlled by changing either the electron energy, undulator period or undulator magnetic field strength. This makes FELs easily tunable, with current shorter wavelength facilities operating from the VUV down to hard x-rays [3, 8–12].

The radiation output is typically a transverse Gaussian mode with nearly full transverse coherence and a spatially homogeneous polarisation that is determined by the magnetic undulator fields.

1.3 History of FELs

1.3.1 Synchrotron Radiation

Predating the FEL is the synchrotron light source which utilises the radiation emitted by high energy electrons as they circulate in a synchrotron. Originally developed for nuclear physics research, synchrotrons accelerate electrons in a large ring. In 1947, white light from electrons travelling through a bend in a synchrotron at General Electric Research Laboratory [13] was the first observed case of radiating electrons, hence naming the radiation from relativistic electrons - synchrotron radiation. This radiation was originally seen as a negative as it causes the electrons to lose energy, limiting the maximum electron energy achievable with the accelerators. In the 1960s, the experimental possibilities of synchrotron radiation were recognised and facilities began to allow access to users wanting to exploit the radiation for scientific research. The quality of the radiation produced advanced quickly as facilities transitioned from utilising light from electrons travelling around a bend to inserting undulators and wigglers in the straight sections between the bends.

Synchrotron light sources are a useful source of V-UV and x-ray radiation which are currently in use all over the world. The light produced by this source is incoherent, which is useful for many applications, however, some experiments ask for a coherent source of x-ray radiation. The development of the x-ray FEL reached the long sought after goal of generating coherent x-ray radiation, improving the properties of synchrotron sources by orders of magnitude.

1.3.2 Development of the Free Electron Laser

Moltz [14] first proposed inducing radiation emission from an electron moving through a stationary electric or magnetic field with undulating polarity, describing the Doppler

frequency shift that would result from shifting from the moving frame of the high energy electron to the laboratory frame. Moltz then demonstrated generating incoherent light at visible and millimeter wavelengths from undulator experiments at Stanford [15]. Many of the key FEL ideas were demonstrated by Phillips, who introduced an undulator source to generate microwaves called a ubitron [16]. However, the device used low energy electron beams and therefore did not produce a significant Doppler frequency shift.

It is Madey who is credited with the invention of the FEL. Madey published his original quantum description of the FEL in 1971, suggesting that such a system could be used to produce coherent x-ray radiation. The first low gain amplification of an external seed [17] was subsequently demonstrated by Madey and colleagues followed by demonstrating lasing in a FEL oscillator system [18].

A significant breakthrough was made, simplifying the analysis of FELs, when it was demonstrated that the FEL could be described by classical physics in addition to the previous quantum approach. Two major contributors to the classical theory of FELs are Colson [19] and Hopf *et al.* [20]. Colson's work described the low gain FEL regime where the FEL can be described by coupled differential equations equivalent to the pendulum equations. Hopf *et al.* concluded that the FEL is a completely classical problem and the amplification previously attributed to the Compton recoil is actually due to electron bunching. The classical description provides a good approximation of the FEL at wavelengths as short as hard x-rays. At wavelengths as short as gamma rays, however, the quantum contribution, namely the electron recoil, impedes the FEL process.

With the FEL now described classically, the theory of the high gain FEL was developed through multiple works [21–25]. The high gain regime allows exponential amplification of the FEL in a single pass of the electron beam through the undulator. This removed the need for mirrors which create an oscillator cavity and allowed the FEL to move towards x-ray wavelengths. It was also shown that the exponential gain of the FEL could be started by a small source such as the noise in an electron beam. This also increased the wavelength range possible with a FEL by removing the need

for an initial seed laser.

1.3.3 Current Facilities

The high gain FEL was demonstrated at first at microwaves [26] then, starting from noise, in the infrared and visible spectral regions [27, 28]. The first VUV/soft x-ray FEL, FLASH [8], was completed in 2005; operating at wavelengths in the range 6.5 to 50nm.

LCLS, the world's first hard x-ray FEL, is powered by the SLAC linear accelerator. The accelerator was originally conceived as a discovery machine for particle physics and had spent most of its life being used to explore subatomic particles, but in the early 2000s the final third of the linac was repurposed to provide relativistic electors for the x-ray FEL. First lasing of LCLS was observed at a wavelength of 1.5 Å in 2009 [3].

Following LCLS, many more hard x-ray FEL facilities have been established, including the European XFEL at DESY in Germany [29], SACLA in Japan [9], SwissFEL in Switzerland [30] and PAL-XFEL in South Korea [31]. The development of Hard x-ray FELs marked a significant advancement in research capabilities and have been and continue to be utilised in numerous research areas including atomic and molecular physics, chemistry, biology and matter in extreme conditions.

FEL technology continues to evolve and facilities such as LCLS are upgrading in order to keep up with scientific demand [32], *e.g.* to meet the need for higher rep rates. There is also a push to establish new facilities, for example, the proposed UKXFEL [7], which hopes to offer capabilities beyond what is possible today.

Chapter 2

FEL Theory

This chapter looks at FEL theory in greater detail than Section 1.2. Starting with the motion of electrons in an undulator, the resonance condition and FEL equations are derived and the main FEL mechanisms are discussed.

2.1 Electron Trajectory Through the Undulator

Considered first is the trajectory of an electron propagating through the magnetic undulator, which ultimately determines the properties of the undulator radiation. The electron enters and travels through the undulator with a relativistic velocity along the z-axis. The electron experiences a force from the undulator's transverse magnetic field which accelerates the electron transversely - altering its path and inducing radiation emission.

The radiation field's effect on the electron's motion is small compared to the motion due to the magnetic undulator and is ignored for the moment. The Lorentz force on an electron in the absence of a radiation field ($\boldsymbol{E} = 0$) is

$$\boldsymbol{F} = -e(c\boldsymbol{\beta} \times \boldsymbol{B}), \tag{2.1}$$

where $e = |e|$ is the electron charge, $c\boldsymbol{\beta}$ is the electron's velocity and c is the speed of light.

2.1.1 Helical Undulator

On-axis, the magnetic field from a helical undulator with period λ_u can be expressed as

$$\boldsymbol{B} = B_0(\cos(k_u z)\hat{\boldsymbol{e}}_{\boldsymbol{x}} \mp \sin(k_u z)\hat{\boldsymbol{e}}_{\boldsymbol{y}} + 0\hat{\boldsymbol{e}}_z), \tag{2.2}$$

where B_0, $k_u = 2\pi/\lambda_u$ and $\hat{\boldsymbol{e}}_{\boldsymbol{x,y,z}}$ are, respectively, the maximum magnetic field amplitude, the undulator wavenumber and unit vectors pointing in the x, y and z directions. The upper sign refers to a left-handed undulator and the lower sign refers to a right-hand undulator.

Equation (2.2) gives the magnetic field on-axis ignoring the off-axis variation. This expression for the field does not satisfy Maxwell's equations for a static magnetic field; notably $\nabla \times B = 0$ is not satisfied. A physical description of the field which does satisfy Maxwell's equations includes a longitudinal component which is zero on-axis but non-zero off-axis. Equation (2.2) therefore provides an adequate description of the undulator's magnetic field despite violating Maxwell's equations, provided that the electrons propagate close to the longitudinal axis.

The force is the rate of change of momentum,

$$\boldsymbol{F} = \frac{\mathrm{d}\boldsymbol{p}}{\mathrm{d}t}, \tag{2.3}$$

where the relativistic momentum $\boldsymbol{p} = \gamma m_0 c\boldsymbol{\beta}$ with $\gamma = (1-\beta^2)^{-1/2}$ and m_0 the rest mass of the electron. The distance along the undulator axis, z, can be exchanged with the variable time, t though the transform $\mathrm{d}t = 1/(c\beta_z)\mathrm{d}z$. On the right-hand side of the Lorentz force equation, the cross product gives $\boldsymbol{\beta} \times \boldsymbol{B} = -\beta_z B_y \hat{\boldsymbol{e}}_{\boldsymbol{x}} + \beta_z B_x \hat{\boldsymbol{e}}_{\boldsymbol{y}} + (\beta_x B_y - \beta_y B_x)\hat{\boldsymbol{e}}_{\boldsymbol{z}}$. Taking only the transverse components first, gives

$$\frac{\mathrm{d}\boldsymbol{\beta}_\perp}{\mathrm{d}z} = -\frac{eB_0}{cm_0\gamma}(\pm\sin(k_u z)\hat{\boldsymbol{e}}_{\boldsymbol{x}} + \cos(k_u z)\hat{\boldsymbol{e}}_{\boldsymbol{y}}). \tag{2.4}$$

Integration with respect to z finds the transverse velocity component

$$\boldsymbol{\beta}_\perp = \frac{K}{\gamma}(\pm\cos(k_u z)\hat{\boldsymbol{e}}_{\boldsymbol{x}} - \sin(k_u z)\hat{\boldsymbol{e}}_{\boldsymbol{y}}), \tag{2.5}$$

where the undulator parameter K is introduced as

$$K = \frac{eB_0}{m_0 c k_u}. \tag{2.6}$$

The electron travels a helical path in the undulator, completing one orbit every undulator period λ_u. The helical path taken by one electron in a left-handed undulator is shown in Figure 2.1 . The magnetic field from a right-handed undulator will reverse the transverse direction of the particle.

Evaluation of the $\hat{\boldsymbol{e}}_{\boldsymbol{z}}$ component of the Lorentz force equation using the transverse velocity components shows $\mathrm{d}\beta_z/\mathrm{d}z = 0$. The electron therefore travels at a constant velocity $c\beta_z$ along the z-axis. β_z can be derived from

$$\frac{1}{\gamma^2} = 1 - (\beta_x^2 + \beta_y^2 + \beta_z^2), \tag{2.7}$$

to show

$$\beta_z = 1 - \frac{1 + K^2}{2\gamma^2}. \tag{2.8}$$

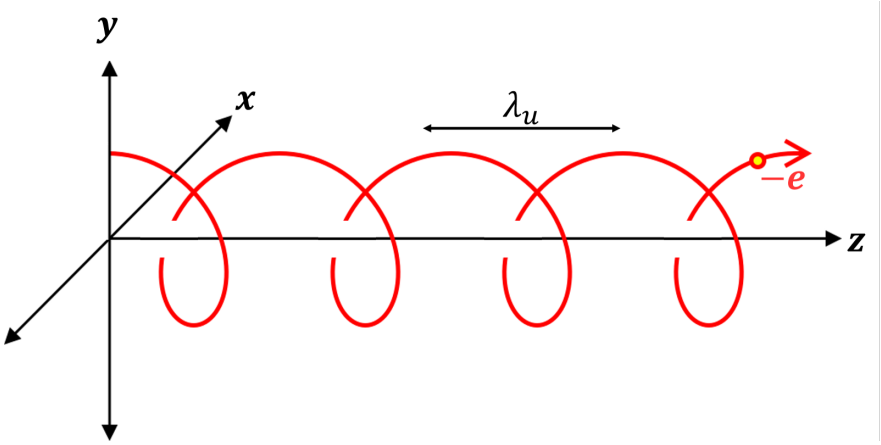

Figure 2.1: An electron propagating through a helical undulator spirals along the z-axis.

2.1.2 Planar Undulator

The planar undulator case is now considered. The planar undulator has a magnetic field only in one of either the x or y direction as opposed to the helical undulator with magnetic field components in both directions. Choosing the magnetic field to be in the x-direction, near the axis the field is described as

$$\boldsymbol{B} = B_0 \cos(k_u z)\hat{\boldsymbol{e}}_{\boldsymbol{x}} + 0\hat{\boldsymbol{e}}_{\boldsymbol{y}} + 0\hat{\boldsymbol{e}}_z. \tag{2.9}$$

An electron travelling through this magnetic field will oscillate in the y-direction with velocity

$$\beta_y = \frac{K}{\gamma}\sin(k_u z). \tag{2.10}$$

There is no oscillation in the x-direction, $\beta_x = 0$. From equation 2.7, the longitudinal is given by

$$\beta_z^2 = 1 - \frac{1}{\gamma^2} - \frac{K^2}{\gamma^2}\sin^2(k_u z). \tag{2.11}$$

Propagating in a planar undulator, the electrons oscillate along z at twice the frequency of the transverse oscillation. This gives rise to odd harmonics on-axis. There is no z dependence on β_z in the helical undulator case and therefore no on-axis harmonics. Off-axis harmonics arise in both cases which is discussed later.

Averaging the z oscillation over an undulator period finds the average longitudinal velocity

$$\bar{\beta}_z = \sqrt{1 - \frac{1}{\gamma^2} - \frac{K^2}{2\gamma^2}}. \tag{2.12}$$

Since $1/\gamma^2 \ll 1$ the approximation $(1-x)^n \simeq 1 - nx$ can be applied to give

$$\bar{\beta}_z \simeq 1 - \frac{1}{2\gamma^2}\left(1 + \frac{K^2}{2}\right). \tag{2.13}$$

This result will be used later when calculating the resonance condition for the radiation.

The path of the electrons in a planar undulator is shown in Figure 2.2. Since the maximum deflection angle, θ_{max}, from the undulator axis is small it can be found using

the approximation $\beta_{x,max}/\beta = \sin(\theta) \simeq \theta$ where $\beta_{x,max} = K/\gamma$ and $\beta \simeq 1$ to give

$$\theta_{max} = \frac{K}{\gamma}. \tag{2.14}$$

The K parameter then defines the deflection angle scaled to the electron energy.

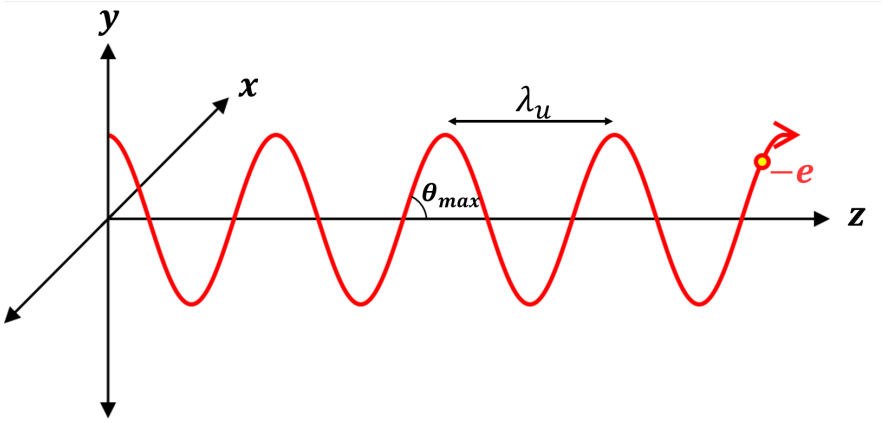

Figure 2.2: An electron propagating through a planar undulator takes a sinusoidal path along the z-axis with oscillations perpendicular to the magnetic field.

2.2 Resonance Condition

With the electron trajectory known, the radiation emitted can now be considered. A primary consideration is the wavelength of the light emitted. As electrons are particles with mass, their velocity is close to but less than the speed of light. The transverse motion, due to the undulator, further decreases an electron's longitudinal velocity. This means the electrons slip backwards relative to the radiation field. This slippage determines the wavelength of radiation. Over many undulator periods, in order for radiation emitted to constructively interfere, it must be phase matched to the electron trajectory. Wavelengths that are phase matched must slip ahead of an electron an integer number of wavelengths every undulator period. By equating the time of flight, $t_e = \lambda_u/c\bar{\beta}_z$, for one electron to travel one undulator period with the time, $t_r = (\lambda_u + h\lambda_h)/c$, for the radiation to travel one undulator period plus an integer number,

h, of resonant wavelengths, λ_h, the resonance condition can be derived as follows,

$$\frac{\lambda_u + h\lambda_h}{c} = \frac{\lambda_u}{\bar{\beta}_z c}, \tag{2.15}$$

$$\lambda_h = \frac{\lambda_u}{h}\left(\frac{1-\bar{\beta}_z}{\bar{\beta}_z}\right). \tag{2.16}$$

The longitudinal velocity was derived above for a helical undulator, equation (2.1), and the planar undulator, equation (2.13). The longitudinal velocity in a planar undulator has a factor of $1/2$ associated with the K^2 term not present in the expression for the helical undulator case. When substituting longitudinal velocity into the expression for resonant wavelength it is then convenient to use the rms undulator parameter, a_u, instead of K to give

$$\lambda_h = \frac{\lambda_u}{2h\gamma^2}(1 + a_u^2). \tag{2.17}$$

a_u is defined in terms of the rms magnetic field instead of the peak field used to define K. For a helical undulator $a_u = K$ and for a planar undulator $a_u = K/\sqrt{2}$. Helical and planar undulator with the same a_u will delay the electrons by the same amount, ensuring the resonance condition is the same for different undulator types when expressed in terms of a_u.

Equation (2.17) only holds for on-axis radiation. Further examination of the time of flight for radiation emitted off-axis as shown in Figure 2.3 modifies the resonance condition to

$$\lambda_h = \frac{\lambda_u}{2h\gamma^2}(1 + a_u^2 + \theta^2\gamma_r^2). \tag{2.18}$$

This equation for the resonant wavelengths demonstrates the tunability of a FEL. The wavelength of a FEL can be adjusted by changing the resonant energy, undulator period and undulator strength. The integer, h, gives the harmonics of the fundamental wavelength, λ_1. In the next section, further analysis will show that different undulators will have different frequency spectrums and not all of the harmonics are emitted on-axis.

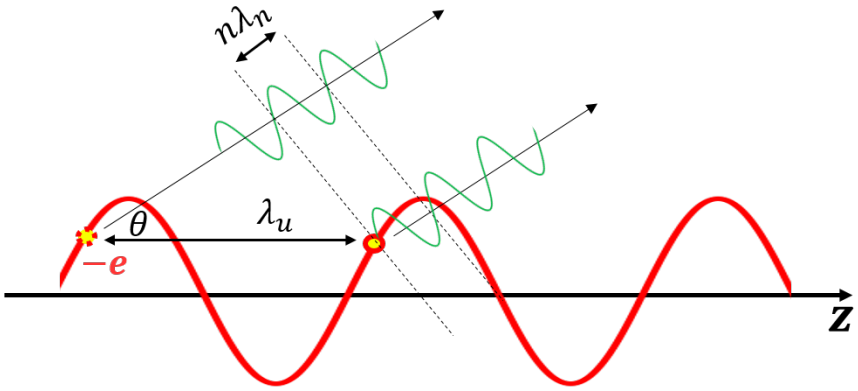

Figure 2.3: Illustration of the condition of resonance. Frequencies that do not slip ahead of an electron beam by an integer number of wavelengths every undulator period experience destructive interference. The resonance condition can be found by equating the time for an electron to travel an undulator period with the time for the light to travel the distance $n\lambda_n + \lambda_u \cos(\theta)$ where θ is the emission angle.

2.3 Interference of Spontaneous Emission

For relativistic energies, $\gamma \gg 1$, the radiation emitted by the electrons is primarily confined to a cone with a half opening angle $\sim \frac{1}{\gamma}$ about the actual path. It is now seen that the previously introduced parameter K, equation (2.1.2), which gave a measure of the deflection angle is important for determining the radiation spectrum. The K parameter then determines the distinction between a wiggler and an undulator where $K \approx 1$ is the boundary above which the magnetic device is referred to as a wiggler. The wiggler spectrum has fewer interference effects than the undulator though strong interference effects may still be notable up to $K \sim 10$. These effects have led to a modern definition of an undulator as a device where the spectral brightness scales with the square of the undulator periods.

Wiggler ($K \gg 1$)

If $K \gg 1$ then the deflection angle of the electron is larger than the cone of radiation emission, $\theta_{max} \gg \frac{1}{\gamma}$. This means an observer on-axis will only receive radiation emitted in a small window of the electron trajectory near the extrema of the electron transverse motion as shown in Figure 2.4. The on-axis electric field observed consists of equally

spaced electric field peaks with alternating polarity. Photons with energies at even harmonics of the resonant frequency arrive out of phase and destructively interfere - there is no even harmonic emission on-axis. The Fourier transform of the field gives the radiation spectrum featuring only odd harmonics. A larger K will produce sharper electric field peaks which results in a larger number of harmonics.

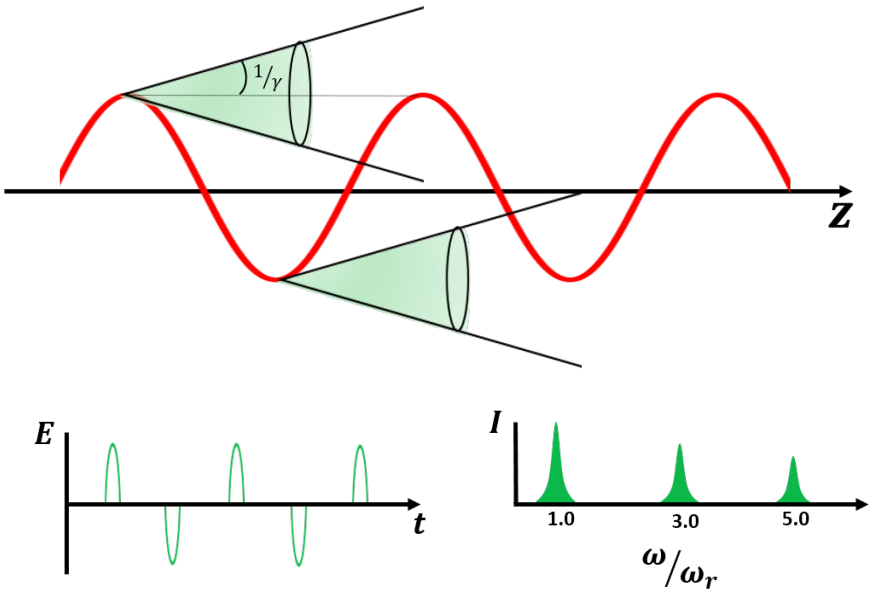

Figure 2.4: Top: The electron path (red) and radiation emitted (green) in a wiggler where $K \gg 1$. Radiation is emitted into a narrow cone of angle $\sim \frac{1}{\gamma}$. On-axis an observer will only revive photons from parts of the electron trajectory near the extrema of electron motion. Bottom: Illustration of the typical time dependence for the electric field on-axis (left) shows the electric field peaks are equally spaced with opposite polarity. Fourier transform of the field produces the frequency spectrum (right) with odd harmonics of the fundamental frequency.

Undulator ($K \leq 1$)

If K is decreased, more parts of the electron trajectory contribute to the radiation field, reducing the intensity and number of the higher harmonics. When $K \leq 1$, radiation emitted at all parts of the electrons trajectory interfere. For $K \ll 1$, the electron trajectory is negligible compared to the angular deviation and the almost coherent su-

perposition from all parts of the trajectory leads to a continuous sinusoidal electric field and the spectrum consists of only the fundamental frequency as shown in Figure 2.5.

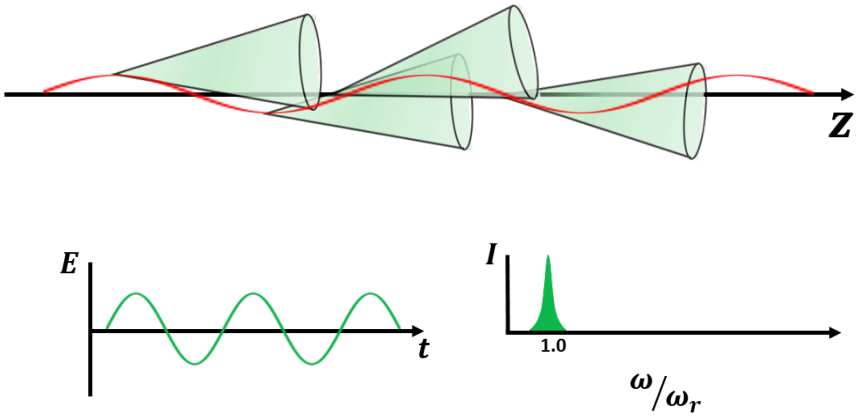

Figure 2.5: Top: The electron path (red) and radiation emitted (green) in an undulator where $K \leq 1$ and radiation from all parts of the electron trajectory interfere. Bottom: For $K \ll 1$ the electric field (left) approaches a continuous sin function and the Fourier transform gives a radiation spectrum (right) with only the fundamental frequency.

For the case of the helical undulator, the electron orbits its propagation axis with a constant radius. For a helical undulator, all parts of the radiation, in particular those from higher harmonics, are off-axis but only the fundamental radiates on-axis.

Off-axis spontaneous emission

Off-axis the spectrum is different. The electric field spikes are no longer evenly spaced and the even harmonics survive. Different positions away from the optical axis receive radiation from different parts of the electron trajectory. This results in a transverse phase variation in the off-axis harmonic radiation - an important consequence exploited in the work contained in this thesis. Further discussion of the off-axis radiation properties is found in Chapter 4.

2.4 The FEL Interaction

2.4.1 Energy Exchange

Section 2.1 described the motion of an electron propagating through an undulator in the absence of a radiation field. Now, the transfer of energy between the electron and a co-propagating radiation field is considered. The radiation is either spontaneous radiation generated by the electrons or can be injected into the undulator from an external source. Consider an electron interacting in a right-handed helical undulator with radiation that is circularly polarised and has spin in the same direction as the electron motion.

A plane circularly polarised electromagnetic field is described by

$$\boldsymbol{E} = E_0(\sin(k_r z - \omega_r t + \phi_r)\hat{\boldsymbol{e}}_{\boldsymbol{x}} + \cos(k_r z - \omega_r t + \phi_r)\hat{\boldsymbol{e}}_{\boldsymbol{y}}), \tag{2.19}$$

where E_0 is the field amplitude. $k_r = 2\pi/\lambda$, ω_r and ϕ_r are, respectively, the wavenumber, angular frequency and phase. The Lorentz force, now including the electric field, is

$$\boldsymbol{F} = -e(\boldsymbol{E} + c\boldsymbol{\beta} \times \boldsymbol{B}). \tag{2.20}$$

The electric field couples with the transverse electron motion. The corresponding change in energy is found by taking the scalar product of both sides of the Lorentz force equation with the transverse velocity, $\boldsymbol{\beta}_\perp$ from equation 2.5. The magnetic field does not couple and exchange energy with the electron as $(c\boldsymbol{\beta} \times \boldsymbol{B}) \cdot \boldsymbol{\beta}_\perp = 0$. This leaves

$$mc\frac{\mathrm{d}\gamma}{\mathrm{d}t} = -e\boldsymbol{E} \cdot \boldsymbol{\beta}_\perp = \frac{eK}{\gamma}E_0 \sin((k_r + k_u)z - \omega_r t + \phi_r). \tag{2.21}$$

The exchange of energy can be positive or negative depending on the electron's position relative to the phase of the wave on the right-hand side of equation (2.20) which is known as the pondermotive wave. If $\frac{\mathrm{d}\gamma}{\mathrm{d}z} > 0$, the electron gains energy from the field and for $\frac{\mathrm{d}\gamma}{\mathrm{d}z} < 0$, the electron gives energy to the radiation field, increasing the radiation field amplitude. The many electrons making up an electron beam will have different positions and some electrons will gain energy while others will lose energy.

There is a continuous exchange in energy between an electron and the field if the electron velocity matches the phase velocity of the pondermotive wave and therefore

$$\frac{\mathrm{d}\theta}{\mathrm{d}t} = 0, \tag{2.22}$$

where

$$\theta = (k_r + k_u)z - \omega_r t + \phi_r \tag{2.23}$$

is the pondermotive phase, with $(k_r + k_u)z - \omega_r t$ the phase of the electron with respect to the pondermotive wave and ϕ_r the phase of the radiation which is allowed to evolve.

Now,

$$\begin{aligned} \frac{\mathrm{d}\theta}{\mathrm{d}t} &= (k_r + k_u)c\beta_z - ck_r, \\ &= c(k_r + k_u)\left(1 - \frac{1+K^2}{2\gamma^2}\right) - ck_r, \\ &= ck_r\left(\frac{k_u}{k_r} - \frac{1+K^2}{2\gamma^2}\right). \end{aligned} \tag{2.24}$$

Setting this equal to zero, rearranging and using $k_u/k_r = \lambda/\lambda_u$ recovers the on-axis resonance condition found in Section 2.2. This is rewritten here for clarity as

$$\lambda = \frac{\lambda_u}{2\gamma_r^2}(1 + K^2), \tag{2.25}$$

where γ_r has been introduced as the resonant electron energy. Electrons with energy near the resonant energy will have a slow but sustained exchange of energy with the radiation field over many undulator periods. An electron's energy will deviate from the resonant energy while interacting with the field in the undulator. Therefore the parameter, η, describing an electron's energy deviation from the resonant energy normalised to the resonant energy is introduced. This electron energy variable is given by

$$\eta = \frac{\gamma - \gamma_r}{\gamma_r} \ll 1. \tag{2.26}$$

The exchange of energy of the electron and the radiation can now be expressed in

terms of the rate of change of η. γ_r is a fixed value so

$$\frac{\mathrm{d}\eta}{\mathrm{d}t} = \frac{1}{\gamma_r}\frac{\mathrm{d}\gamma}{\mathrm{d}t}. \tag{2.27}$$

Using equation (2.21), along with changing the dependent variable of the differential from t to z, gives

$$\frac{\mathrm{d}\eta}{\mathrm{d}z} = \epsilon \sin(\theta), \tag{2.28}$$

where

$$\epsilon = \frac{eKE_0}{mc^2\gamma_r^2}. \tag{2.29}$$

Substituting $\gamma = \gamma_r(\eta + 1)$ into equation (2.24) (and using approximation $1/(1-x)^2 \approx 1 + 2x$ for small x) it is straightforward to show

$$\begin{aligned} \frac{\mathrm{d}\theta}{\mathrm{d}z} &= k_u \left(1 - \frac{1}{(\eta+1)^2}\right), \\ &= 2k_u\eta. \end{aligned} \tag{2.30}$$

Equations (2.28) and (2.30) describe the evolution of the electron energy and phase along the undulator axis when interacting with a constant field and are the familiar pendulum equations.

The equivalent equations for a planar undulator are the same except

$$\epsilon = \frac{e\tilde{K}E_0}{2mc^2\gamma_r^2}, \tag{2.31}$$

for the planar undulator case. The equation now contains the modified undulator parameter $\tilde{K}$, defined as

$$\tilde{K} = K\left[J_0\left(\frac{K^2}{4+2K^2}\right) - J_1\left(\frac{K^2}{4+2K^2}\right)\right], \tag{2.32}$$

where $J_0(x)$ and $J_1(x)$ are Bessel functions. This modified undulator parameter arises from the oscillation in z which reduces the coupling between the electrons and the radiation. The parameter $\tilde{K}$ is used in equations that involve the interaction strength but not the resonant wavelength calculation which is independent of FEL interaction.

2.4.2 The Wave Equation

The pendulum equations do not offer a full picture of the FEL as they assume the field is constant. To have a complete description of the FEL, the field must be allowed to evolve. Maxwell's wave equation for the electric field from a moving charge is

$$\left(\frac{\partial^2}{\partial z^2} - \frac{1}{c^2}\frac{\partial^2}{\partial t^2} + \nabla_\perp^2\right)\boldsymbol{E} = \mu_0\frac{\partial \boldsymbol{J}_\perp}{\partial t} + \frac{1}{\epsilon}\nabla\rho_e, \tag{2.33}$$

where ∇ is the Laplacian and $\boldsymbol{J}$ is the current density. The underlying physics of the FEL interaction is adequately described without diffraction and space charge terms and these terms are dropped. The wave equation, now expressed in the 1D approximation, is

$$\left(\frac{\partial^2}{\partial z^2} - \frac{1}{c^2}\frac{\partial^2}{\partial t^2}\right)\boldsymbol{E} = \mu_0\frac{\partial \boldsymbol{J}_\perp}{\partial t}, \tag{2.34}$$

where the transverse current is

$$\boldsymbol{J}_\perp = -ec\sum_{j=1}^{N}\boldsymbol{\beta}_{\perp j}\delta(\boldsymbol{r} - \boldsymbol{r}_j(t)). \tag{2.35}$$

As the many electrons in the beam contribute to the current, the subscript j is introduced to indicate quantities belonging to the jth electron in the beam. The current then includes the sum over the number, N, of electrons in the electron beam with positions $\boldsymbol{r}_j(t)$. (A typical electron beam contains a very large number of electrons, $N \approx 10^9$) The delta function can be expressed as $\delta(\boldsymbol{r} - \boldsymbol{r}_j(t)) = \delta(x - x_j)\delta(y - y_j)\delta(z - z_j)$.

To follow previous derivations [33, 34] the electric field in equation (2.19) is now expressed in exponential form

$$\boldsymbol{E} = \frac{-i}{\sqrt{2}}\left(\tilde{E}(z,t)e^{i(k_r z - \omega_r t)}\hat{\boldsymbol{e}} - \tilde{E}^*(z,t)e^{-i(k_r z - \omega_r t)}\hat{\boldsymbol{e}}^*\right). \tag{2.36}$$

The field is decomposed into two parts: a slowly varying field envelope describing the amplitude and phase, $\tilde{E}(z,t) = E_0 e^{i\phi_r}$ and a fast oscillatory term $e^{i(k_r z - \omega_r t)}$. The unit vector is defined as, $\hat{\boldsymbol{e}} = \frac{\hat{\boldsymbol{x}} + i\hat{\boldsymbol{y}}}{\sqrt{2}}$ and then $\hat{\boldsymbol{e}}\cdot\hat{\boldsymbol{e}} = 0$ and $\hat{\boldsymbol{e}}\cdot\hat{\boldsymbol{e}}^* = 1$. Equation (2.36) can be substituted into equation (2.34). Integrating over the transverse plane and taking the

scalar product with $\hat{\boldsymbol{e}}^*$ gives [35]

$$\frac{-i}{\sqrt{2}}\left(\frac{\partial^2}{\partial z^2}-\frac{1}{c^2}\frac{\partial^2}{\partial t^2}\right)\tilde{E}(z,t)e^{i(k_r z-\omega_r t)}=\frac{\mu_0}{\sigma}\frac{\partial J_{\hat{e}}}{\partial t}, \tag{2.37}$$

where σ is the cross sectional area which is assumed to be equal for the radiation and electron beam. The delta functions, $\delta(x-x_j)$ and $\delta(y-y_j)$, integrate to unity and the current term is

$$J_{\hat{e}}=-ec\sum_{j=1}^{N}\beta_{\hat{e}j}\delta(\boldsymbol{z}-z_j(t)). \tag{2.38}$$

Equation (2.5) gives the electron's velocity in a helical undulator without the radiation field contribution. Using $\beta_{\hat{e}j}=\boldsymbol{\beta}_{\perp}j\cdot\hat{\boldsymbol{e}}^*$, the electron velocity in exponential form is inserted into equation 2.38 to give

$$J_{\hat{e}}=\frac{ecK}{\sqrt{2}}\sum_{j=1}^{N}\frac{1}{\gamma_j}e^{-ik_u z}\delta(z-z_j(t)). \tag{2.39}$$

2.4.3 The Slowly Varying Envelope Approximation

Typical analysis of the FEL equations apply the slowly varying envelope approximation (SVEA). This approximation states that the radiation envelope varies slowly with respect to the radiation wavelength in both space and time. This allows the statements

$$\left|\frac{\partial\tilde{E}}{\partial z}\right|\ll\left|k\tilde{E}\right|,\quad\left|\frac{\partial\tilde{E}}{\partial t}\right|\ll\left|\omega\tilde{E}\right|. \tag{2.40}$$

This approximation allows the second derivatives in the wave equation to be dropped.

Applying this approximation to the LHS of equation (2.37) gives

$$\frac{-i}{\sqrt{2}}\left(\frac{\partial^2}{\partial z^2}-\frac{1}{c^2}\frac{\partial^2}{\partial t^2}\right)\tilde{E}(z,t)e^{i(k_r z-\omega_r t)}\simeq\sqrt{2}k_r\left[\left(\frac{\partial}{\partial z}+\frac{1}{c}\frac{\partial}{\partial t}\right)\tilde{E}\right]e^{i(k_r z-\omega_r t)}. \tag{2.41}$$

Using this result, equation (2.37) becomes

$$\left(\frac{\partial}{\partial z}+\frac{1}{c}\frac{\partial}{\partial t}\right)\tilde{E}=\frac{\mu_0}{\sqrt{2}k_r\sigma}\frac{\partial J_{\hat{e}}}{\partial t}e^{-i(k_r z-\omega_r t)}. \tag{2.42}$$

The SVEA restricts any frequency dependent change in the evolution of the field amplitude to frequencies around the resonance frequency, $2\pi/\lambda_r$. To establish a slowly varying current, equation (2.42) is averaged over the time interval $\Delta t = n\lambda_r/c$: for n an integer. It is assumed that the amplitude of the envelope is approximately constant over the integration window and the LHS is unchanged by the integration. Taking the RHS side and applying the product rule gives [36]

$$\frac{\mu_0}{\sqrt{2}k_r\sigma\Delta t}\int_{t-\Delta t/2}^{t+\Delta t/2}\frac{\partial J_{\hat{e}}}{\partial t}e^{-i(k_r z-\omega_r t)}\mathrm{d}t \approx \frac{-\mu_0}{\sqrt{2}k_r\sigma\Delta t}\int_{t-\Delta t/2}^{t+\Delta t/2} i\omega J_{\hat{e}}e^{-i(k_r z-\omega_r t)}\mathrm{d}t. \quad (2.43)$$

$J_{\hat{e}}$ is substituted into this equation and the variable in the delta function is changed using $\delta(z - z_j(t)) = \delta(t - t_j(z))/c\beta_z$. The delta function has the property

$$\int_{a-\epsilon}^{a+\epsilon} f(x)\delta(x-a)dx = f(a). \quad (2.44)$$

The integration thus picks out the N electrons passing a fixed plane of z in the time interval Δt. The slowly varying equation is now

$$\left(\frac{\partial}{\partial z}+\frac{1}{c}\frac{\partial}{\partial t}\right)\tilde{E} = \frac{-ieKn_e}{2\epsilon_0\gamma_r}\left(\frac{1}{N}\sum_{j=1}^{N}e^{-i\theta_j}\right), \quad (2.45)$$

where $\theta_j = (k_r + k_u)z - \omega t_j(z)$ and n_e is the number density. It was assumed that the electrons all have similar energy and thus γ_j is taken out of the sum and relabelled γ_r. The term in the brackets is the bunching parameter, b,

$$b = \frac{1}{N}\sum_{j=1}^{N}e^{-i\theta_j}. \quad (2.46)$$

The bunching parameter gives a measure of the micro-bunching in the electron beam. If the electrons are uniformly distributed in phase, $|b| = 0$ and there is no net gain to the field. If $|b| > 0$, there is a net gain to the field. An electron beam where all the electrons in a slice have the same phase has a bunching parameter $|b| = 1$, this is the maximum bunching possible and describes a fully bunched electron beam. Note that for the planar undulator case, the average values of the electrons' velocity and

phase must be used due to the oscillation along z. As with the pendulum equations, the modified undulator parameter, defined in equation (2.32), is used when describing a planar undulator.

Equations (2.28), (2.30) and (2.45) make up the FEL equations. These are a set of coupled differential equations describing the evolution of the electron phase and radiation field. Before solving these equations, it is helpful to scale them via the universal scaling developed by Bonifacio *et al.* [37].

2.5 Universal Scaling

Universal scaling is commonly applied to the FEL equations to produce a simpler description of the FEL mechanism without consideration of specific operating parameters. In later chapters, examples of experimentally relevant parameters are provided (see Table 5.1 and Table 6.1.) To scale the equations, dimensionless variables are defined which are normalised to the FEL or Pierce parameter, ρ, defined as

$$\rho = \frac{1}{\gamma}\left(\frac{a_u \omega_p}{4ck_u}\right)^{2/3}, \tag{2.47}$$

where the plasma frequency, ω_p is

$$\omega_p = \sqrt{\frac{e^2 n_p}{\epsilon_0 m}} \tag{2.48}$$

and n_p is the peak electron number density of the electron bunch.

Scaled co-ordinates

The scaled coordinates $\bar{z}$ and $\bar{z}_1$ replace z and t on the FEL equations. The distance through the undulator is scaled using

$$\bar{z} = \frac{4\pi\rho}{\lambda_u} z. \tag{2.49}$$

$\bar{z}_1$, is the scaled coordinate in the frame moving the velocity of the pondermotive wave. $\bar{z}_1$ replaces the time coordinate and is defined as

$$\bar{z}_1 = \frac{4\pi\rho}{\lambda_r}(z - c\bar{\beta}_z t). \tag{2.50}$$

The derivatives in the FEL equations can then be transformed using

$$\frac{\mathrm{d}}{\mathrm{d}z} = \frac{4\pi\rho}{\lambda_u}\frac{\mathrm{d}}{\mathrm{d}\bar{z}} \quad \text{and} \quad \left(\frac{\partial}{\partial z} + \frac{1}{c}\frac{\partial}{\partial t}\right) = \frac{4\pi\rho}{\lambda_u}\left(\frac{\partial}{\partial \bar{z}} + \frac{\partial}{\partial \bar{z}_1}\right). \tag{2.51}$$

Scaled FEL equations

The FEL equations are now rewritten replacing η with the scaled energy parameter $p_j = \frac{\gamma_j - \gamma_r}{\rho\gamma_r}$ and replacing the $\tilde{E}$ with the scaled complex field envelope $A = \frac{a_u e\tilde{E}}{4mc^2 k_u \rho^2 \gamma^2}$. The universally scaled FEL equation are then given by

$$\frac{\mathrm{d}p_j}{\mathrm{d}\bar{z}} = -i\left(Ae^{i\theta_j} - A^* e^{-i\theta_j}\right), \tag{2.52}$$

$$\frac{\mathrm{d}\theta_j}{\mathrm{d}\bar{z}} = p_j, \tag{2.53}$$

$$\left(\frac{\partial}{\partial \bar{z}} + \frac{\partial}{\partial \bar{z}_1}\right) A = -ib. \tag{2.54}$$

2.6 Steady-state Analysis

The equations can be further simplified by assuming that the electron beam is continuous, with no beginning or end, and that the properties of the electron beam are uniform across the beam. This is called the 'steady state' approximation. In this approximation, the radiation field will only have a spatial dependence and no time dependence which allows the derivative with respect to $\bar{z}_1$ to be dropped in equation (2.54). This assumption is used in the following section to examine the FEL instability which leads to amplification of the radiation field, however, it does not take into account the slippage between the radiation field. The effect of slippage is examined further in Section 2.7. . In the steady-state regime, the FEL equations are easily solved numerically. The

scaled intensity and bunching parameter are plotted in Figure 2.6 for a uniformly distributed electron beam and small initial field. The FEL process can be considered in three stages. In the first stage, $\bar{z} \lesssim 2$, there is little growth of the radiation field, this is referred to as the lethargy region. After this region, the field experiences exponential growth up until the last region, where saturation effects occur. In first two regions - lethargy followed by exponential growth - the output power scales linearly with input power and these regions are well described by linear theory [37]. Exponential growth cannot continue indefinitely and nonlinear saturation effects act in the final region to limit growth.

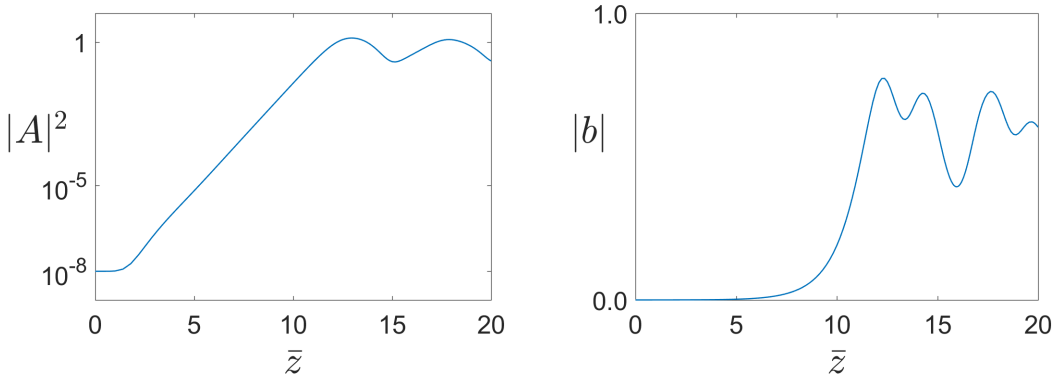

Figure 2.6: Numerical evaluation of the steady-state FEL equations with an initial radiation field $|A_0| = 10^{-4}$. Left: The scaled intensity vs $\bar{z}$. Right: The bunching parameter vs $\bar{z}$.

McNeil and Thompson [38] give a clear description of the FEL mechanism, which shows how the electron bunching can drive the FEL interaction. To follow this description, the FEL equations are stated with the radiation field separated into a magnitude and phase term $A = |A|e^{i\phi_r}$. In order for the FEL equations presented here to match the equations in [38], a phase offset is introduced so that $\phi_r \to (\phi_r - \pi/2)$. The steady state wave equation is now given by

$$\frac{\mathrm{d}A}{\mathrm{d}\bar{z}} + |A|i\frac{\mathrm{d}\phi_r}{\mathrm{d}\bar{z}} = \langle e^{-i(\theta_j+\phi_r)}\rangle, \tag{2.55}$$

where $\langle ... \rangle = \frac{1}{N}\sum_{j=1}^{N}$. Equating the real and imaginary parts gives the evolution of

the fields amplitude and phase as

$$\frac{\mathrm{d}A}{\mathrm{d}\bar{z}} = \langle \cos(\theta_j + \phi_r) \rangle, \tag{2.56}$$

$$\frac{\mathrm{d}\phi_r}{\mathrm{d}\bar{z}} = -\frac{1}{|A|} \langle \sin(\theta_j + \phi_r) \rangle. \tag{2.57}$$

With the phase offset, the rate of change of energy becomes

$$\frac{\mathrm{d}p_j}{\mathrm{d}\bar{z}} = -2|A| \cos(\theta_j + \phi_r). \tag{2.58}$$

For an electron beam with uniformly distributed electrons, $\frac{\mathrm{d}A}{\mathrm{d}\bar{z}} = 0$, $\frac{\mathrm{d}\phi}{\mathrm{d}\bar{z}} = 0$ and the field is not driven. However, the introduction of a small radiation field will change the energy of the electrons. From equation (2.58), electrons with a phase $\pi/2 < \theta < \frac{3\pi}{2}$ will gain energy and electrons with a phase $0 < \theta < \pi/2$ or $3\pi/2 < \theta < 2\pi$ will lose energy. The energy modulation of electrons transfers to a density modulation and the electrons start to bunch about $\theta = 3\pi/2$. The radiation is not immediately amplified as $\frac{\mathrm{d}A}{\mathrm{d}\bar{z}} = 0$. However, inspection of equation (2.57) shows that this bunching will drive the radiation phase and, since the initial field is very small, this phase change is significant. Now $\phi_r > 0$, then the amplitude of the radiation field increases, which in turn increases the bunching in the field. The electron bunching continues to drive the radiation phase and subsequently the field amplitude until saturation. At saturation $|A| \sim 1$, and the rate of phase change is slowed down and the electrons will regain some of the energy from the field.

From the scaling of A it can be shown that [37]

$$\rho |A|^2 = \frac{P_{rad}}{P_{beam}}, \tag{2.59}$$

where P_{rad} and P_{beam} are the power in the radiation field and the electron beam, respectively. The FEL power saturates when $|A|^2 \approx 1$ and so the above relation shows that ρ gives the efficiency of the FEL, *i.e.* the fraction of electron beam power converted to radiation power.

To explore the exponential gain of the radiation further, the FEL equations can

be linearised by considering the evolution of the equations with small perturbations applied to their initial conditions. This is not included in this thesis; however, we do note an important result that FEL amplification is characterised by the gain length, l_g, which is given by

$$l_g = \frac{\lambda_u}{4\pi\rho}. \tag{2.60}$$

Revisiting the universal scaling, equation (2.49), it is seen that the distance through the undulator was scaled to the gain length.

2.7 SASE

The above analysis considered FEL amplification in the steady-state regime where the initial seed for amplification came from an initial radiation field. A more complete picture includes slippage of the light relative to the electrons as well as variation of the electron density along the bunch. The bunch variation, which arises from shot noise from the electron gun, means that the initial bunching parameter along the beam is non-zero and therefore can act as the initial seed to start up the FEL process. This is particularly important at short wavelengths where radiation seeds are not available. Starting the FEL process with the random density fluctuations in the electron beam is called Self Amplified Spontaneous Emission (SASE).

The temporal structure of SASE radiation is initially spiky with very little temporal coherence, however, the slippage in the electron beam acts to increase the temporal coherence in the beam. A measure of the influence that the slippage has on the temporal coherence is defined by the cooperation length [39],

$$l_c = \frac{\lambda_r}{2\pi\rho}. \tag{2.61}$$

This is the length the radiation field slips ahead of the electrons in one gain length. Figure 2.7 shows an example of SASE output at saturation. An electron beam that is much longer than l_c will have a spiky radiation profile at saturation with a maximum peak separation $\approx 2\pi l_c$.

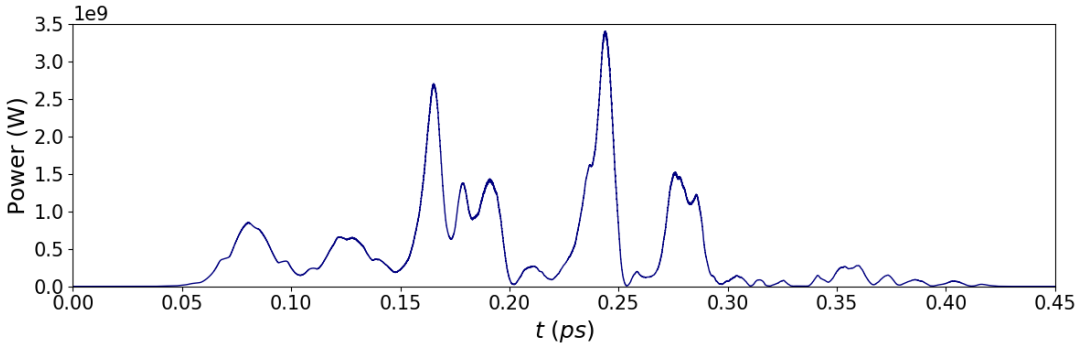

Figure 2.7: Typical SASE radiation profile of a FEL.

Chapter 3

Orbital Angular Momentum of Light

The starting point for the work in this thesis was to consider FEL radiation carrying orbital angular momentum. This chapter develops a theoretical basis for the orbital angular momentum, OAM, of light. In Chapter 4, generation of light carrying OAM using a FEL is discussed.

3.1 Orbital Angular Momentum

Since the 1600s, it has been understood that light carries angular momentum. In 1909, Poynting [40] explained that as well as linear momentum, circularly polarised light also carries spin angular momentum. Before a seminal paper from Allen *et al.* in 1992 [41], OAM was thought to be a property of light confined to only being concerned with higher-order atomic transitions. Allen *et al.* corrected this notion, showing that light beams with helical wavefronts also carry OAM. These helically phased beams could readily be generated with standard optics and, in fact, had already been generated and studied for many of the previous years without recognition of the OAM. Instead, it was the beams' intensity profile, which is null on-axis, that was of interest to researchers. Allen *et al.'s* paper was a breakthrough not only for recognising that light carries OAM but also that it is quantized, with each photon carrying a discrete value of

OAM. Since 1992, OAM has received considerable attention, with applications such as optical tweezers [42], and in the fields of quantum optics [43], imaging [44] and optical communication [45], to list a few examples. A more in-depth look at the diverse range of application areas involving light's OAM is provided in Ref. [46].

3.1.1 Helically-phased beams

The amplitude distribution of helically-phased beams can be expressed in cylindrical coordinates as [47],

$$\boldsymbol{u}(r, \phi, z) = \boldsymbol{u}_0(r, z) \exp(i\ell\phi) \tag{3.1}$$

where ℓ, an integer, is the azimuthal mode number and ϕ is the angular coordinate. Compared to the usual plane waves, where $\ell = 0$, the phase of radiation has now acquired a new component, so the total phase of the wave is $kz - \omega t + \ell\phi$. The result of this new phase term is that the phase front of the radiation is twisted into a helix. Figure 3.1 shows the surface of constant phase for different values of ℓ. The magnitude and sign of ℓ determine, respectively, the number of intertwined helixes and the handedness of the helixes. Unlike spin momentum, which is limited between the values ± 1, the magnitude of ℓ is theoretically unbounded. This is of particular interest as it suggests the potential for light to carry more information per photon.

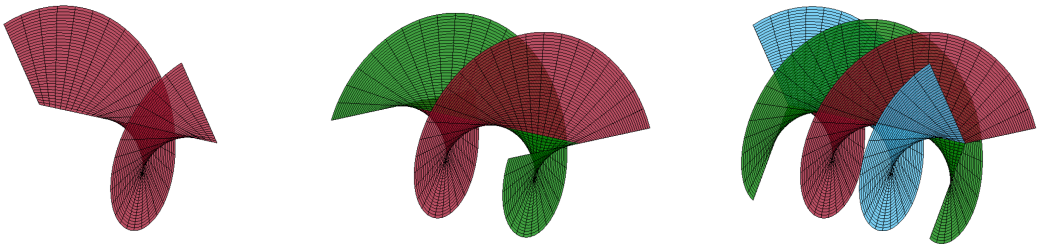

Figure 3.1: Wavefronts for waves with azimuthal index (left to right) $\ell = 1, 2, 3$.

Instead of considering the phase fronts of these beams, the phase of a cross section of an $\ell = 1$ beam is shown in Figure 3.2. It is seen that travelling around the azimuth of the beam changes the phase of the light. ℓ thus defines the number of times the phase changes from 0 to 2π in one rotation. This means that a change in ϕ is indistinguishable from time - travelling around the azimuth of the beam is equivalent to a change in time. Another consequence of this phase structure is that at the centre of the beam there is a phase singularity and, associated with this singularity, the intensity of the light is zero. This produces a ring intensity profile, with no intensity at the centre and the radius of the maximum intensity increasing with $|\ell|$ as $\sqrt{\ell/2}w$, where w is the beam waist when $\ell = 0$.

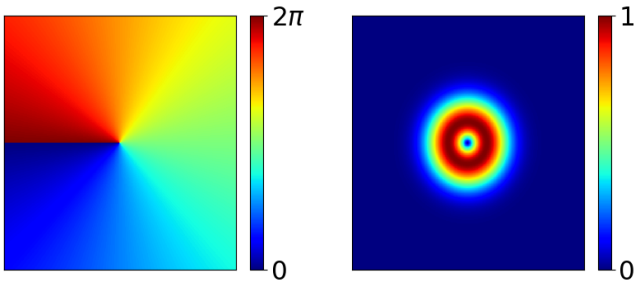

Figure 3.2: Phase (left) and normalised intensity (right) cross section of a helically phased $\ell = 1$ beam.

Angular momentum

It is understood that light carries momentum which can interact with physical systems. The twisted wavefronts described above means some of the momentum carried by the radiation is OAM. To see how this specific angular momentum arises, consider the direction of the flow of energy of a light beam. The flow of energy of an electromagnetic beam is described by the Poynting Vector, $\boldsymbol{S}$,

$$\boldsymbol{S} = \frac{1}{\mu_0}\boldsymbol{E} \times \boldsymbol{B} \tag{3.2}$$

where μ_0 is the permeability of free space. In free space, the Poynting vector also describes the flow of momentum. This vector points in the direction which is the

surface normal of the wavefront. For plane waves, $\ell = 0$, this vector is directed solely along z, the direction of propagation. When the phase front twists - as in Figure 3.1 - then the Poynting vector is no longer parallel to the optical axis and acquires an azimuthal component. The light then carries an angular momentum in the direction of propagation, which appears as a consequence of the phase gradient and is unrelated to the spin momentum which results from the rotating polarisation vector in circularly polarised light.

Perhaps it is easiest to understand the difference between the momentum types by considering the effect it has when transferred to a trapped particle [42, 48]. Linear momentum parallel to the optical axis when transferred to a particle will push it away in the direction of the radiation propagation. Spin momentum causes a rotation around the centre of the particle, whereas the orbital angular momentum will rotate the particle at a radius, r, round the centre of the beam.

A simple picture of the azimuthal component of momentum flow has been provided. A more in-depth look at how this property arises and how, less intuitively perhaps, helically phased beams carry discrete values of OAM equivalent to $\ell\hbar$ per photon is now needed.

3.1.2 Spin and OAM Separation in the Paraxial Approximation

OAM was first studied in the paraxial approximation. The following sections will also utilise this approximation as, in the paraxial regime, spin momentum and orbital angular momentum are easily separated. Paraxial waves provide a close description of real laser amplification [49] and propagation including FEL radiation. The paraxial approximation assumes that changes in transverse beam profile change particularly slowly in z such that the terms $\partial^2\boldsymbol{u}/\partial z^2$ and $|\partial\boldsymbol{u}/\partial z|$ can be ignored in the derivation of the wave equation. The paraxial wave equation is then

$$2i\frac{\partial \boldsymbol{u}(r,\phi,z)}{\partial z} = -\frac{1}{k}\left(\frac{\partial^2}{\partial x^2} + \frac{\partial^2}{\partial y^2}\right)\boldsymbol{u}(r,\phi,z). \tag{3.3}$$

First, the vector potential of a laser mode is defined as

$$\boldsymbol{A} = \boldsymbol{u}(r, \phi, z) \exp(ikz)\hat{\boldsymbol{e}}_{\perp}, \tag{3.4}$$

where $\hat{\boldsymbol{e}}_{\perp}$ is the transverse polarisation vector. $\boldsymbol{u}(r, \phi, z)$, is the amplitude distribution which is given by equation (3.1). The electric and magnetic fields expressed in terms of the vector potential via the Lorenz gauge are [50]

$$\boldsymbol{E} = i\omega \left(\boldsymbol{A} + \frac{1}{k^2} \nabla(\nabla \cdot \boldsymbol{A}) \right), \tag{3.5}$$

$$\boldsymbol{B} = \nabla \times \boldsymbol{A}. \tag{3.6}$$

The real part of the time averaged linear momentum density is [51]

$$\begin{aligned} \boldsymbol{p} &= \epsilon_0 \langle \boldsymbol{E} \times \boldsymbol{B} \rangle, \\ &= \frac{\epsilon_0}{2} [(\boldsymbol{E}^* \times \boldsymbol{B}) + (\boldsymbol{E} \times \boldsymbol{B}^*)], \\ &= \frac{\omega \epsilon_0}{2} \Big[i \Big(\boldsymbol{u}(r, \phi, z) \nabla \boldsymbol{u}^*(r, \phi, z) - \boldsymbol{u}^*(r, \phi, z) \nabla \boldsymbol{u}(r, \phi, z) \Big) + \sigma \frac{\partial |\boldsymbol{u}_0(r, z)|^2}{\partial r} \hat{\boldsymbol{e}}_{\boldsymbol{\phi}} \\ &\qquad + 2k |\boldsymbol{u}_0(r, z)|^2 \hat{\boldsymbol{e}}_{\boldsymbol{z}} \Big], \end{aligned} \tag{3.7}$$

where $\sigma = \pm 1$ gives the polarisation of the radiation and ϵ_0 is the permittivity of free space. Using, $\nabla = (\frac{\partial}{\partial r}\hat{\boldsymbol{e}}_{\boldsymbol{r}} + \frac{1}{r}\frac{\partial}{\partial \phi}\hat{\boldsymbol{e}}_{\boldsymbol{\phi}} + \frac{\partial}{\partial z}\hat{\boldsymbol{e}}_{\boldsymbol{z}})$, to evaluate the first two terms revels an OAM term in the azimuthal component of linear momentum

$$\begin{aligned} \boldsymbol{p} = \frac{\omega \epsilon_0}{2} \Big[i \Big(\boldsymbol{u}_0(r, z) \nabla \boldsymbol{u}_0^*(r, z) - \boldsymbol{u}_0(r, z)^* \nabla \boldsymbol{u}_0(r, z) \Big) + \Big(\frac{2\ell}{r} |\boldsymbol{u}_0(r, z)|^2 + \sigma \frac{\partial |\boldsymbol{u}_0(r, z)|^2}{\partial r} \Big) \hat{\boldsymbol{e}}_{\boldsymbol{\phi}} \\ + 2k |\boldsymbol{u}_0(r, z)|^2 \hat{\boldsymbol{e}}_z \Big]. \end{aligned} \tag{3.8}$$

The ϕ component of the linear momentum now has two terms, the first relates to the orbital angular momentum and depends on the azimuthal mode number ℓ. The second term relates to the spin momentum and depends on the polarisation σ. This

is consequential as the cross product of linear momentum with $\hat{\boldsymbol{r}}$ gives the angular momentum density

$$\boldsymbol{j} = \hat{\boldsymbol{r}} \times \boldsymbol{p} \tag{3.9}$$

and therefore the angular momentum in the direction of propagation is

$$j_z = r p_\phi = \frac{\epsilon_0 \omega}{2}\Big(2\ell |\boldsymbol{u}_0(z,r)|^2 + r\sigma \frac{\partial |\boldsymbol{u}_0(r,z)|^2}{\partial r}\Big). \tag{3.10}$$

In the paraxial approximation, most of the energy of the field is concentrated in the longitudinal direction, the time averaged energy density can therefore be defined as

$$\mathrm{w} \simeq c p_z = c\omega k \epsilon_0 |\boldsymbol{u}_0(r,z)|^2 \tag{3.11}$$

and then the local ratio of angular momentum to total energy is

$$\frac{j_z}{\mathrm{w}} = \frac{\ell}{\omega} + \frac{\sigma r}{2\omega |\boldsymbol{u}_0(r,z)|^2} \frac{\partial |\boldsymbol{u}_0(r,z)|^2}{\partial r}. \tag{3.12}$$

The total angular momentum, J_z, and total energy, W, ratio can be found by integrating across the beam to give

$$\frac{J_z}{W} = \frac{\int\int r j_z \mathrm{d}r\mathrm{d}\phi}{\int\int r \mathrm{w} \mathrm{d}r\mathrm{d}\phi} = \frac{\ell + \sigma}{\omega}. \tag{3.13}$$

Equations (3.12) and (3.13) demonstrate that orbital and spin momentum are separated - at least in the paraxial regime. Right-handed and left-handed polarisation are indicated when, respectively, $\sigma = -1$ and $\sigma = +1$. For $\sigma = 0$ the light is linear polarised; it is seen that the OAM is independent of the polarisation and linear polarised light can carry OAM. Similarly, light without OAM, $\ell = 0$, can still carry angular momentum through the polarisation.

Another important result is found through multiplying equation (3.13) by the energy of one photon, $\hbar\omega$. This shows that the OAM along z carried per photon is $\hbar\ell$. It also follows that the spin momentum is $\pm\hbar$ as expected.

Non-paraxial beams

A similar result for non-paraxial beams can be derived directly from Maxwell's equations [50, 52]. However, out of the paraxial regime, there is an additional correction term in the energy ratio equation. This demonstrates that there is not such a simple separation between the spin and orbital angular momentum. However, it does show that the appearance of the orbital angular momentum is not an artefact of the paraxial approximation. The correction term has a dependence on σ only, when $\sigma = 0$ the correction term disappears and the ratio of J_z and W is exactly equation (3.13). This confirms that out of the paraxial regime, a light beam can carry orbital and not spin momentum.

3.2 Solutions to the Paraxial Wave Equation

The Laguerre-Gaussian and Hermite-Gaussian modes are solutions to the paraxial wave equation when solved with cylindrical or Cartesian coordinates, respectively. Both families of modes will be referenced throughout this thesis and so they are presented in the following section.

3.2.1 Laguerre-Gaussian Modes

The Laguerre-Gaussian, LG, modes were the first radiation beams discussed in the context of OAM. Although OAM is a property carried by all radiation beams with a helical phase structure, the LG modes are ubiquitous in the literature as they are a complete set of orthogonal modes. These modes have an amplitude defined as [47]

$$\begin{aligned} LG_{p,\ell} = \sqrt{\frac{2p!}{\pi(p+|\ell|)!}} \frac{1}{w(z)} \left[\frac{r\sqrt{2}}{w(z)}\right]^{|\ell|} \exp\left[\frac{-r^2}{w^2(z)}\right] L_p^{|\ell|}\left(\frac{2r^2}{w^2(z)}\right) \exp[i\ell\phi] \\ \exp\left[\frac{ik_0 r^2 z}{2(z^2+z_R^2)}\right] \exp\left[-i(2p+|\ell|+1)\tan^{-1}\left(\frac{z}{z_R}\right)\right], \end{aligned} \tag{3.14}$$

where the beam waist w_0 evolved as $w(z) = w_0(1 + z^2/z_R^2)^{1/2}$ along z. The variable z_R is the Rayleigh range and the functions $L_p^{|\ell|}$ are associated Laguerre polynomials. The

mode numbers p and ℓ give, respectively, the radial mode and the azimuthal mode. Figures 3.3 and 3.4 give the intensity and phase profiles for the first three p and ℓ mode numbers. The lowest order mode of this set is found with $p = \ell = 0$ which is the simple Gaussian distribution. For $|\ell| > 1$, LG modes have a well defined angular momentum as they have an azimuthal dependence $e^{i\ell\phi}$.

The LG modes also make up a complete basis set which means that any arbitrary radiation field can be expressed as a complete sum of the different LG modes. As the modes are mutually orthogonal then

$$\int\int LG_{p,\ell} LG^{*}_{p',\ell'} \mathrm{d}x\mathrm{d}y = \delta_{p,p'}\delta_{\ell,\ell'}. \tag{3.15}$$

This will be used later in this thesis to decompose the radiation from FEL simulations into the different LG modes in order to examine the OAM content.

3.2.2 Hermite Gaussian Modes

Another complete set of orthogonal modes are the Hermite-Gaussian, HG, modes. These modes have amplitude distributions defined by

$$\begin{aligned} HG_{m,n} = \sqrt{\frac{2^{1-(n+m)}}{\pi n!m!}} \frac{1}{w(z)} \exp\Big[\frac{-(x^2+y^2)}{w^2(z)}\Big] H_m\Big(\frac{x\sqrt{2}}{w(z)}\Big) H_n\Big(\frac{y\sqrt{2}}{w(z)}\Big) \\ \exp\Big[\frac{-ik_0(x^2+y^2)z}{2(z^2+z_R^2)}\Big] \exp\Big[-i(m+n+1)\tan^{-1}\Big(\frac{z}{z_R}\Big)\Big]. \end{aligned} \tag{3.16}$$

Figure 3.5 displays the intensity profile for the first three n and m numbers. The intensity profiles have different intensity nodes which are π out of phase with each other. The mode numbers m and n are positive integers, they indicate the number of nodal lines in, respectively, the x and y directions. As with the LG modes, the lowest order mode, $n = m = 0$ is the Gaussian mode.

A single HG mode does not contain OAM. However, there is transverse variation in the phase profile of the higher-order HG modes. Any radiation beam can be considered to be a superposition of the HG modes; therefore any LG modes can be expressed in terms of the HG modes. For example, the $LG_{0,1}$ mode is equivalent to the coherent

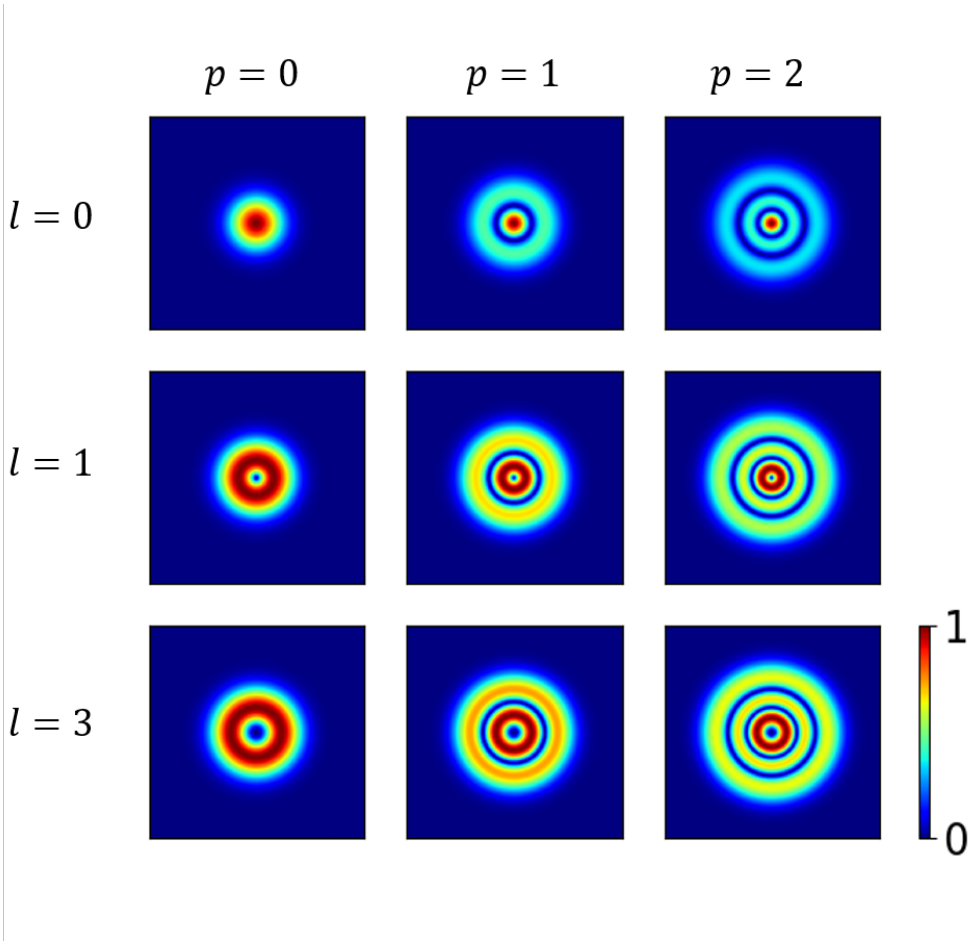

Figure 3.3: Normalised intensity distributions for the Laguerre-Gaussian modes when $z = 0$.

combination $HG_{0,1}$ and $HG_{1,0}$ modes with a $\pi/2$ phase shift *i.e.*

$$\frac{1}{\sqrt{2}} HG_{0,1} + \frac{i}{\sqrt{2}} HG_{1,0} = LG_{0,1}. \tag{3.17}$$

This superposition is shown in Figure 3.6.

3.2.3 Gouy Phase Shift

The Gouy phase shift, $\psi_{\mathrm{G}}(z)$, is associated with any wave passing through a focus or coming from a small source point. For the transverse modes described above, this phase

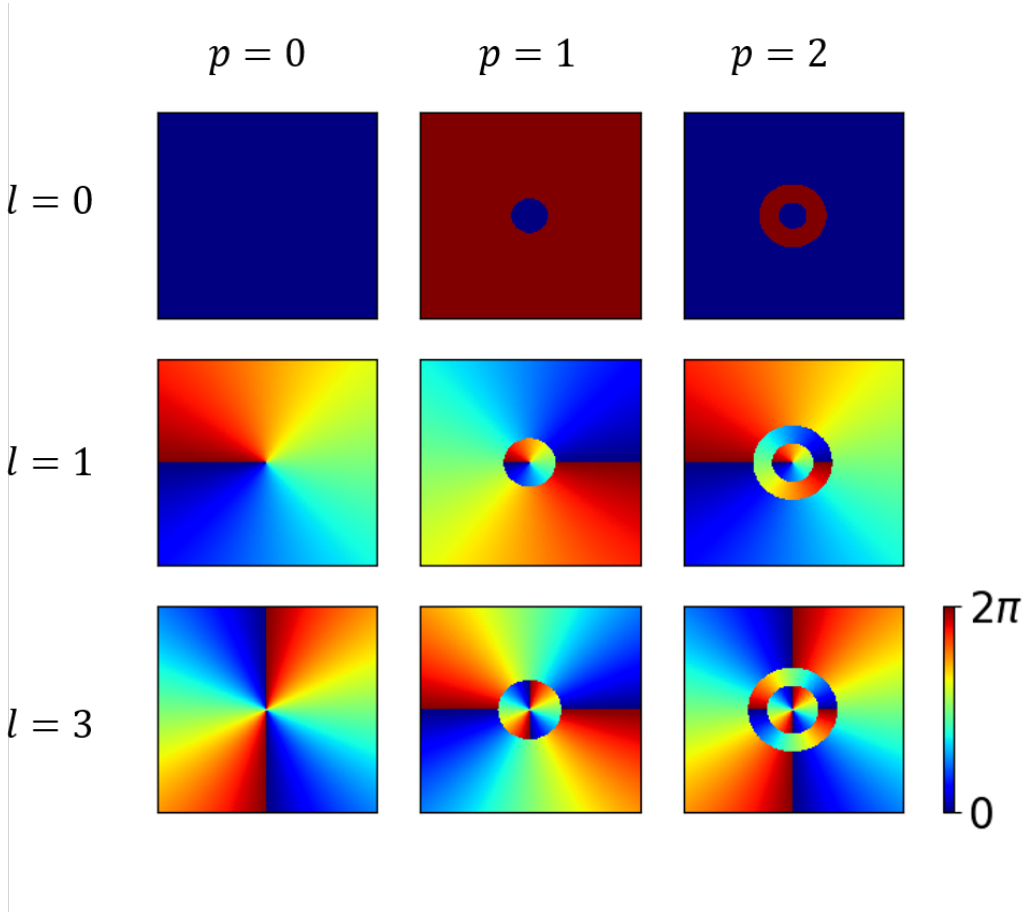

Figure 3.4: Phase distributions for the Laguerre-Gaussian modes when $z = 0$.

shift depends on the mode indexes. The Gouy phase shift for an LG mode is given by

$$\psi_{\mathrm{G},p,\ell}(z) = (2p + |\ell| + 1)\tan^{-1}\left(\frac{z}{z_R}\right) \tag{3.18}$$

and for a HG mode, it is

$$\psi_{\mathrm{G},n,m}(z) = (m + n + 1)\tan^{-1}\left(\frac{z}{z_R}\right). \tag{3.19}$$

This phase shift can be quite substantial, for example, a Gaussian beam passing though a focus will acquire a π phase shift. The Gouy effect can be seen in conventional laser cavities where the higher-order modes have different resonant frequencies [49].

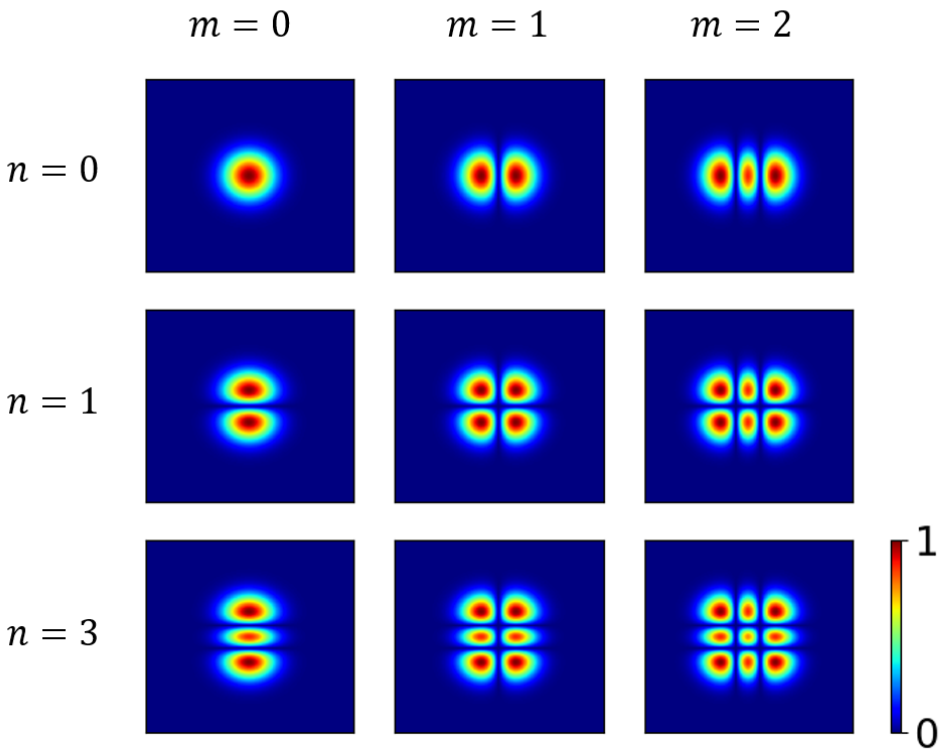

Figure 3.5: Normalised intensity distributions for the Hermite-Gaussian modes when $z = 0$.

3.3 Generation of OAM light

Conventional methods which produce light carrying OAM use different optical elements which impose the helical phase structure on a plane wave. An intuitive method to do this is with a spiral phase plate [53–55]. This optical element has an optical thickness that varies with azimuthal position. The light is delayed according to azimuthal position, which twists the phase distribution. Although a simple concept, execution is difficult, as extreme precision is required to make the element and spiral phase plates are not used for light at wavelengths shorter than visible wavelengths.

The method used by Allen *et al.* in the seminal OAM paper [41] was based on the mode conversion of *HG* to *LG* modes through a cylindrical lens telescope. As discussed

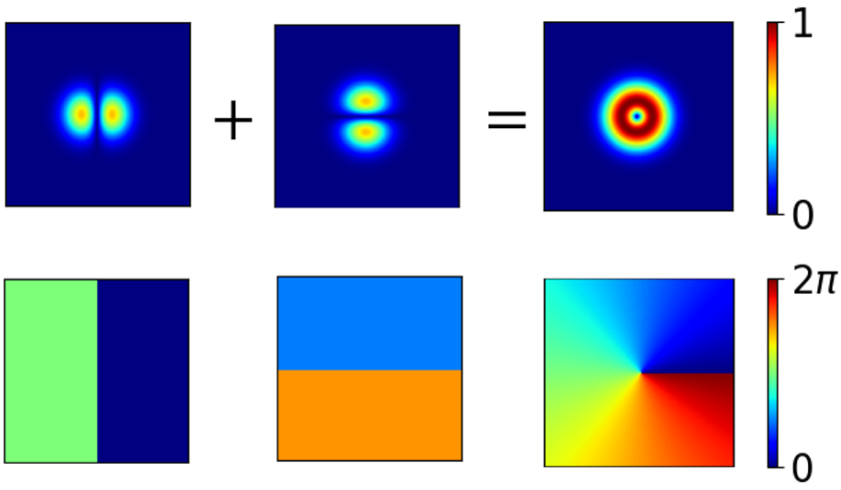

Figure 3.6: Schematic showing that the combination of Hermite-Gaissian modes $HG_{0,1}$ and $HG_{1,0}$ modes produce a Laguerre-Gaussian mode $LG_{0,1}$. Top: Intensity plots. Bottom: corresponding phase profiles.

in the previous section, the LG modes can be transformed into HG modes and vice versa. The method works due to the fact an HG mode at 45° can be decomposed into a set of HG modes. The cylindrical lenses then re-phase the HG modes - via the Gouy phase shift - to form an LG mode [47].

The cylindrical lens and spiral phase plate methods are both examples of refractive optics. However, before Allen *et al.'s* paper and without recognition of angular momentum of the light, an alternative technique was developed [56]. In this method, which uses computer generated holography, refractive optics such as the spiral phase plate are mimicked by diffracted optical elements. Combining the desired helical phase distribution with the phase of a diffraction grating (to separate out the zeroth order) results in a forked diffraction grating. Diffracting a Gaussian light beam through this hologram then converts the light into the desired helical beam, where the number of prongs on the 'fork' determines $|\ell|$. Further development of this method produced the spatial light modulators (SLMs), which are pixellated liquid crystal devices that will display an image generated by a computer. This allows the design displayed on the device to be easily changed, providing active programming of the phase of the light.

Chapter 4

Free Electron Laser Radiation Carrying Orbital Angular Momentum

The conventional techniques used to generate light carrying orbital angular momentum, discussed in Section 3.3, use optical elements that alter the phase of a Gaussian beam. These techniques have been developed to use with conventional lasers available in laboratories and, as a result, work best at the wavelengths and intensities offered by these lasers. FELs are used when the desired radiation has a shorter wavelength and/or higher intensity than that available with traditional sources and the traditional routes to convert the phase of radiation do not work. In particular, the damage threshold of the optical elements restricts the brightness and wavelength of the light they transmit. In order to provide researchers with OAM radiation with the properties available from FELs, new techniques have been developed.

S Sasaki and I McNulty [57,58] were the first to identify that the harmonic radiation emitted in a helical undulator has a helical phase and thus carries an OAM. Preceding experiments observed ring and spiral intensity distributions from FEL radiation suggesting the presence of OAM. Sasaki and McNulty theoretically demonstrated that the harmonic radiation carries OAM, characterised by the OAM index $\ell = \pm(h-1)$ with h the harmonic number and sign dependent on the handedness of the undulator. Intense

radiation carrying OAM is therefore accessible with helical undulators. Experiments confirming the theoretical work measured the OAM in spontaneous undulator radiation [59] and then in the coherent emission from a bunched electron beam radiating at the second harmonic [60]. At Fermi FEL [61], OAM radiation was demonstrated from both the coherent second harmonic emission as well as a spiral zone plate which takes a more traditional approach to convert radiation outside of the FEL. The spiral zone plate was constructed out of silicon in order to not be damaged by the XUX (26 nm wavelength) radiation emitted in the FEL. Most recently, a FEL oscillator was used to generate coherent superposition of two Laguerre-Gaussian modes with azimuthal mode numbers of equal magnitude and opposite sign [62].

E Hemsing, along with colleagues, has produced a large body of theoretical and experimental work concerning OAM radiation in a FEL [63–67]. This includes describing the development of different modes in a FEL and how these modes are affected due to parameters such as diffraction and energy spread. Hemsing has also provided the first method by which OAM radiation is carried by the fundamental frequency of undulator radiation [66]. The method works by pre-bunching the beam into a helix before entering the FEL via harmonic interaction with a seed laser in a helical undulator.

4.1 OAM Content in the Harmonics of Helical Undulators

In Chapter 2, it was shown that there is no harmonic radiation on-axis for all the harmonics of a helical undulator and the odd harmonics of the planar undulator. Off-axis, however, the radiation received is emitted at different points in the electron's trajectory and the harmonics survive. It turns out that the phase of the off-axis harmonic radiation has a dependence on the azimuthal position at which is is observed. The properties of the spontaneous emission by electrons in an undulator is now discussed.

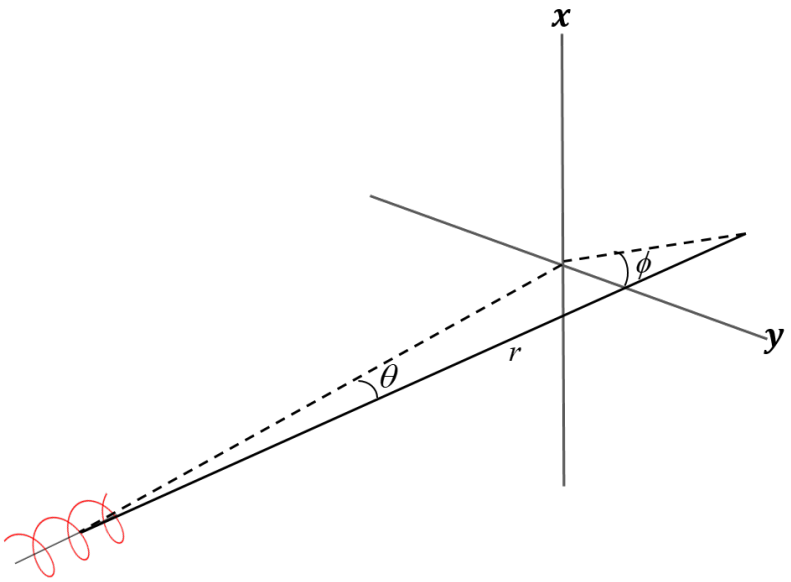

Figure 4.1: Geometry of off-axis emission.

4.1.1 Spontaneous Emission

The electric field radiated from a single electron in the frequency domain can be written as (in SI units) [68]

$$\boldsymbol{E}(\omega) = \frac{ie\omega e^{i\omega r}}{4\pi\sqrt{2\pi}c\epsilon_0 r}\int_{-\infty}^{\infty}\hat{\boldsymbol{n}}\times(\hat{\boldsymbol{n}}\times\boldsymbol{\beta})e^{i\omega(t-\boldsymbol{n}\cdot\boldsymbol{r}_e(t)/c)}\mathrm{d}t, \tag{4.1}$$

where r is the distance from the undulator and $\hat{\boldsymbol{n}} = \boldsymbol{r}/r = \sin\theta\cos\phi\hat{\boldsymbol{x}} + \sin\theta\sin\phi\hat{\boldsymbol{y}} + \cos\theta\hat{\boldsymbol{z}}$ is the unit vector pointing from the origin to the observer. The electron travels through the undulator along the path $\boldsymbol{r}_e(t) = c\int\boldsymbol{\beta}\mathrm{d}t$ where, for a helical undulator, transverse and longitudinal components of $\boldsymbol{\beta}$ are given in equations (2.5) and (2.8).

The electric field gives the angular spectral energy distribution in the far field via

$$\frac{\mathrm{d}^2W}{\mathrm{d}\omega\mathrm{d}\Omega} = 2\epsilon_0 cr^2|\boldsymbol{E}(\omega)|^2. \tag{4.2}$$

Substituting in equation (4.1) gives

$$\frac{\mathrm{d}^2W}{\mathrm{d}\omega\mathrm{d}\Omega} = \frac{e^2\omega^2}{16\pi^3c\epsilon_0}\left|\int_{-\infty}^{\infty}\boldsymbol{n}\times(\boldsymbol{n}\times\boldsymbol{\beta})e^{i\omega(t-\boldsymbol{n}\cdot\boldsymbol{r}(t)/c)}\mathrm{d}t\right|^2. \tag{4.3}$$

For a helical undulator with N_u periods, this can be expressed for the different harmonic frequencies, h, as [69]

$$\frac{\mathrm{d}^2 W_h}{\mathrm{d}\omega \mathrm{d}\Omega} \approx \frac{\mu_0}{8\pi c}\left(\frac{e\omega N_u K}{k_w \gamma}\right)^2 \mathrm{sinc}^2\left[N_u \pi\left(\frac{\omega(1-\beta_z\cos\theta)}{k_w c} - h\right)\right] J_{h-1}^2\left(\frac{\omega K \sin\theta}{\gamma k_w c}\right), \tag{4.4}$$

where J_{h-1} is the Bessel function of the first kind. This term is zero on-axis for all values of h except $h = 1$.

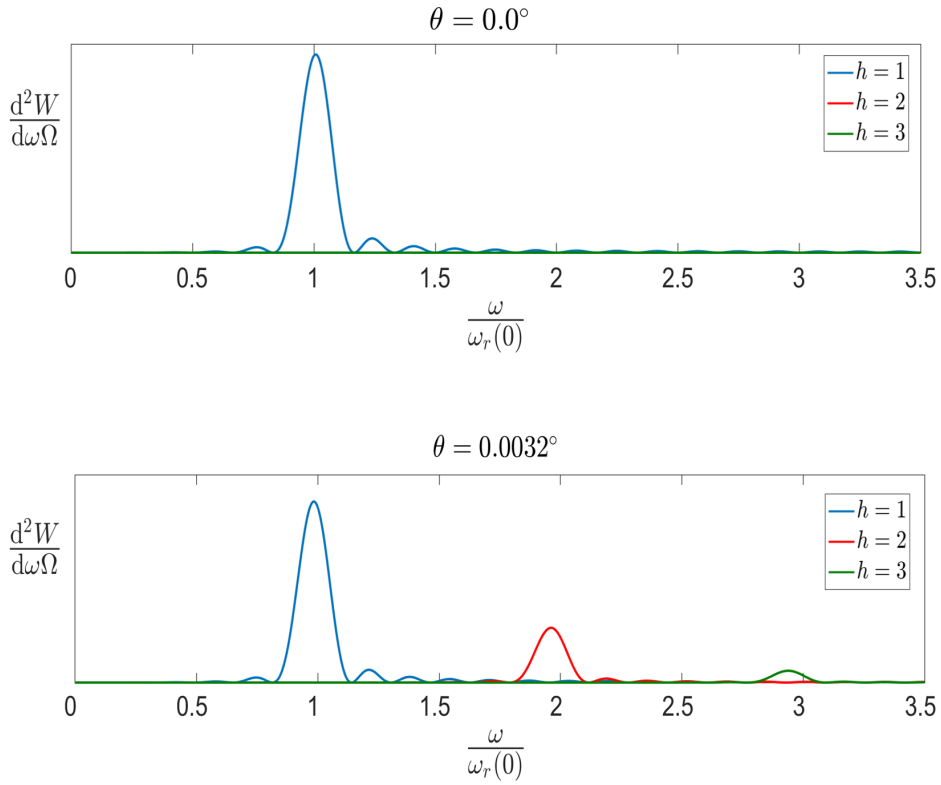

Figure 4.2: On-axis (top) and off-axis (bottom) spectrum of a helical undulator. The parameters used are: $N_u = 6$, $K = 2.634$, $\lambda_u = 0.039$ m, $\gamma = 7869$

Using equation (4.1.1), the spectrum of emission is plotted for the different harmonics shown in Figure 4.2. On-axis, $\theta = 0$, the radiation spectrum contains only the fundamental frequency. Moving off-axis, the spectrum now contains harmonics. In Section 2.2 the resonance condition was derived which has a dependence on θ. This is seen in the figure where the peaks of the spectrum are shifted for $\theta \neq 0$. The

$\text{sinc}^2(x)$ function is peaked when $x = 0$, and thus the peak of the spectrum is found at frequencies

$$\omega_h(\theta) = \frac{hk_w c}{1 - \beta_z \cos(\theta)}. \tag{4.5}$$

From this - for small θ - the resonance condition, equation (2.18), is recovered. The $\text{sinc}^2(x)$ function's FWHM is found when $x = \pm 1.39$, and so the FWHM of each frequency peak is

$$\Delta\omega_h = \frac{0.88}{hN_u}\omega_h(\theta). \tag{4.6}$$

Increasing the number of undulator periods therefore narrows the frequency bandwidth. Similarly, for small angles, the spatial distribution FWHM at the peak frequencies is

$$\Delta\theta \simeq 1/\gamma\sqrt{\frac{0.88}{hN_u}\frac{\omega_h(0)}{\omega_h(\theta)}}. \tag{4.7}$$

Increasing the number of undulator periods therefore also narrows the spatial distribution.

Following [67], numerical calculation of equation (4.1) for second harmonic emission of an electron in a helical undulator is included in Figure 4.3, where the integral is taken over the limits $\pm N_u\lambda_u/2c$. The phase profile of the harmonic emission has an azimuthal variation, which indicates the presence of OAM. There is a slight asymmetry in the intensity profile which indicates that this is not a single $\ell = \pm 1$ mode, but that there are small contributions from other modes, notably the $\ell = 0$ modes.

Explicit calculation of equation (4.1) presented in [67] finds the transverse electric fields to be (for small forward angles)

$$\begin{aligned} E_x \approx \mp\frac{ie\omega}{4\pi\sqrt{2\pi}c\epsilon_0 r}\frac{N_u\pi}{w_u}e^{i\omega r}\text{sinc}\left[N_u\pi\left(\frac{\omega(1-\beta_z\cos\theta)}{k_w c} - h\right)\right] \\ \times J_{h-1}^2\left(\frac{\omega K\sin\theta}{\gamma k_w c}\right)(\pm 1)^{h-1}e^{\pm i(h-1)\phi} \end{aligned} \tag{4.8}$$

and

$$E_y = \mp iE_x. \tag{4.9}$$

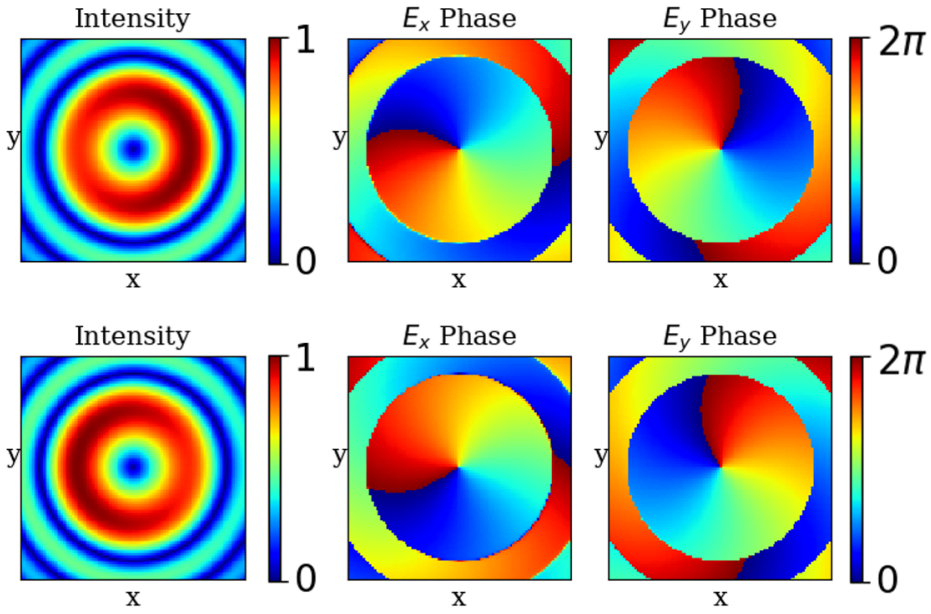

Figure 4.3: Second harmonic emission from an electron in a helical undulator, where emission is given by equation (4.1). Parameters used are: $N_u = 32$, $K = 2.3$, $\lambda_u = 0.039$ m, $\gamma = 7869$. Top: An LHU produces an $\ell = -1$ vortex beam with right-hand circular polarisation. Bottom: An RHU produces an $\ell = 1$ vortex beam with left-hand circular polarisation.

An azimuthal dependence on the phase has been revealed for $h > 1$. It is shown that the higher harmonics have acquired a phase term $e^{i(h-1)\phi}$ and so the harmonics have an OAM index $\ell = \pm(h-1)$. The transverse components have a fixed $\pm\pi/2$ difference as radiation emitted is circularly polarised and so also carry a spin angular momentum $\sigma = \mp$. The OAM arises separately from the polarisation, however, both are consequences of the trajectory of the electron through the undulator and thus it is not possible to flip the handedness of the OAM without also flipping the handedness of the polarisation. Table 4.1 summarises the polarisation and transverse modes profiles for different undulator configurations.

In the Table, the radiation is described in terms of the transverse modes introduced in Chapter 4. For a single electron, the emitted radiation is not strictly the *LG* modes. However, for an electron beam with a Gaussian transverse profile with beam waist $\sigma_x > \gamma\sqrt{N_u}/k$, the angles of electron emission are restricted by the electron beam

Table 4.1: The polarisation and transverse modes emitted in different undulator configurations.

Undulator	Polarisation	Transverse mode
LH Helical	RH circular	$LG_{0,-(h-1)}$
RH Helical	LH circular	$LG_{0,+(h-1)}$
x-Poled Planar	y linear	$HM_{0,(h-1)}$
y-Poled Planar	x linear	$HM_{(h-1),0}$

waist and, for large N_u and K, the field becomes a close approximation of the LG modes.

The higher harmonic radiation from planar undulators also has transverse phase variation. This radiation is best described by the HG modes with nodal lines along the same axis as the electron oscillation. The HG modes and the corresponding polarisation emitted by different undulators are also included in Table 4.1.

4.1.2 Accessing Harmonic Radiation

The fundamental wavelength, which has a Gaussian transverse profile, dominates the undulator radiation spectra after several gain lengths. However, an electron beam can be prepared with a micro-bunching structure in order to stimulate emission at the higher harmonics.

Afterburner undulators

Undulators which are placed downstream of a main - usually planar - undulator amplification section once micro-bunching has been established, are called 'afterburners'. Afterburners are increasingly being explored as a method to tailor FEL output in different ways and provide solutions to enable specific experimental output requirements (e.g. provide polarisation control [4]) with minimal changes to an existing facility and therefore at relatively low cost. Much of the research in this thesis will focus on different afterburner configurations due to the feasibility of implementing afterburner type setups at real facilities. For OAM generation, pre-bunching electron beam at a har-

monic of a helical afterburner means the coherent radiation emitted in the afterburner will be in an LG mode.

The coherent emission for a beam of N_e electrons is given by

$$\frac{\mathrm{d}^2 W_C}{\mathrm{d}\omega \mathrm{d}\Omega} = N_e^2 F(\omega) \frac{\mathrm{d}^2 W}{\mathrm{d}\omega \mathrm{d}\Omega}, \tag{4.10}$$

where $F(\omega)$ is the form factor for the electron beam. The form factor for a Gaussian electron beam is [67]

$$F(\omega) = b^2 \mathrm{sinc}^2 \left[\frac{\tau}{2}(\omega_b - \omega\cos\theta)\right] e^{-\sigma_x^2 \frac{\omega^2}{c} \sin^2\theta}, \tag{4.11}$$

where τ is the length of the beam. The form factor picks out part of the spontaneous emission spectrum as well as limiting the angles of emission to $\theta < c/\sigma_x\omega$ where ω_b is the frequency of the bunching. If ω_b is a harmonic of the undulator then the radiation emitted is also at the second harmonic and will have the form of an LG_0^{h-1} mode. Detuning the helical afterburner so that the bunching is lower than $\omega_h(0) > \omega_b$ will push the radiation off-axis which can improve the purity of the LG mode emitted as well as the intensity.

For a single helical afterburner emitting OAM radiation at the second harmonic the radiated coherent power

$$P = 4P_b b^2 \frac{I_0}{\gamma I_A} \left(\frac{K^2}{1+K^2}\right)^2 \ln\left(\frac{1+4N^2}{4N^2}\right), \tag{4.12}$$

where P_b is the peak electron beam power, I_A= 17 kA is the Alfven current, and $N = k\sigma_x^2/L_u$ is the Fresnel number of the electron beam with $k = 2\pi/\lambda_b$, and $L_u = N_u\lambda_u$ the length of the undulator. This is orders of magnitude lower than the power that would be emitted if the afterburner was emitting at the fundamental wavelength.

4.2 Modelling OAM Radiation with the FEL Simulation Code Puffin

The most prevalent FEL simulation code is Genesis [70]. This code, like many others, applies several approximations, which substantially decreases the code's computation time. Significant to this thesis is the approximation that the FEL equations can be averaged over an undulator period. Genesis solves the FEL equations for individual resonant period length slices of radiation and electron beam, adding slippage between the electrons and the radiation field after every one resonant period of numerical integration. This averaging gives sufficient modelling of basic FEL operation, however, it limits the resolution of processes to the resonant wavelength scale and above (although some functionality has been added to model higher harmonics of planar undulators [71]). The OAM content contained in the second harmonic of coherent spontaneous emission is washed out in the process of averaging. Therefore codes which apply this averaging are not suitable for modelling many OAM/FEL schemes.

The simulations presented in this thesis use the FEL simulation code Puffin [72,73]. In contrast to most other FEL codes, Puffin does not average the electron motion over an undulator period, allowing modelling of both planar and helical harmonic emission arising from electron motion at the sub-undulator period scale. The Puffin code also does not utilise the slowly varying envelope approximation, although the paraxial approximation is made. The omission of many of the approximations used by other codes makes Puffin ideal for modelling many novel FEL schemes including the ones presented in this thesis.

The Puffin code is developed and available on GitHub [74]. Puffin is a parallel numerical solver for unaveraged FEL equations, it is written in Fortran 90 and uses MPI and OpenMP. The Puffin code was modified to allow simulation of the FEL methods presented in this thesis. To model the work included in Chapter 5, the code was modified to apply a transfer matrix to the electrons which represent skew quadrupole magnets and a rotation to the electrons along the longitudinal axis. To model the work included in Chapter 6, the code was given the functionality to change the handedness

of the helical undulators simulated.

4.2.1 Time-saving Modes

Since Puffin does not employ the same approximations as other FEL codes, it uses significantly more computation time which is expensive as well as time-consuming. In order to save computational resources, Puffin provides two optional time-saving modes which can be turned on and off. The first employs the plane wave approximation - essentially modelling the FEL in 1D. This is useful for fast simulations when the temporal properties of the FEL radiation pulse are being investigated, however, as OAM is a property of radiation with transverse phase variation, 1D simulations cannot model OAM beams.

The second time-saving option is to model a slice of the electron beam by imposing periodic boundaries. The simplest option is to model one resonant wavelength of electron beam - this is the steady-state approximation. This allows modelling of radiation with OAM, however, the simulations are time-independent and temporal effects are not modelled. The length of the slice modelled can be increased to better simulate density variations across the electron beam, but full temporal simulations will provide the most accurate picture.

4.2.2 OAM Content at the Second Harmonic

Figures 4.4and 4.5 shows the 2D and 3D radiation field of the second harmonic of helical undulators. The simulations utilised Puffin's periodic mode and use parameters inspired by CLARA [75] with planar undulators exchanged for helical undulators. The plots are shown close to saturation with the second harmonic of the radiation filtered from the full radiation field. The spiral pattern in the field indicates the presence of (diffracted) OAM radiation.

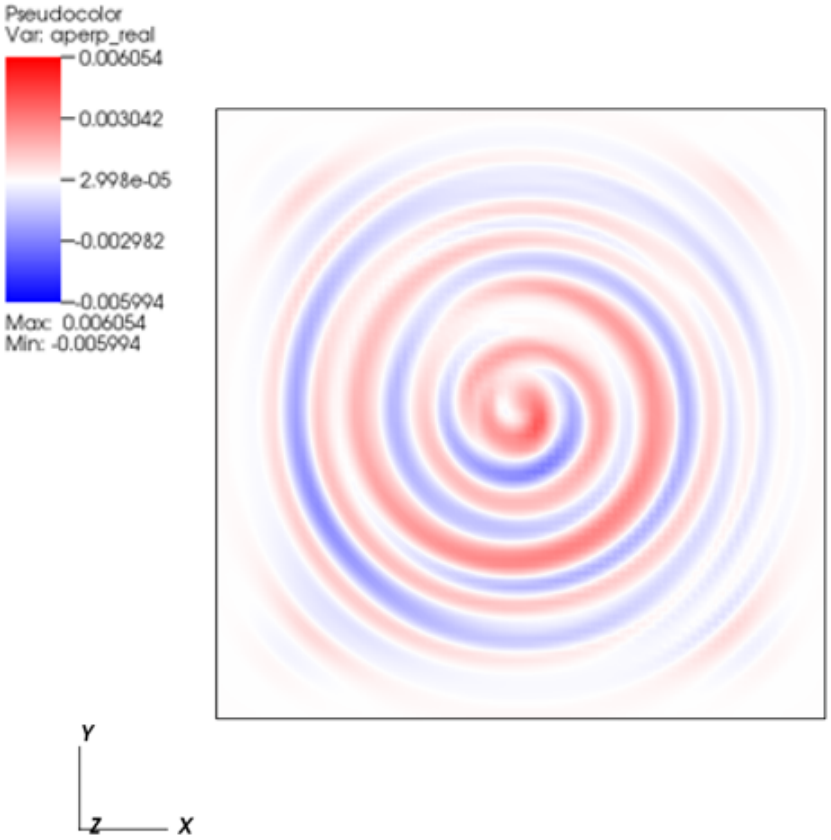

Figure 4.4: 2D plot of the 2nd harmonic radiation field from a helical undulator. The FEL is modelled using the FEL simulation code Puffin.

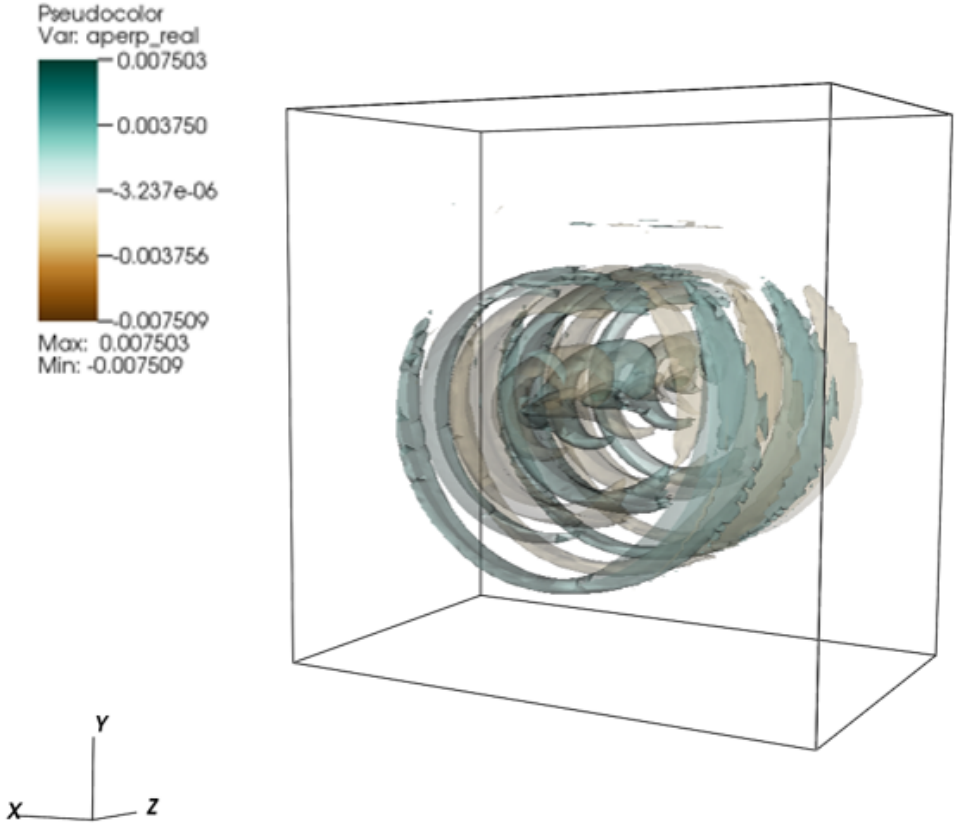

Figure 4.5: 3D plot of the 2nd harmonic radiation field from a helical undulator. The FEL is modelled using the FEL simulation code Puffin.

Chapter 5

Investigating OAM Radiation Start-up from SASE

This chapter investigates a scheme to produce OAM light at the fundamental wavelength of the undulator. Whereas previous methods generating fundamental wavelength OAM light have relied on seeding the FEL, either with an OAM seed or with a pre-bunched electron beam, this chapter proposes a method where the initial seed comes from the shot noise in the electron beam. For methods requiring the FEL to be seeded, the output is restricted by the quality of seeds available. This can mean very short wavelengths are unavailable through seeding schemes as a suitable seed laser may not be accessible at the required wavelength with an intensity large enough to overcome the initial shot noise in the beam. Here, the feasibility of selecting for radiation with OAM through a method that works *in situ* is considered, which would generate high powered OAM radiation at the full wavelength range of FELs.

The method presented here relies on the rotation of an electron beam. This proved a difficult task, and, although a rotation of the electron beam was demonstrated, physical rotation of the electron beam caused a debunching effect in the electron beam which washed out any FEL gain. Although ultimately unsuccessful, the work is still presented here as it is an interesting demonstration of the mechanisms for transverse mode selection in a FEL.

5.1 Competing Modes

Electrons enter the undulator with random phases due to shot noise in the electron gun. In the self amplified spontaneous emission (SASE) mode of operation, the initial amplitude due to the noise acts as a seed for the FEL interaction and is amplified. The incoherence of the electrons is mimicked by the radiation they produce. This incoherent radiation can be described as a superposition of all the modes which make up an orthogonal basis set. As they carry OAM, the *LG* modes are chosen and the radiation is expressed as

$$E(\phi, \hat{r}) = \sum_{\ell=-\infty}^{\infty} \sum_{p=0}^{\infty} a_{p,\ell} LG_{p,\ell}(\phi, \hat{r}), \tag{5.1}$$

where $a_{p,l}$ is the initial mode amplitude. The noise in the electron beam seeds all modes. However, the coupling between the electron beam and the radiation modes reduces with increasing $|\ell|$ due to the null intensity at the centre of the higher-order modes - which is larger for larger $|\ell|$. Therefore, the transverse profile of the higher-order modes means they have longer gain lengths [64] with the shortest gain length belonging to the Gaussian mode. The Gaussian mode, consequently, dominates FEL interaction, suppressing the higher-order modes, leading to the Gaussian mode of operation typical of a FEL.

5.2 Suppression of the Gaussian Mode

It is possible to disrupt the interaction between electrons and radiation by imposing a relative phase shift between the electrons and the radiation field. Through successive phase shifts between short undulator modules, the FEL interaction can be suppressed. In a paper by Brian McNeil and colleagues [76], it was proposed that this could be used to induce harmonic lasing in a FEL. It was shown that a longitudinal delay of electrons, which can be imposed by chicane modules, will cause different relative phase shifts between the electrons and the different harmonic wavelengths emitted in a FEL. A longitudinal delay that causes a phase shift, $\Delta\theta$, relative to the fundamental

wavelength will then cause a phase shift, $n\Delta\theta$, relative to the nth harmonic. The exponential gain of radiation at the fundamental frequency was suppressed by repeated shifts when $\Delta\theta$ was chosen to be non-integer multiples of 2π. The disruption of the fundamental wavelength then allows growth in the power of the harmonic radiation. Instead of considering higher frequency harmonics of the radiation emitted in a FEL, this chapter considers the LG modes emitted at the fundamental frequency.

The transverse phase structure of the LG modes provides an additional route to impose a phase shift on the light. An electron rotated round the longitudinal axis of a higher-order LG beam experience the same phase shift as from a longitudinal shift. For a rotational shift, $\Delta\phi_r$, of the electron beam, the electrons experience a phase shift, $\ell\Delta\phi_r$, relative to an LG mode.

For an LG mode with OAM index ℓ, the total phase change, $\Delta\Psi_\ell$, between radiation and the electrons from the combination of a longitudinal and rotational shift is therefore

$$\Delta\Psi_\ell = \Delta\theta + \ell\Delta\phi_r. \tag{5.2}$$

It is clear from equation (5.2) that through careful selection of $\Delta\theta$ and $\Delta\phi_r$, different relative phase changes between the electrons and the OAM modes can be achieved. Notably, a rotational shift in the electron beam has no effect on radiation with a Gaussian profile. If successive repetition of the shifts are chosen to cause the exponential gain of the Gaussian mode to be disrupted - such that the gain length of the Gaussian mode is longer than of the higher-order modes - then a dominant OAM mode will self-select for amplification. This is modelled in the next section.

5.3 Simulations

The simulations presented in this sections use parameters based on the LCLS facility [3], given in Table 5.1. The selected parameters mean that the radiation emitted is in the hard x-ray wavelength range.

5.3.1 Rotation

The Puffin code was modified in order to add a rotation to the electrons along the longitudinal axis according to the rotation matrix,

$$R(\Delta\phi_r) = \begin{bmatrix} \cos\Delta\phi_r & 0 & -\sin\Delta\phi_r & 0 \\ 0 & \cos\Delta\phi_r & 0 & -\sin\Delta\phi_r \\ \sin\Delta\phi_r & 0 & \cos\Delta\phi_r & 0 \\ 0 & \sin\Delta\phi_r & 0 & \cos\Delta\phi_r \end{bmatrix}, \tag{5.3}$$

which acts on the phase space vector constructed from the vaiables (x, p_x, y, p_y), where x and y are the transverse co-ordinates, and p_x and p_y are the conjugate of momenta.

Table 5.1: Parameters based on LCLS

Parameter	Value
Electron beam energy [GeV]	13.6
Peak current, I_0 [kA]	3
rms energy spread σ_γ/γ	1.0×10^{-4}
Normalised emittance [mm-mrad]	0.4
rms beam size σ_x [μm]	16
Undulator period λ_u[cm]	3.0
rms undulator parameter $\overline{a}_u$	2.48
Resonant wavelength λ_r [Å]	1.5
Number of undulator periods per module	144
Number of undulator modules	17

5.3.2 Results

The rotation is applied - along with a longitudinal shift - between undulator modules each around a gain length long. In order to alter mode competition to select for a LG_{01} mode, the shift pairs are chosen so that $\Delta\Psi_1 = 2\pi$. The setup utilizes three alternating pairs of shifts, the longitudinal shifts, $\Delta\theta = \pi/2, \pi$ and $3\pi/2$ and the corresponding rotational shifts $\Delta\phi_r = 3\pi/2, \pi$ and $\pi/2$ respectively. These sections are repeated until the radiation reached saturation.

The relative electron/radiation phase change for the Gaussian and $\ell = -1$ modes

from these shifts are non-integer multiples of 2π. It can be seen from Figure. 5.1 that the gain in these modes has been disrupted. Suppressing the competing transverse modes means the $LG_{0,1}$ mode dominates the interaction. This causes the $LG_{0,1}$ mode to grow over an order of magnitude above the Gaussian mode. Also included in Figure. 5.1 is the bunching factor for the different helical modes which is defined as [77]

$$b_\ell = \langle \exp(i\theta_j - i\ell\phi) \rangle, \tag{5.4}$$

where the brackets indicate the ensemble average over the whole electron beam. The b_1 factor has exponential growth as the electrons propagate through the undulator. The electrons are bunched in a helical distribution which translates to a helical distribution in the radiation the electrons emit. This phase distribution is plotted in Figure. 5.2 at a point close to saturation. The intensity of the radiation is also included in the figure displaying the ring structure typical of helically phased beams.

Figure 5.3 compares growth in the $LG_{0,0}$ and $LG_{0,1}$ modes with and without the phase shifts introduced. The figure shows how the $LG_{0,1}$ mode increases when the $LG_{0,0}$ mode is reduced. This demonstrates that the OAM operation is not solely from a reduction in the power in the Gaussian mode but an increase in power $\ell = 1$ mode. The suppression of the interaction of the Gaussian modes has induced exponential interaction with the higher-order transverse modes. Importantly, the final power of the FEL is similar regardless of the dominant mode.

5.4 Issues with Rotating an Electron Beam

The simulations which have been presented used the point transform given by equation (5.3). A beamline that will rotate an electron beam through an arbitrary angle was developed with collaborators and presented in [78]. Although the required rotation was achieved, the method requires several skew quadrupole magnets with strong fields and the total length of the rotation beamline, approximately 5 m, is significant. Ultimately, it was found that the effect of the beamline on the longitudinal phase (z) of the electrons had the effect of washing out all bunching in the beam. Variations in

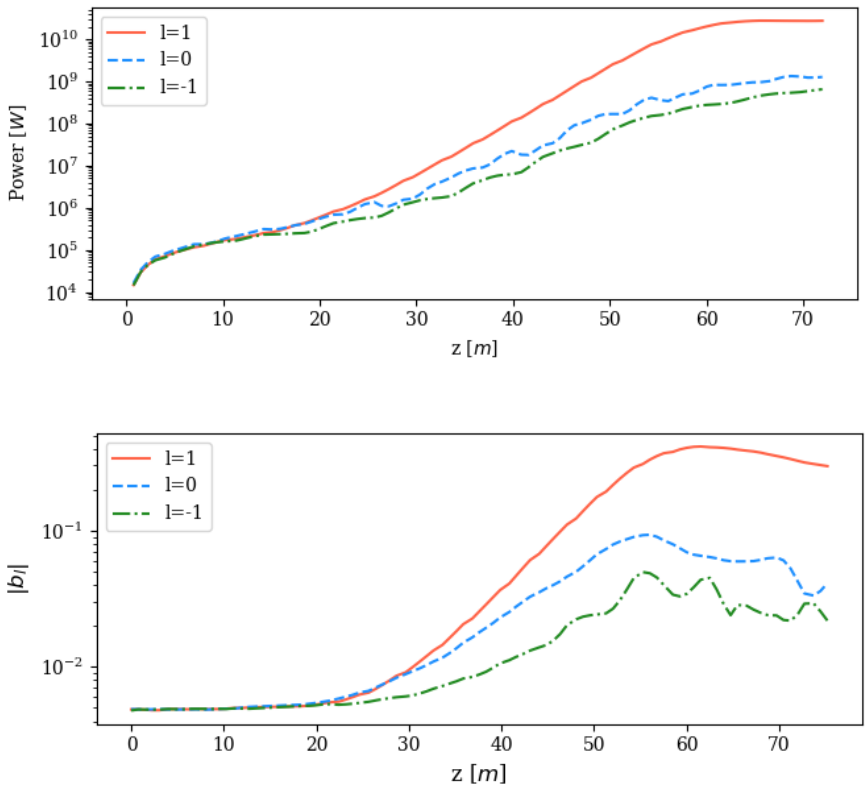

Figure 5.1: Power decomposition into Laguerre-Gaussian modes (top) and helical micro-bunching factor (bottom) when the phase shifts $\Delta\theta = \pi$, $\Delta\phi_r = \pi$ and $\Delta\theta = 3\pi/2$, $\Delta\phi_r = \pi/2$ are imposed between undulator modules. This results in the most power being contained in the $LG_{0,1}$ mode.

the transverse components of momentum change the z component of momentum p_z. Since the electrons will have different transverse momentum, depending on their distance from the beam radius, this causes a different longitudinal momentum variation for different electrons and leads to a debunching of the electron beam.

The debunching of the electrons is likely to be the outcome for any method used to rotate the electron beam as the transverse displacement of the electrons, when rotated, is dependent on the distance from the centre of the electron beam. As the radius of the electron beam is many orders of magnitude greater than the radiation wavelength, the variation in longitudinal position resulting from a rotation will be significant in the scale of the radiation. It may still be possible to reduce the effect of debunching

by compensating for the transverse variation in longitudinal momentum; however, this wasn't achieved in this work.

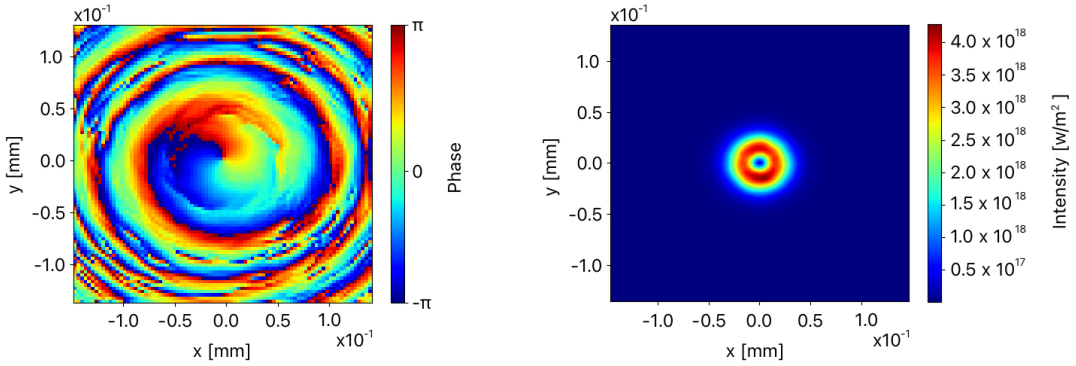

Figure 5.2: Phase (left) and intensity (right) at $z = 55.25m$ when the phase shifts $\Delta\theta = \pi$, $\Delta\phi_r = \pi$ and $\Delta\theta = 3\pi/2$, $\Delta\phi_r = \pi/2$ are imposed between undulator modules.

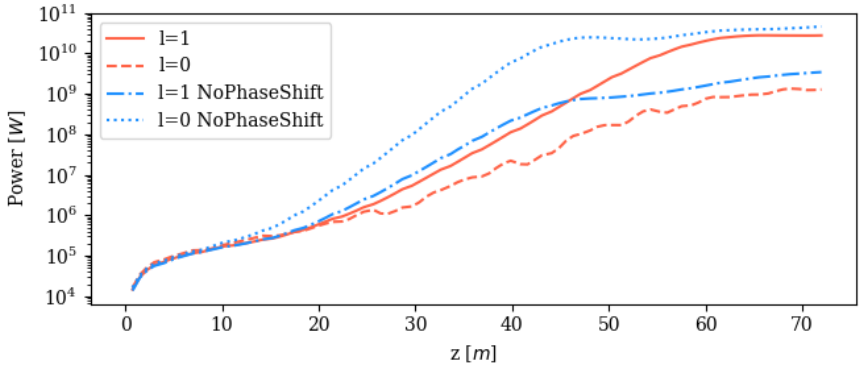

Figure 5.3: Comparison of the power growth in the LG_{00} and LG_{01} with and without phase shift introduced between undulator modules.

Chapter 6

Poincaré Beam Generation

The higher-order transverse modes are examples of light which is spatially structured in both intensity and phase. Superimposing two of these modes with orthogonal polarisation will produce beams which will have an additional spatial structure in the polarisation. Polarisation is important when considering light's interaction with matter. The majority of past research has concentrated on light with polarisation which does not vary with transverse spatial coordinate, such as linear, elliptical or circular polarisation. However, as research has progressed, there has been an increase in the need for the generation of custom light fields and there has been growing interest in vector, or Fully Structured Light (FSL), beams with spatially-varying polarisation states [79–81]. As discussed in Chapter 4, the higher harmonics of the FEL radiation are well described by the LG or HG modes - the work presented in this chapter investigates exploiting the structure of harmonic FEL radiation to generate light which is also structured in polarisation.

6.1 Motivation

Polarisation can be structured in different polarisation distributions. The different distributions give the beams additional, beneficial properties which are useful in a number of applications. For example, beams with radially orientated linear polarisation can be focused more tightly than those with spatially homogeneous linear polarisation, with

applications in laser machining, optical nano-probing, and nano-lithography [79,82,83]. Beams with transversely structured polarisation have also been shown to propagate more stably in self-focussing nonlinear media [84]. In general, the ability to control both the intensity and the polarisation of FSL beams may provide a useful method for applications in material processing [85], microscopy [86], and in atomic state preparation, manipulation and detection [87,88].

The generation of FSL beams commonly relies upon methods that use external conversion optics to superimpose orthogonally-polarised transverse modes, including interferometric techniques [89, 90]. While earlier works have produced OAM vortex beams in the x-ray [91,92], there are, as yet, insufficient optical methods to superimpose OAM beams to generate the Poincaré x-ray beams described here. Generation of a class of FLS beams called cylindrical vector beams has been demonstrated in the ultraviolet using higher harmonic generation [93] and vector beams from synchrotron light sources have been demonstrated using crossed helical undulators and band-pass filter which filters out the second harmonic radiation [94].

Generation of FSL in the X-ray using Free Electron Lasers is predicted to open up new unexplored areas of atomic and molecular science. One such area is in the field of mirror image chiral molecules, either left or right handed, also called enantiomers. When subjected to FSL, a discriminatory optical force in opposite directions can result for each enantiomer [95].

6.2 Structured Light

Before a method for producing FSL at modern FEL facilities is presented, background material detailing the form of these beams is needed. To start, consider what happens when Laguerre-Gaussian modes are combined.

6.2.1 The Scalar Combination of Laguerre-Gaussian Modes

The superposition of two LG beams with equal amplitude, ϵ, the same polarisation vector $\hat{\boldsymbol{e}}$ can be expressed as

$$\boldsymbol{E} = \epsilon(LG_{0,\ell_1} + LG_{0,\ell_2})\hat{\boldsymbol{e}}. \tag{6.1}$$

The structured phase profile of the different LG beams means the transverse intensity profile sees areas of constructive and destructive interference. An interesting case arises when the two beams have azimuthal mode numbers with equal magnitude and opposite sign, $\ell_1 = -\ell_2$. The phase profiles then are mirror images of each other; changing in opposite azimuthal directions. The intensity of the combined field is plotted in Figure 6.1; the result is an intensity profile structured in a *petal* pattern where the number of petals is $2|\ell_1| = 2|\ell_2|$ [96, 97]. These patterns can be used to quantify the ℓ of a beam by interfering it with itself reflected in a mirror.

The interference of two transverse modes with the same polarisation can generate a new structure in the intensity and phase of the radiation, but the polarisation remains constant across the beam. In order to structure the polarisation, transverse modes with different polarisation must be superimposed.

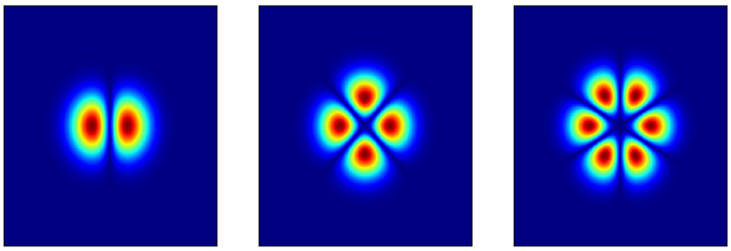

Figure 6.1: Scalar combination of two Laguerre-Gaussian beams with $\pm\ell$ for (left to right) $|\ell| = 1, 2, 3$

6.2.2 The Vector Combination of Laguerre-Gaussian Modes

In the simplest form, FSL beams can be described by a vector superposition of two orthogonally polarised spatial eigenmodes

$$\boldsymbol{E}(\boldsymbol{r},\boldsymbol{\phi}) = E_1(\boldsymbol{r},\boldsymbol{\phi})\hat{\boldsymbol{e}}_{\mathbf{1}} + e^{i\beta}E_2(\boldsymbol{r},\boldsymbol{\phi})\hat{\boldsymbol{e}}_{\mathbf{2}}, \tag{6.2}$$

where β is the phase between the two modes and $\hat{\boldsymbol{e}}_{\mathbf{1}}$ and $\hat{\boldsymbol{e}}_{\mathbf{2}}$ are orthogonal polarisation vectors.

For cylindrically symmetric beams, the LG set of tansverse modes and circular polarisation basis is adopted, where $\hat{\boldsymbol{e}}_{\mathbf{1}} = \hat{\boldsymbol{e}}_{\boldsymbol{L}} = (\hat{\boldsymbol{e}}_x + i\hat{\boldsymbol{e}}_y)/\sqrt{2}$ and $\hat{\boldsymbol{e}}_{\mathbf{2}} = \hat{\boldsymbol{e}}_{\boldsymbol{R}} = (\hat{\boldsymbol{e}}_x - i\hat{\boldsymbol{e}}_y)/\sqrt{2}$ correspond to left and right handed circular polarisation vectors, respectively. The resultant spatial distribution of the polarisation is controlled by the superposition of the modes

$$\begin{aligned} E_1(\boldsymbol{r},\boldsymbol{\phi}) &= \epsilon_L LG_{p_L,\ell_L}, \\ E_2(\boldsymbol{r},\boldsymbol{\phi}) &= \epsilon_R LG_{p_R,\ell_R}, \end{aligned} \tag{6.3}$$

where ϵ_L and ϵ_R are the field mode amplitudes [47]. If either E_1 or E_2 is zero, then the resultant beam is an LG mode with spatially uniform circular polarisation. However, if E_1 or E_2 represent different LG modes, the resultant beam will have spatially variant states of polarisation. Two classes of light are considered in this work - cylindrical vector beams and full Poincaré beams.

Cylindrical Vector Beams

If the two modes have equal amplitudes and the same OAM ($\ell_L = \ell_R$), the resultant beam will have spatially uniform linear polarisation. If they have equal amplitudes and equal but opposite OAM ($\ell_L = -\ell_R$), however, the resultant Cylindrical Vector (CV) beam [79, 81] will have an azimuthally varying linear polarisation distribution. The phase difference β determines the distribution. For $\beta = 0, \pi, \pi/2$, the CV beam will have a radial, azimuthal or spiral distribution respectively.

Full Poincaré Beams

If the two modes have different magnitudes of OAM, the resultant 'full Poincaré' beam will carry a net OAM and the polarisation will vary in both the azimuthal and radial co-ordinates and may contain all states of polarisation: linear; elliptical; and circular [80]. Typical examples are the so-called 'lemon' and 'star' beams [98].

Ideal *LG* beams, described by equation 3.14, are combined computationally and plotted in Figure 6.2. Examples of both CV and Full Poincaré beam are included. The polarisation ellipse is plotted in order to map the polarisation distribution of the different beams. Further detail on the mapping of polarisation is provided in Section. 6.2.3.

The examples above described FSL in terms of the *LG* modes. But, of course, the *LG* can be transformed into *HG* modes and vice versa. For beams with Cartesian symmetry, the profiles may be better expressed as *HG* modes [99] and with linear polarisation vectors $\hat{\boldsymbol{e}}_1 = \hat{\boldsymbol{e}}_x$, $\hat{\boldsymbol{e}}_2 = \hat{\boldsymbol{e}}_y$.

6.2.3 Mapping Polarisation

In order to understand the polarisation structure in the beam, there needs to be a method for mapping the polarisation across the beam. By plotting a polarisation ellipse, the state of polarisation can be plotted at each point on the field. A polarisation ellipse provides a method to visualise the state of polarisation, however, the ellipticity and the orientation of the ellipse are not easily measurable. The Stokes parameters are observables that can be used to define the polarisation of field and from them, the polarisation ellipse can be created.

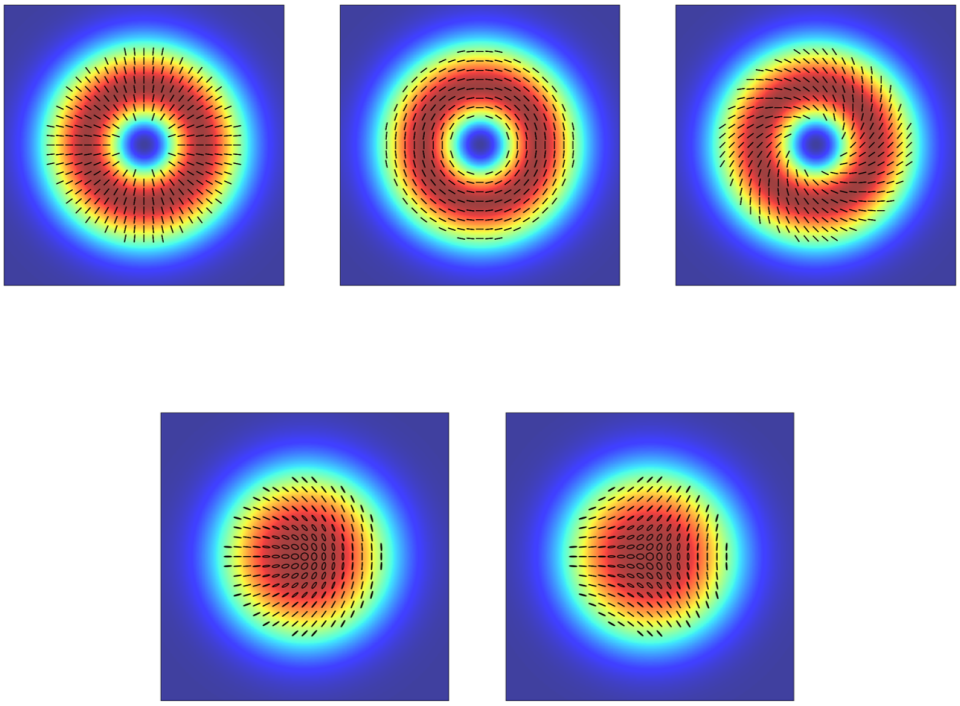

Figure 6.2: The vector combination of two spatial eigenmodes produces different polarisation distributions for different mode combinations. The polarisation distributions are visualised by plotting the polarisation ellipse on top of the intensity profile.
Top: Cylindrical vector beams are produced by the superposition of beams where $\ell_L = 1$, $\ell_R = -1$. The phase $\beta = 0, \pi, \pi/2$ between the two beams changes the distribution to either (left to right) radial, azimuthal or spiral respectively. Bottom: Full Poincaré beams with the distributions (left to right) 'lemon' and 'star' where, respectively, $\ell_L = 0$, $\ell_R = 1$ and $\ell_L = 1$, $\ell_R = 0$.

The Stokes parameters can be directly measured from a field as

$$\begin{aligned} S_0 &= |E_x|^2 + |E_y|^2 = |E_{45}|^2 + |E_{135}|^2 = |E_R|^2 + |E_L|^2, \\ S_1 &= |E_x|^2 - |E_y|^2 = 2\,\mathrm{Re}(E_{45}^* E_{135}) = 2\,\mathrm{Re}(E_R^* E_L), \\ S_2 &= 2\,\mathrm{Re}(E_x^* E_y) = |E_{45}|^2 - |E_{135}|^2 = 2\,\mathrm{Im}(E_R^* E_L), \\ S_3 &= 2\,\mathrm{Im}(E_x^* E_y) = 2\,\mathrm{Im}(E_{45}^* E_{135}) = |E_R|^2 - |E_L|^2, \end{aligned} \tag{6.4}$$

where the subscripts denote the appropriate field components of: linear; linear ro-

tated at angles 45° and 135°; and circular polarised lights [100]. The linear horizontal/vertical, diagonal linear, and circular polarisation are described by S_1, S_2, and S_3, respectively. The Stokes parameters can be normalised to the intensity Stokes parameter via

$$s_i = \frac{S_i}{S_0}, \tag{6.5}$$

for $i = 0, 1, 2, 3$. If the light is fully polarised then $s_0^2 = s_1^2 + s_2^2 + s_3^2 = 1$. The normalised Stokes parameters can be arranged into a column matrix, which gives the normalised Stokes vector

$$\boldsymbol{s} = \frac{1}{S_0}\begin{pmatrix} S_1 \\ S_2 \\ S_3 \end{pmatrix} = \begin{pmatrix} s_1 \\ s_2 \\ s_3 \end{pmatrix}. \tag{6.6}$$

The normalised Stokes vector can be visualised as a unit vector that points to the position on the Poincaré sphere where the polarisation lies. The Poincaré sphere is a method to visualise light's polarisation by plotting the normalised Stokes parameters for polarisation in 3D space. Pure states of polarisation then lie on a sphere with radius equal to 1, where the poles of the sphere represent right or left circular polarisation and the equator represents linear polarisation states with varying orientation. Figure 6.3 provides a plot of the Poincaré sphere and a normalised Stokes vector with arbitrary polarisation.

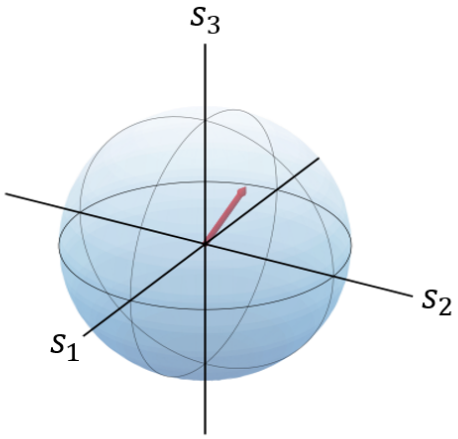

Figure 6.3: Poincaré sphere and normalised Stokes vector for an arbitrary polarisation.

As well as being a useful visualisation tool in itself, the Poincaré sphere provided a method for translating the Stokes parameters into angles which can be used to create a polarisation ellipse. For a single polarisation at a point on the surface of the Poincaré sphere, the nomalised Stokes parameters can be expressed in tems of the latitude angle, 2χ, and longitude angle, 2ψ as

$$\begin{aligned} s_1 &= \cos(2\chi)\cos(2\psi), \\ s_2 &= \cos(2\chi)\sin(2\psi), \\ s_3 &= \sin(2\chi). \end{aligned} \tag{6.7}$$

These equations can then be rearranged to find the ellipticity, $-\pi/4 \leq \chi \leq \pi/4$, and the orientation, $0 \leq \psi \leq \pi$, of a polarisation ellipse [101],

$$\chi = \frac{1}{2}\sin^{-1}(s_3), \tag{6.8}$$

$$\psi = \frac{1}{2}\tan^{-1}(\frac{s_2}{s_1}). \tag{6.9}$$

Figure 6.4 shows how these values construct the ellipse which can then be plotted at each point in the field map polarisation as in Figure 6.2. If the light is linearly polarised, $\chi = 0$, the polarisation ellipse is plotted as a straight line, whereas pure circular polarisation produces a circle. The handedness of the polarisation is not displayed in the shape of the ellipse and so it is common to colour the ellipses to indicate handedness.

6.3 Method of Generating Poincaré Beams in a FEL

The proposed method for generating Poincaré beams is simple; control of the polarisation in the transverse plane is obtained through the overlap of different coherent transverse light distributions radiated from a bunched electron beam in two consecutive orthogonally polarised undulators. Different transverse profiles are obtained by emitting at a higher harmonic in one or both of the undulators. This method enables the generation of beams structured in their intensity, phase, and polarisation - so-called

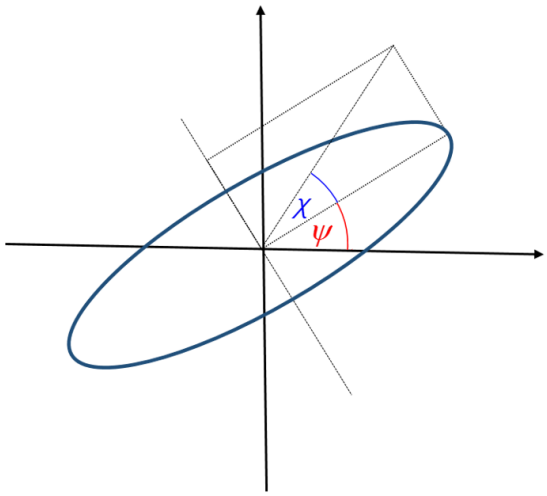

Figure 6.4: A polarisation ellipse defined in terms χ and ψ which are calculated using the Stokes vectors.

Poincaré beams - at high powers with tunable wavelengths.

The radiation output from a FEL is typically a transverse Gaussian mode with nearly full transverse coherence and a spatially homogeneous polarisation that is determined by the magnetic undulator fields (planar, helical, or elliptical). A typical X-ray FEL facility uses planar undulators to micro-bunch the electrons, which therefore generates linear polarised light. One method to enable polarisation control is adding additional undulators placed downstream of the main planar undulator amplification section once micro-bunching has been established [102]. In Chapter 4, it was shown that the higher-order transverse modes can be accessed by a similar afterburner configuration by tuning the afterburner to a sub-harmonic of the electron bunching.

It follows that FSL can be generated in a FEL afterburner by combining the methods for polarisation control and transverse mode generation. The proposed method is outlined in Figure 6.5. The electron beam is first sent through a long undulator section which established bunching in the electron beam. The primary FEL radiation pulse energy emitted in this section can also be strongly suppressed (but the electron beam bunching preserved) by using an undulator with reverse tapering [4] and by electron beam steering [103], so that only the radiation pulse generated in the afterburner is

delivered to experiments.

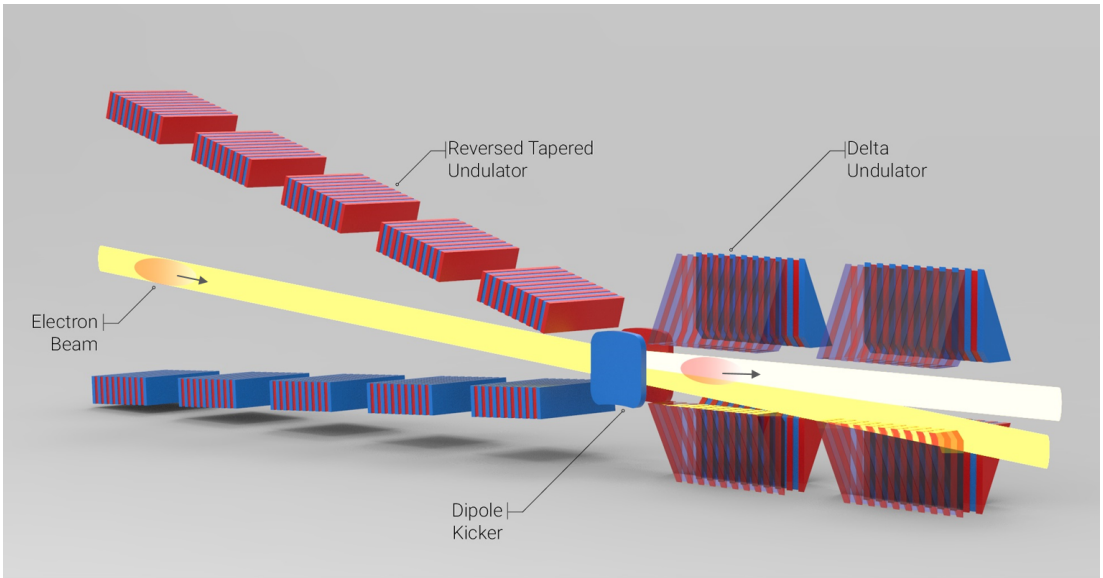

Figure 6.5: Schematic of the method. A relativistic electron beam is initially bunched using a reverse tapered undulator. This suppresses the generation of linearly polarised radiation. A dipole kicker (or off-axis quadrupole lattice) then redirects the electron beam into two Delta undulators tuned so that the electron bunching is at an harmonic of their fundamental resonant wavelength. The Delta undulators can then be adjusted for different polarisations and tuning to generate light with transversely inhomogeneous polarisation - Fully Structured Light

Proposed for the afterburner extension is then two consecutive orthogonally polarised afterburners, individually adjustable in their strength, polarisation, and relative phase. The two radiation pulses emitted from each of the two undulators overlap spatially and temporally. Previous versions of this crossed undulator setup have experimentally demonstrated polarisation control at the fundamental [104, 105]. In the method described here, the electrons emit higher-order transverse modes at the second harmonic in one or both of the afterburners. This results in an FSL beam with an output field described by the superposition of modes, as in equation 6.2. The phase difference, β, between the two modes can also be controlled by using a small magnetic phase-shifter between the two afterburners. This also allows phase-shifts due to the slippage between modules to be compensated, or the polarisation pattern to be mod-

ified or rotated. Such a setup can be constructed from two Delta-type (or Apple-II) afterburner undulators [106,107], provided that they have sufficient adjustment of their K parameters to access harmonics - extending the practicality of these undulators to enable transverse polarisation control.

6.4 Simulations

Puffin simulations of the proposed method used the parameters, given in Table 6.1, which are based on the parameters for the LCLS-II project at SLAC [32]. These parameters are used to highlight the feasibility of implementing the setup at existing FEL facilities. The wavelength simulated is in the soft X-ray region of the frequency spectrum, though this not the limit of wavelengths possible with the scheme. It may be possible to utilise this method to generate beams structured in polarisation in wavelengths as short as hard X-rays, but this is left for future work.

Table 6.1: Parameters based on LCLSII

Parameter	Value	
Bunching Stage		
Electron beam energy [GeV]	4	
Peak current, I_0 [kA]	1	
rms energy spread σ_γ/γ	1.25×10^{-4}	
Normalised emittance [mm-mrad]	0.45	
rms beam size σ_x [μm]	26	
Undulator period λ_u[cm]	3.9	
Resonant wavelength λ_r [nm]	1.25	
Modulation wavelength λ_m[nm]	40.0	
Modulation amplitude γ_m/γ_0	1.2×10^{-3}	
rms undulator parameter $\overline{a}_u$	1.72	
ρ parameter	1.2×10^{-3}	
Afterburner	Delta 1	Delta 2
Number of periods	20	20
Cylindrical vector λ_r [nm]	2.5	2.5
Poincare vector λ_r [nm]	2.5	1.25

Time-independent (steady-state) simulations were used to demonstrate the method. This mode does not model the full temporal duration of the electron beam. However,

as demonstrated in other crossed undulator methods, temporal pulse effects should not significantly affect the results, as the bunching factor on entering the afterburners is orders of magnitude larger than any beam shot-noise, and the relative slippage between electrons and radiation pulses is less than the coherence length [108].

6.4.1 Reverse Tapered Undulator

The electrons are first pre-bunched in a reverse tapered FEL section with $\lambda_b = 1.25$ nm. Figure 6.6 plots the radiation power and bunching for an untapered undulator and an undulator with a reverse taper introduced. From the figure, the growth rate of the bunching is slightly inhibited when the reverse taper is introduced, but with the advantage of a significant decrease in the power of the radiation. The crosses in the figure mark the power when the bunching factor $|b| = 0.45$; this is the bunching achieved before the electrons were extracted for input to the afterburner. Strong bunching can be achieved using a reverse tapered undulator while reducing the FEL output power to 10 MW, two orders of magnitude lower than without the undulator taper.

The process for pre-bunching electrons in a reverse tapered undulator has been described previously [4]. The electron beam bunching process does not differ significantly from the standard FEL process, with the exception of the reduced radiation power. Steering the electron beam to further reduce the contribution from the background power is not modelled [103], and the radiation generated in the FEL section is simply removed in the second part of the simulation.

6.4.2 Afterburner

The pre-bunched beam then enters the afterburner Delta undulators, which can be adjusted for linear or circular polarisation and tuned so that the electron bunching is at either the fundamental or second harmonic. FSL beams with three different polarisation distributions that are generated using this setup are now presented.

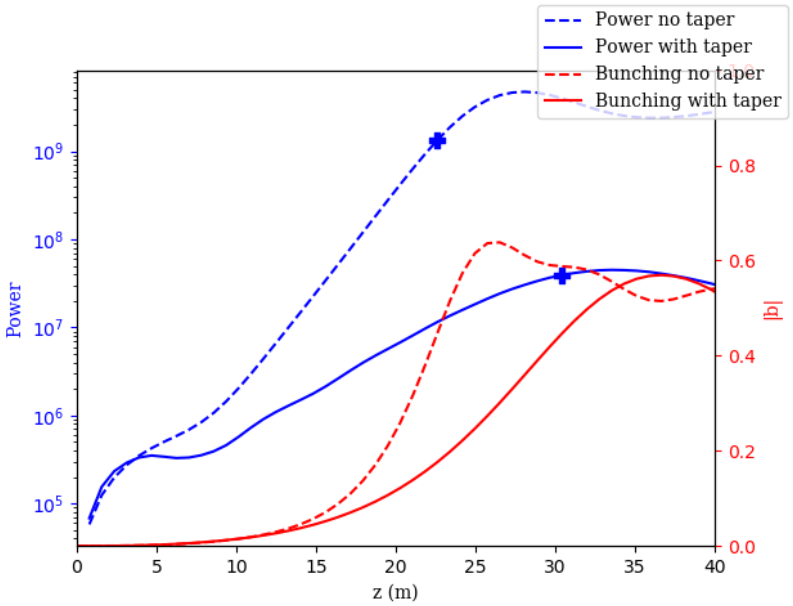

Figure 6.6: Comparison of the the power and bunching of undulator with and without a reverse taper. The blue crosses indicate the power at which the bunching factor $|b| = 0.45$

FEL Generated Vector Beams

In the first example, a pair of cross-polarised planar afterburners is simulated. They are both tuned to a fundamental resonance of $\lambda_r = 2.5$ nm, so that the electron beam is bunched and radiates at the second harmonic. In the far field, the setup generates the field

$$\boldsymbol{E}(\boldsymbol{r}, \boldsymbol{\phi}) = \epsilon_1 HG_{1,0}\hat{\boldsymbol{e}}_{\boldsymbol{x}} + e^{i\beta}\epsilon_2 HG_{0,1}\hat{\boldsymbol{e}}_{\boldsymbol{y}}. \tag{6.10}$$

With $\epsilon_1 = \epsilon_2$, this superposition is seen in Figure. 6.7 to create an annular intensity profile with a radial polarisation distribution for $\beta = 0$.

The normalised Stokes vector capturing the spatial polarisation for these crossed planar harmonic undulators can be written as

$$\boldsymbol{s} = \begin{pmatrix} \cos(2\phi) \\ \cos(\beta)\sin(2\phi) \\ \sin(\beta)\sin(2\phi) \end{pmatrix}. \tag{6.11}$$

Note that for $\beta \neq 0$, the polarisation distribution can also contain circular components.

Similarly, with crossed helical undulators tuned so that the bunching is at the second harmonic, one obtains $\ell_R = -1$ and $\ell_L = 1$. If the undulators are the same length and the bunching factor does not change significantly between them, the modes have equal amplitude, $\epsilon_L = \epsilon_R$. The Stokes vector obtained is then

$$\boldsymbol{s} = \begin{pmatrix} \cos(\beta - 2\phi) \\ \sin(\beta - 2\phi) \\ 0 \end{pmatrix}. \tag{6.12}$$

The S_3 parameter vanishes, so the beam has only linear polarisation states which vary with ϕ. The generated vector 'vortex beam' is also shown in Figure 6.7.

In order for this description to accurately model the final FSL output, the radiation emitted in each undulator should be well-described by a pure mode. In Ref. [109], it was shown that with sufficiently large K and periods N_u in a helical afterburner, coherent radiation from a pre-bunched electron beam is well approximated by an LG mode in the limit that the electron beam radius satisfies $\sigma_x > \gamma_z\sqrt{N_u}/k$, such that the emission angles are dominated by the electron beam and not the undulator emission. The undulators must also be kept relatively short to reduce the diffraction of the radiation so that the transverse sizes of the modes do not significantly differ.

FEL Generated Full Poincaré Beams

The second class of light with spatially inhomogeneous polarisation considered is full Poincaré beams created from a superposition of $LG_{0,\pm1}$ and $LG_{0,0}$ (Gaussian) radiation with orthogonal circular polarisations. From equation (6.2.2), the Stokes vector then becomes

$$\boldsymbol{s} = \begin{pmatrix} \frac{2\sqrt{2}rw_0}{2r^2+w_0^2}\cos(\beta - \phi) \\ \frac{2\sqrt{2}rw_0}{2r^2+w_0^2}\sin(\beta - \phi) \\ \pm\frac{2r^2-w_0^2}{2r^2+w_0^2} \end{pmatrix}, \tag{6.13}$$

where the $+$ and $-$ signs correspond to $(\ell_L, \ell_R) = (1, 0)$ and $(\ell_L, \ell_R) = (0, -1)$, respectively. On-axis, $r = 0$, the polarisation is purely circular while the at the radius

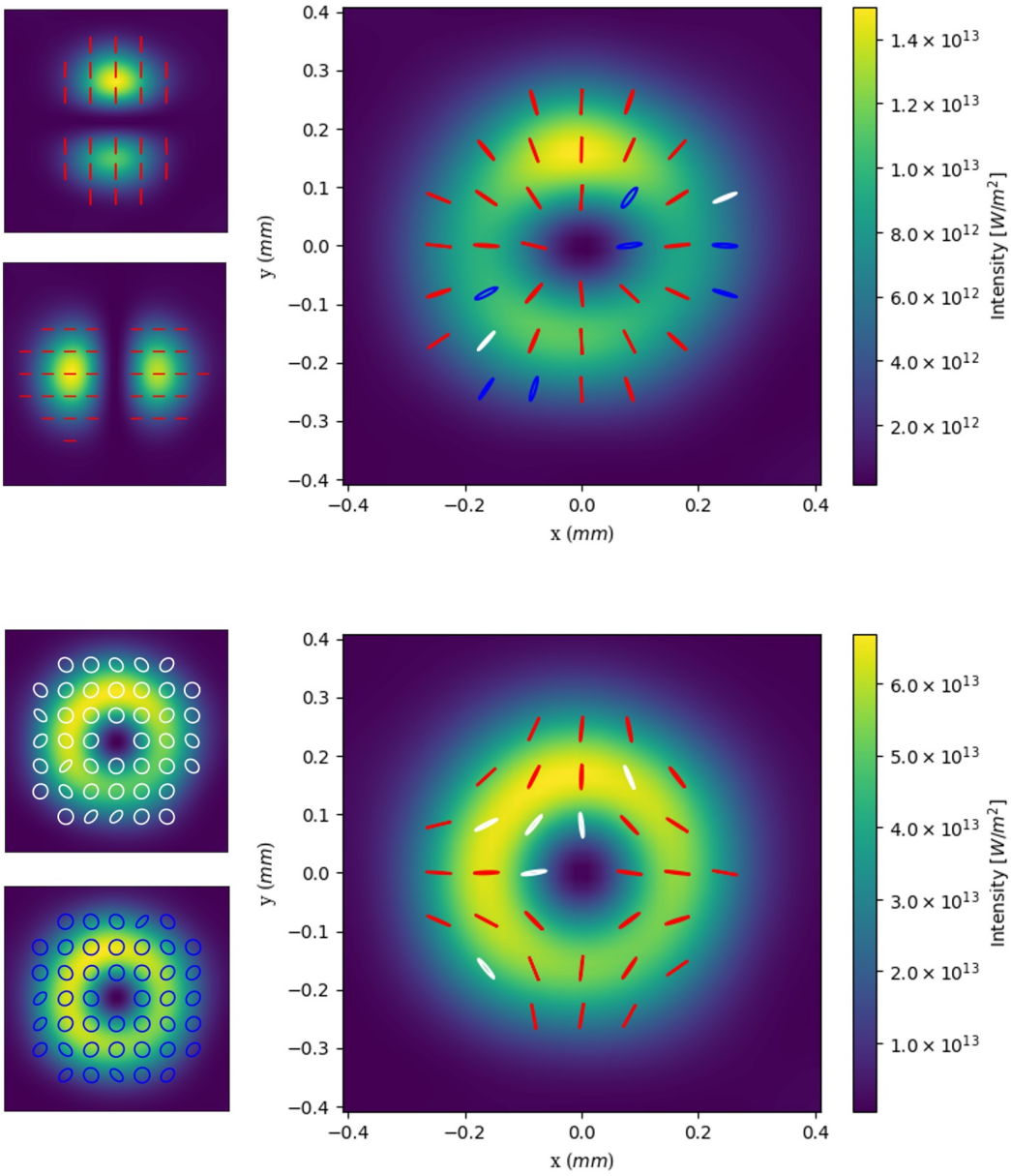

Figure 6.7: Simulation of cylindrical vector polarisation. The electrons are bunched at the second harmonic of the Delta undulators to give orthogonal linear (top) and circular (bottom) polarisation. The radiation polarisation emitted from each Delta undulator is plotted schematically on the (left) two plots and the combined field simulated from both undulators on the (right) plot. Red, blue and white lines correspond to linear, right-circular and left-circular polarisation respectively.

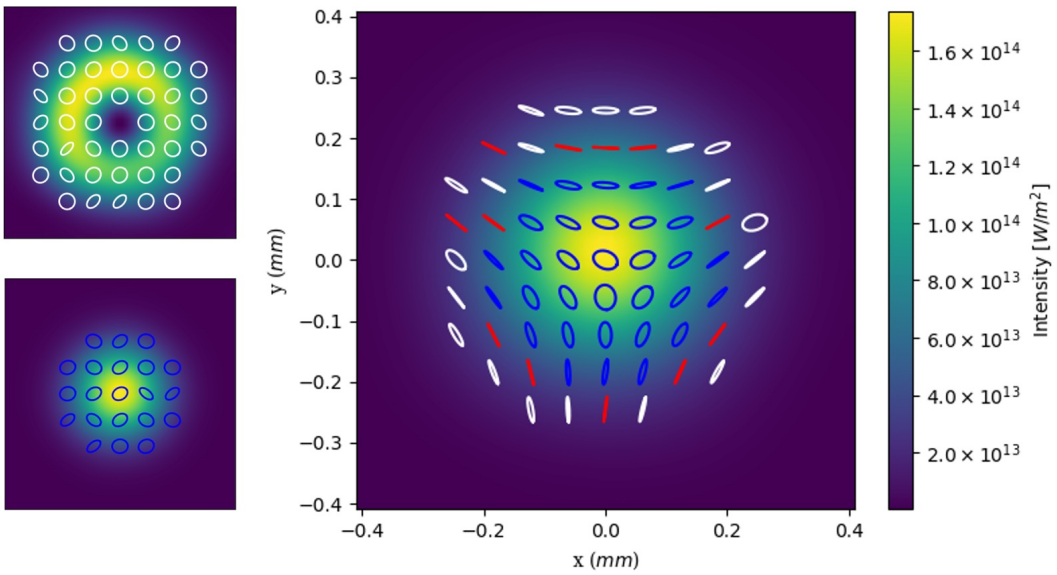

Figure 6.8: Poincaré polarisation distribution downstream of the afterburner. The Delta undulators are set to have orthogonal circular polarisations. The electrons are bunched at the second harmonic of the first undulator and the fundamental of the second undulator. The radiation emitted in each Delta undulator is plotted (left) along with the combined field from both undulators (right).

$r = w_0/\sqrt{2}$, the polarisation is purely linear, with orientation depending on ϕ. Figure 6.8 shows the 'star' Poincaré beam output generated in the $(\ell_L, \ell_R) = (1, 0)$ case. To achieve this combination, the second undulator is tuned so that its fundamental resonance matches the bunching wavelength at $\lambda_r = 1.25$ nm and the radiation emitted is Gaussian. The first undulator is tuned to $\lambda_r = 2.5$ nm, radiating at the second harmonic as before. The electrons radiate with higher power at the fundamental than at the second harmonic. To compensate and balance the powers between the two radiation beams, the Delta undulator emitting at the fundamental is detuned from resonance to reduce its power output. Detuning the undulator will affect the mode size and therefore polarisation structure. Specific undulator detuning is a topic for future studies and will depend on the specific application.

Unavailable polarisation distributions

Due to the relationship between the polarisation and the transverse modes, only certain distributions are available with this setup. Table 4.1 summarised the possible transverse and polarisation combinations. This means that the spiral, azimuthal and 'lemon' polarisation distributions are not enabled through the setup. Delaying the y-polarised field E_y with optics would allow transformation of the beams presented into these distributions. However, since this requires optics, this is not included.

6.5 Future Possibilities of FEL Generated FSL

The three x-ray polarisation topologies demonstrated here are not the full range of pulses available with the two Delta undulator arrangement. In addition to varying the polarisation and undulator resonance, other factors can change the polarisation distribution. Both the phase and power ratio between the different transverse modes can be adjusted which, for example, could be used to create elliptical vector beams. Slightly detuning the resonance of one undulator will push the radiation further off-axis, which can be used to control the mode overlap [104]. Finally, radiating at even higher harmonics of a helical undulator will generate the higher-order LG modes producing yet more variants, though the power drops with increasing harmonic number [109].

This method can generate Poincaré beams at any operational wavelength of a FEL facility. The advantage of the afterburner configuration is that it is both simple and cost effective to implement as the afterburners can be added to existing FEL facilities, or may already exist as the last couple undulator sections. Furthermore, the method could be combined with other methods. For example, consideration of temporal or short pulse effects can be envisaged that alter the FSL in the temporal domain (e.g., [110]) adding a further dimension for potential experimental exploitation.

Chapter 7

Alternating Pulse Properties

This chapter describes a method developed which will create a train of radiation pulses where the properties of the pulses alternate. As discussed in Section 3.3, typical OAM generation methods use static devices which transform the phase of the radiation. In addition to limiting the wavelength and intensity of radiation with OAM, this means it is difficult to alternate the OAM of a radiation pulse at ultra-fast timescales using conversion optics. This problem also arises for modulation of the polarisation of radiation as conventional polarising elements are quasi-static devices at ultra-fast timescales. On route to developing a method for modulating the OAM of radiation, a simple method for modulating the polarisation was found. This work uses a technique for generating trains of pulses in a FEL called mode-locking. A description of mode-locking in a FEL is provided before presenting the scheme for alternating the pulses' polarisation. A discussion on how this can then be adapted to modulate the handedness of OAM carried by each pulse is included at the end of this chapter along with promising first results.

7.1 Mode-locking

7.1.1 Description of Mode-Locking in a FEL

Trains of short pulses can be created in a FEL through a process called mode-locking, analogous with mode-locking in a conventional cavity laser [49]. The mode-locked FEL concept was first proposed by Brian McNeil and Neil Thompson in their initial paper

on the mode-locked FEL amplifier [5]. In collaboration with Dave Dunning, the authors subsequently adapted the work into an afterburner configuration [111]. Mode-locking in FELs has not been demonstrated experimentally, although plans to test the method at FEL facilities should be implemented in the near future.

Mode-locking is a method to obtain trains of ultra-short radiation pulses by synthesising a set of axial radiation modes which can be 'locked' by the introduction of an additional modulation. In a FEL, frequency modes can be generated, without a cavity, by separating short undulator modules with chicanes which add extra slippage between the electrons and the radiation field by delaying the electrons. Analysis in [5] showed this additional slippage affects the frequency spectrum of the radiation. The spontaneous emission for a series of undulator and chicane modules has a spectrum described by a sinc^2 function envelope multiplied by an interference term. The width of the sinc^2 function defines the bandwidth, which is equal to that of an individual undulator module ($\Delta\omega_{FWHM} \simeq 1/N_w$). Interference of radiation radiated in multiple undulator sections means that only wavelengths of radiation that slip ahead of electrons by an integer number of wavelengths between undulator modules survive. The sinc^2 function is then modulated by a comb of discrete frequency modes centred on the resonant frequency, ω_r. For a combined slippage, $s = \delta + l$, from the slippage in one undulator module, l, plus the slippage in the subsequent chicane, δ, the frequency mode spacing is

$$\Delta\omega_s = \frac{2\pi c}{s}, \tag{7.1}$$

equivalently,

$$\Delta\omega_s = \frac{2\pi}{T_s}, \tag{7.2}$$

where $T_s = s/c$ is the time taken for radiation to travel the slippage length.

The slippage enhancement factor, S_e, is defined as the ratio of the total slippage between undulator modules and the slippage in one undulator module,

$$S_e = \frac{s}{l}. \tag{7.3}$$

It is found that the number of modes, N_0, which fit into the frequency bandwidth is

$$N_0 = 2S_e - 1. \tag{7.4}$$

From the equations above, to increase the number of frequency modes there are two options. Either increase the bandwidth by decreasing l while keeping s constant or - for a fixed undulator length - decrease the mode spacing by increasing δ. For $S_e = 1$, the spectrum is the normal undulator spectrum for the total undulator length and not an individual undulator module.

The synthesised frequency comb transforms into a temporal train of radiation intensity spikes. However, the frequency modes have no fixed phase and therefore the pulse separation and duration are irregular. In order to fix the phase relationship between the different frequency modes, an interaction modulation is introduced with the modulation frequency, $\Delta\omega_m$, equal to the mode spacing frequency ($\Delta\omega_m = \Delta\omega_s$). The required modulation can be applied to the electron beam as either a current [112] or energy [5] modulation. The result of phase-locking the frequency modes is that they will constructively interfere at defined times given by

$$t = nT_s, \tag{7.5}$$

where n is an integer. In addition to even spacing of pulses in the temporal pulse train, the pulses also have equal duration. The full width at the base of each pulse is $2T_s/N$. The FWHM pulse duration, τ_p, is then approximately

$$\tau_p \approx T_s/N_0. \tag{7.6}$$

7.1.2 The Mode-locked Afterburner

Mode-locking in a FEL was first devised as a mode-locked amplifier setup where the additional slippage is applied between all sections of undulator. Implementation of this scheme would involve large changes to existing facilities in order to insert many chicanes between short undulator modules. The mode-locked afterburner was proposed

as a solution to generating the same short pulse radiation trains as the mode-locked amplifier but using a method that can be easily implemented at existing accelerator facilities.

The mode-locked afterburner can be split into three sections, the first is a modulator that imposes a sinusoidal energy modulation on the electron beam. Second, an amplifier section that bunches the electrons; this section makes use of the standard undulator lines available at user facilities. A micro-bunching comb develops in the amplifier due to the energy modulation on the electron beam. Close to saturation, the electrons enter the final section - the afterburner. Here, short undulator modules separated by chicane delays map the micro-bunching comb onto the temporal structure of the radiation. Each of these three sections is now discussed.

Modulation

A sinusoidal modulation is imposed on an electron beam through interaction in a undulator with a resonant laser field. This modulation takes the form

$$\gamma(t) = \gamma_0 + \gamma_m \cos(\omega_m t), \tag{7.7}$$

where γ_0 is the mean energy, γ_m is the modulation amplitude and ω_m the modulation frequency. The modulation period, $\lambda_m = \omega_m/2\pi c$, is set to be an integer number of the FELs resonant wavelength. Since it is much longer than the FEL radiation, HHG sources [113] could be used as the modulating seed laser for mode-locking at soft and hard x-ray wavelengths.

Amplifier Stage

The modulated electron beam enters a long undulator where the FEL interaction bunches the electrons together. The energy modulation on the electron beam means that there are large energy gradients in the electron beam. If the gradient, $\Delta\gamma$, is large enough, the FEL interaction is suppressed and the electrons won't micro-bunch. Near the extrema of the energy modulation, the energy gradient is much smaller and micro-

bunching is expected. In fact, micro-bunching develops significantly more strongly at the minima of the modulation than the maxima as discussed in [111, 114]. Only sections of the electron beam close to the minima of the modulation micro-bunch together creating a periodic bunching structure in the electron beam. Increasing the amplitude of the energy modulation decreases the length of the bunched sections. Matching this length to the length of the slippage from the individual modules in the afterburner minimises the duration of the radiation pulses without significantly suppressing the growth rate.

The Afterburner

With the micro-bunching comb established, the electron beam enters the 'afterburner' which produces the radiation pulse train. Although here and in the remainder of this chapter this section is referred to as an 'afterburner' (following the language used in Ref. [111]), it is noted that this section is longer than undulator sections commonly deemed afterburners such as the one used in Chapter 6. Although the afterburner section used to mode-lock the radiation is shorter than the preceding amplifier section, the majority of the FEL amplification takes place in the afterburner and therefore is not a true afterburner.

In the mode-locked afterburner, chicanes - placed between undulator modules - maintain the overlap between sections of high micro-bunching and the developing radiation train and the radiation spikes are therefore amplified. The radiation pulse train generated in the afterburner dominates the final radiation structure; this is because the radiation growth is suppressed in the amplifying section - due to the energy modulation - and exponential in the afterburner as the rephasing of the electron beam by chicanes maintains the interaction between sections of high beam quality. Additionally, the chicanes have a dispersive effect on the electrons which increases the electron beam's micro-bunching. This is the 'optical klystron' effect [115].

7.2 Polarisation Modulation

7.2.1 Motivation

Current experiments can demand greater spatial [83] and/or temporal [116] control and flexibility of the polarisation than the generation of purely circular, elliptical or linearly polarised light. In particular, fast temporal switching of light's polarisation is desirable for techniques such as polarisation modulation spectroscopy, notably, X-ray magnetic circular dichroism (XMCD) [117–119] and may offer control over material excitations including lattice vibrations [120], charge and spin [121, 122].

Ultra-fast switching of the polarisation properties of light is a non-trivial task as conventional polarising elements are quasi-static devices at ultra-fast timescales. While some conventional polarising elements can be controlled by electric currents [123], these are limited by their electronic components to gigahertz switching speeds and also see large energy losses.

In the drive to further decrease switching rates, recent research using plasmonic technologies has further decreased linear polarisation switching to 800fs [124] and circular polarisation switching to pico-second timescales [125]. However, these techniques are based on the active control of polarising elements and operate primarily at visible wavelengths or longer. As wavelengths shorten beyond the ultraviolet, polarising optics are more limited with modulation timescales being determined primarily by the light generation method.

In electron accelerator based light sources, which can generate light into the hard X-ray, it is the motion of the radiating electrons propagating through magnetic undulators that determines the polarisation of the photon beam. For example, circular polarisation modulation with a $\sim$ 2ns switching rate has been demonstrated in a synchrotron by controlling electron bunch orbits through twin undulators [126]. Methods of generating X-rays with temporally varying polarisation from the output of FELs include 100fs switching using a chirped electron beam [127]. Femto-second isolated pulses with different polarisation can be generated with the fresh slice method described in [128].

It can be envisaged that significant improvement on temporal polarisation switching

timescales to those comparable to atomic processes will enable experimental investigation of these processes. In XMCD, for example, the polarisation switching rate of X-rays limits the observable processes to those occurring slower than the switching cycle [119]. In this thesis, a method is described which could improve the polarisation switching rate of both linear and circularly polarised high brightness X-rays towards the attosecond timescale regime and comparable to the period of a ground state electron in the Bohr hydrogen atom, the atomic unit of time $\approx$ 24as. We speculate that pulses of such timescales could be used to develop novel methods, perhaps similar to XMCD, that can improve temporal resolutions to below that of the exchange interaction responsible for magnetic order [129].

7.3 Method for Generating Pulse Trains with Alternating Polarisation

Section 7.1 details a FEL technique that produces a train of radiation spikes. In the following section, a method to produce a pulse train where the polarisation of each pulse alternates is presented. Figure 7.1 shows a schematic overview of the technique. The initial two stages of the setup - the modulator and amplifier - are the same as for the mode-locked amplifier and are used to generate a micro-bunching comb. The electron bunching structure is then mapped to an alternating polarised pulse train by alternating orthogonal polarised undulators - the afterburner section. Both of the different polarised radiation fields emitted in the afterburner are mode-locked and therefore are emitted in pulse trains. The two pulse trains are shifted temporally with respect to each other so that the combined pulse train consists of alternating polarised pulses. The polarisation of the pulses generated depend on the undulator modules which make up the afterburner. They can be either planar or helical undulators to generate, respectively, linear or circular polarisation. However, the polarisation emitted in the different undulators must be orthogonal to each other.

Figure 7.2 shows a schematic of just the afterburner section which the electrons enter close to saturation after a micro-bunching comb structure is developed in the electron

Figure 7.1: Schematic layout to generate pulse trains with alternating pulse properties. The method uses three sections: an electron energy modulator, long FEL amplifier and an afterburner section consisting of short undulator sections which alternate in polarisation separated by electron chicane delays.

beam. The chicanes placed between undulator modules delay the high micro-bunched regions of the electron beam to ensure they overlap with the developing pulse train in the undulator radiating corresponding polarised light - amplifying the short pulses of radiation. Radiation will not interact with electrons in an orthogonally polarised undulator and experience free propagation. The undulators then effectively act like additional chicane modules to the orthogonally polarised radiation.

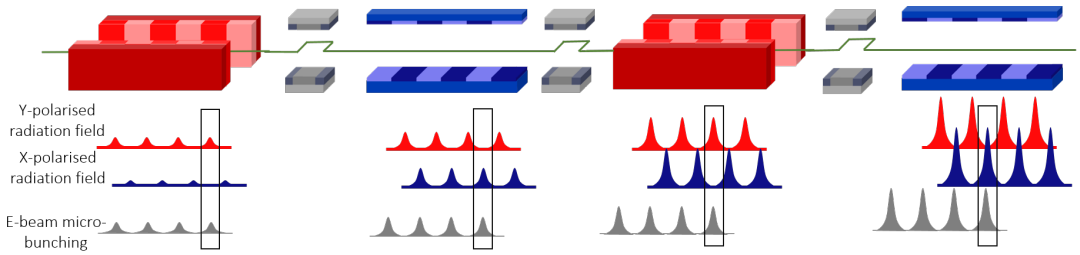

Figure 7.2: Schematic layout of a section of afterburner used to generate a radiation pulse train with alternating x and y linear polarisation. In each undulator, those regions of the electron beam with modulated micro-bunching emit coherently. Chicanes delay the electron beam between undulator modules so that those sections of high micro-bunching overlap with the appropriately polarised pulse for the undulator in which they are propagating.

The combined slippage with respect to the radiation wavefront from the chicanes plus undulators emitting the same polarisation is the modulation period λ_m. This maintains the overlap between the radiation pulse structure and electron beam which mode-locks the radiation. The temporal separation of pulses of radiation with the same

polarisation is then $T_s = \lambda_m/c$ and the relative times of the pulses are

$$t_1 = nT_s. \tag{7.8}$$

The orthogonally polarised pulses will then have pulse peaks at relative times

$$t_2 = t_0 + t_1 + \Delta T, \tag{7.9}$$

where $\Delta T = \lambda_m/2c$ is the time for the radiation to travel half the modulation period through the bunch. t_0 is a constant which may shift the radiation pulse trains relative to each other. This relative shift is controlled by adjusting the slippage between consecutive orthogonally polarised undulators to be

$$s_{12} = \lambda_m/2 + ct_0 \tag{7.10}$$

and

$$s_{21} = \lambda_m/2 - ct_0. \tag{7.11}$$

When $t_0 = 0$, there is equal slippage between undulator modules and therefore equal spacing between all pulses.

7.4 Simulations

Simulations of alternating pulse generation were carried out in Puffin with the same LCLS-II type parameters listed in Table. 6.1. The method was modelled, first, with the plane wave approximation (1D simulations) to save computation time, then repeated for full 3D simulations.

7.4.1 Modulator

An electron beam, with a Gaussian current profile, is first prepared with a sinusoidal energy modulation of period $\lambda_m = 40$ nm $= 32\lambda_r$. This is applied via the initial conditions of the beam before any FEL interaction is simulated. Start to end simulations with full

modelling of the energy modulation is left for future work. However, pre-modulation at longer wavelengths is relatively straightforward and similar modulation as presented here for a non-ideal electron beam has previously been demonstrated [130, 131].

7.4.2 Amplifier

As with the mode-locked afterburner of [111], the electron micro-bunching comb is then developed in a SASE FEL 'pre-amplifier'. The simulation modelled an x-polarised undulator similar to that found at most current FEL facilities. The power growth in this pre-amplifier stage is inhibited by the electron beam energy modulation. On subsequent injection into the afterburner, the power growth in the pulsed regions becomes exponential due to their overlap with the high quality electron beam regions being maintained. There is therefore much greater radiation power generated in the afterburner than in the pre-amplifier. The point at which the electron beam is extracted from the pre-amplifier is chosen so that the radiation is two orders of magnitude smaller than the final saturated radiation power in the following afterburner. For 1D simulations, the electrons are extracted after 550 undulator periods and the electrons are extracted after 900 undulator periods for the full 3D simulations.

7.4.3 Alternate Linear Polarisation Afterburner

The method is demonstrated, first, using an afterburner with alternating x and y planar undulators that will emit correspondingly linearly polarised light. Both the x and orthogonal y polarised undulator modules in the afterburner are 8 periods long, each separated by a chicane that delays the electrons by a further 8 resonant wavelengths. The total electron delay is then, $s = 16\lambda_r = \lambda_m/2$ between successive undulator modules and λ_m between undulators of the same polarisation. This maintains overlap between the electron micro-bunching comb and the alternating orthogonally polarised radiation.

1D results

1D simulations are used to track the overlap between the electron beam bunching and the different radiation fields. Figure. 7.3 plots a window of radiation and electron beam at different positions in the afterburner. The top panel shows the electrons and field before the electron beam enters the afterburner. Electrons at the minima of the modulation have micro-bunched in the amplifier stage and there is a small amount of x-polarised radiation from the amplifier. The remaining panels are plots from different positions through the amplifier. The second and third panels are, respectively, plots from the middle y and x polarised undulators and the last two plots are the last two undulator modules. In the different undulator modules, the micro-bunched comb overlaps with the corresponding radiation spike. The micro-bunching increases rapidly and the radiation spikes are amplified.

3D results

The results from the 3D simulations are now presented. Figure. 7.4 shows a section of the radiation power profiles and the spectrum of the x and y polarised fields after 36 afterburner undulator modules (16 of each polarisation). The additional slippage between undulator modules leads to a frequency spectrum that is broader than typical FEL output and discretized into frequency modes with mode spacing, $\Delta\omega_s$, determined by the time taken for the radiation to travel the total slippage length between the same polarised undulators. The radiation pulse peaks arise from the constructive interference between the frequency modes whose phase has been fixed by the modulation, $\Delta\omega_m = \Delta\omega_s$. This is the principle of mode-locking as described in [5, 49].

As the undulator modules have equal lengths, both the x and y polarised fields have approximately the same pulse FWHM duration of $\tau_p \approx 19$ as and with peak powers of $P_{pk} \approx 1$ GW. The separation between each pulse is approximately 67 as corresponding to a polarisation switching rate of 15 PHz. The radiation spikes with different polarisation do not interfere with each other due to their orthogonal polarisation. Each pulse train has power fluctuations typical of SASE output. However, as both fields are emitted by the same electron beam source, which sees only small changes between

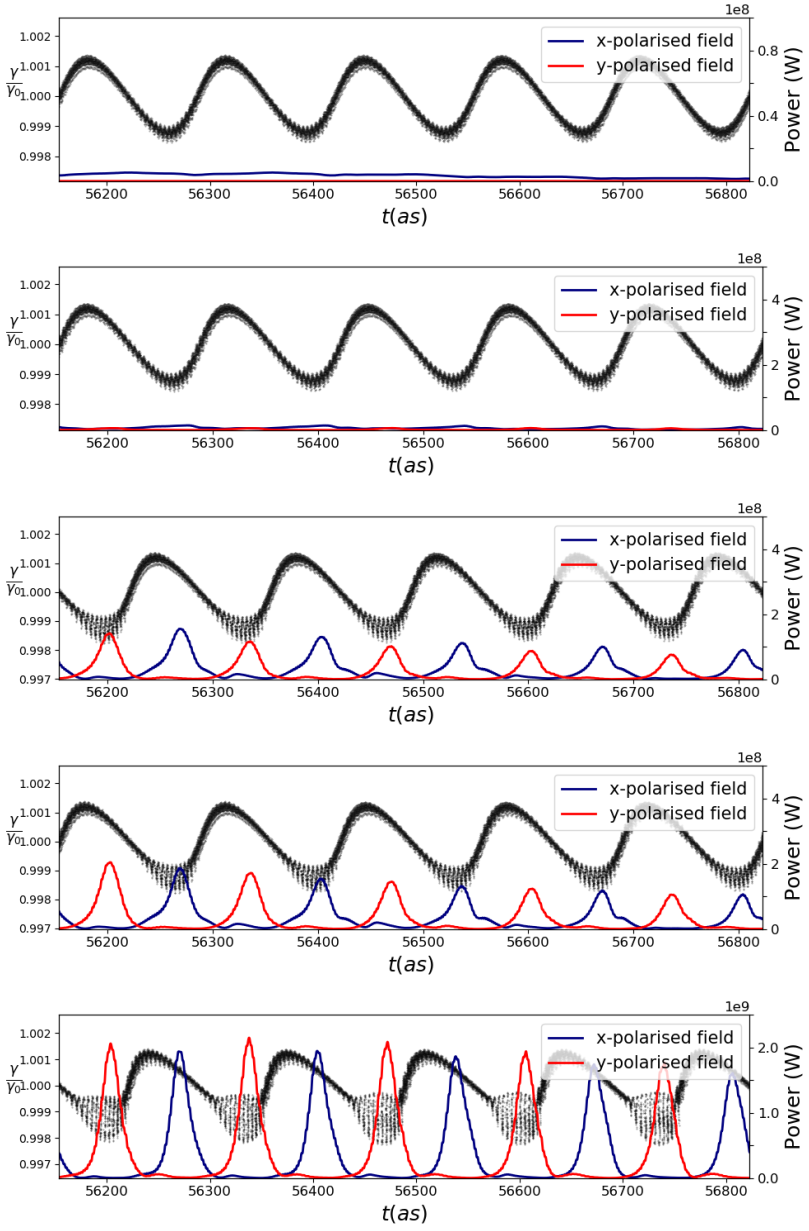

Figure 7.3: Plot of electron energy and radiation power vs time for a window of radiation. Starting at the electrons' entry into the undulator, panels from top to bottom follow the evolution of the electron beam propagating through the afterburner. The minima of the electron beam's energy modulation maintains overlap with the radiation spikes of the polarised field corresponding to the undulator they are in.

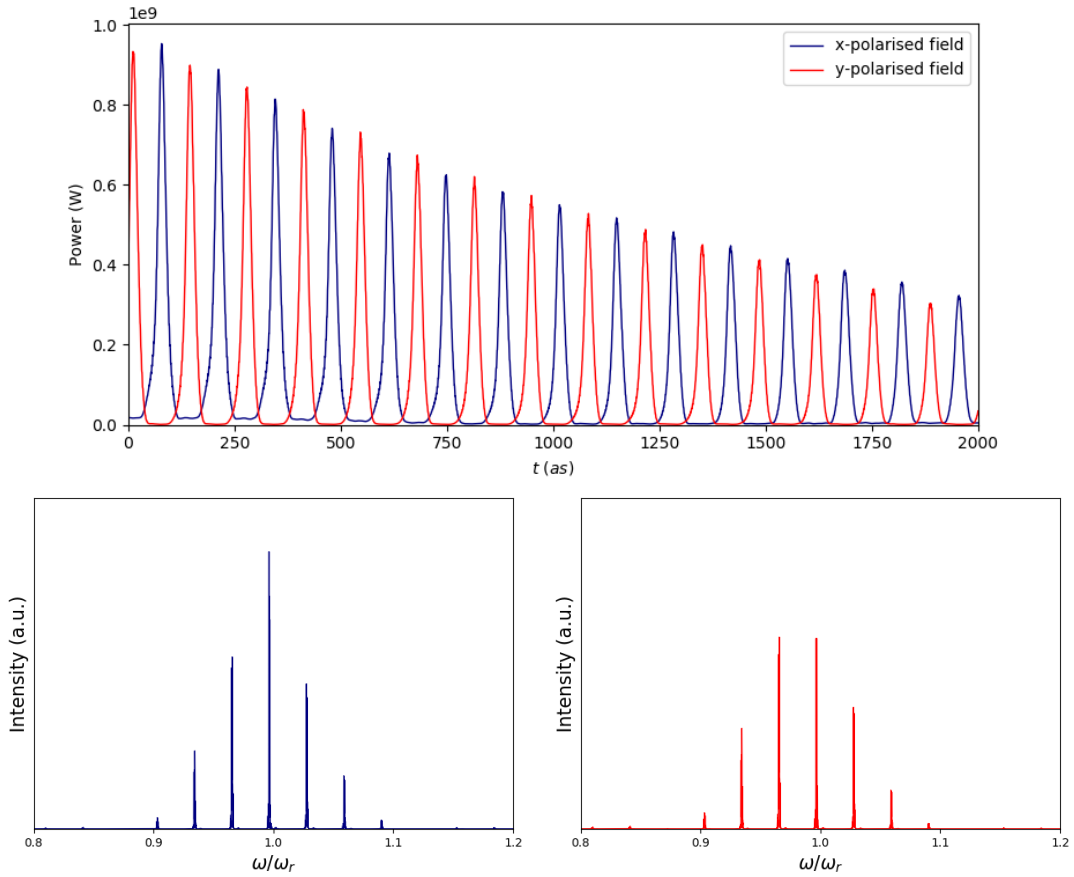

Figure 7.4: Power vs relative time t for the x and y polarised fields (top) and the corresponding spectra (bottom) after 36 undulator-chicane modules.

undulator modules, fluctuations in the power of one pulse train envelope should be similar to its orthogonal counterpart.

A normalised Stokes parameter, s_1 - defined by equations (6.4) and (6.5) - is used to examine the degree of linear polarisation in the pulses. Values of $s_1 = \pm 1.0$ then indicate fully linear x or y polarisation, respectively. This Stokes parameter is plotted as a function of time in Figure 7.5. From the figure, it is shown that the polarisation is highly modulated, flipping between the two polarisation states. The high degree of polarisation contrast is seen at the peak powers, $|s_1| \approx 1.0$. Across the full pulse train, $|s_1| > 0.95$ at the peak powers, demonstrating a high degree of polarisation modulation.

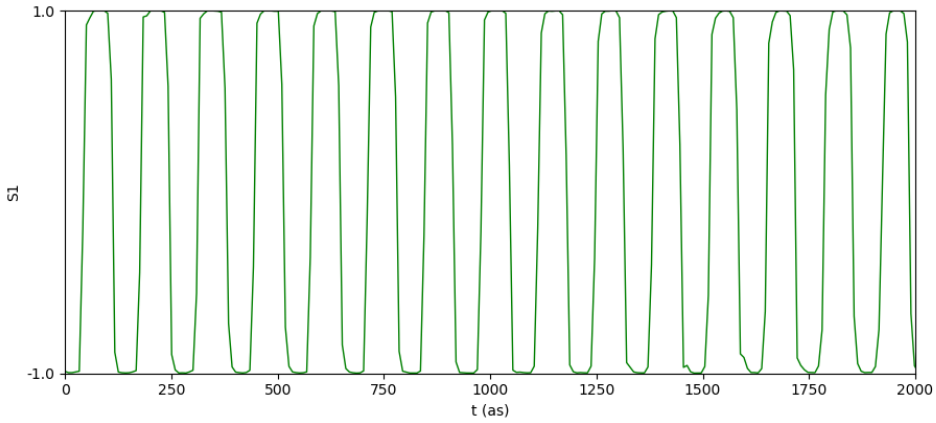

Figure 7.5: The on-axis normalised Stokes parameter s_1 as a function of relative time t after 36 undulator-chicane modules. It is seen that s_1 flips between positive and negative values with extremes at $|s_1| \approx 1.0$, indicating high degree of polarisation modulation.

7.4.4 Alternate Circular Polarisation Afterburner

Pulses with polarisation alternating between left and right hand circular polarisation have also been modelled. The amplifier section, which pre-bunches the electrons using SASE, remains an (x-polarised) planar undulator similar to that above. The afterburner now consists of orthogonal left and right circularly polarised helical undulators.

Figure 7.6 shows the power profiles for the left-hand circular, LCP, and right-hand circular, RCP, polarisation. The pulses now alternate between orthogonal circular polarisation with the same FWHM pulse duration τ_p and rate as the linearly polarised case above. The Stokes parameter, s_3, which gives the degree of circular polarisation is plotted in Figure 7.7. The additional noise seen in this figure, compared to the linear polarised case (Figure 7.5), is a numerical artifact of analysing the circular polarisation content of the field from the Puffin code which natively splits the field in linear polarisation. Across the pulse peaks, there is a high degree of circular polarisation, $|s_3| > 0.9$. This is very promising as many ultra-fast polarisation switching techniques cannot achieve full handedness reversal.

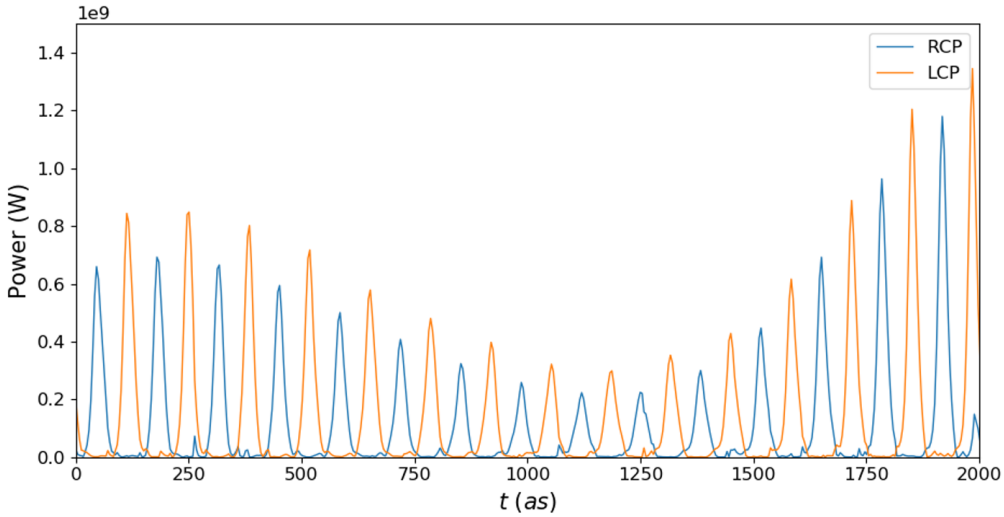

Figure 7.6: Power Spectrum for left and right hand polarisation vs relative time at the end an afterburner with alternating polarised helical undulator modules.

7.5 Future Adaptations

The simulation parameters used considered soft X-ray pulses similar to the LCLS-II, however, this is by no means the limit of the wavelengths available with this setup. Extrapolating from the simulations of a hard X-ray mode-locked afterburner as presented in [111], the same parameters adapted to generate alternating polarised pulses here would generate pulse separation times of 5 as, approximately one fifth of the atomic unit of time. Discussion of scaling the mode-locked afterburner to yet higher photon energies provided in [111] should also apply to the methods described here. Given the broad scaling of FEL wavelength operation, the method described will also be applicable to longer wavelengths, again opening up new experimental opportunities.

As well as operating across a broad range of wavelengths, the method could be adapted to meet other specific experimental requirements. The temporal shift between pulse trains of orthogonal polarisations may be controlled via the chicane slippage as defined in equations (7.10)-(7.11). This could be used to bring alternating pulses close together followed by a longer time interval. The time duration of the different pulse types may also be altered by the length of the different types of undulators to generate pulse trains with a pulse of one polarisation followed by a shorter pulse with

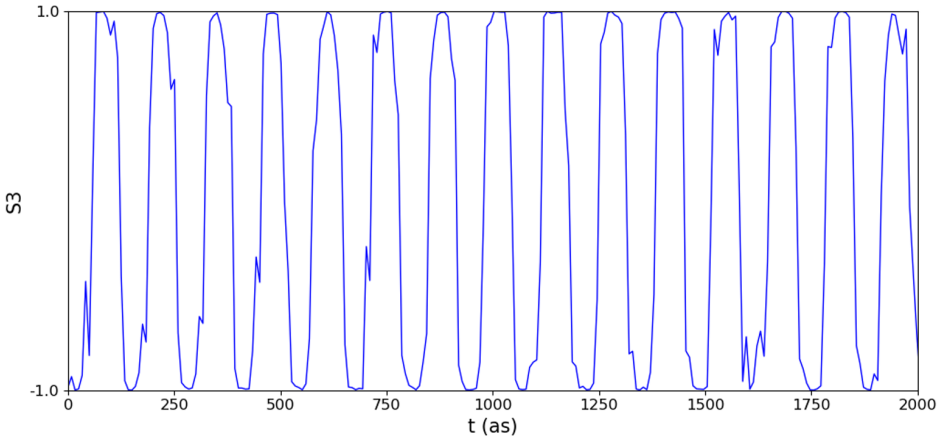

Figure 7.7: The on-axis normalised Stokes parameter s_3 as a function of relative time t after 36 undulator-chicane modules. It is seen that s_3 flips between positive and negative values with extremes at $|s_3| \approx 1.0$, indicating high degree of polarisation modulation.

the orthogonal polarisation. However, it is noted that this will also result in different pulse powers and bandwidths which would need further consideration.

7.6 Alternating OAM Pulse Trains

Future work will look at adapting the method presented in this chapter to produce pulse trains where the handedness of the OAM in the pulse alternates. The method for alternating the properties of pulses in a pulse train originated from the desire to alternate the OAM by utilising OAM emission at the second harmonic. Alternating the polarisation was studied first for two reasons. First, the simulations of the polarisation modulation method could utilise the 1D mode in Puffin whereas simulations of OAM pulses cannot. The second reason, alternating the polarisation requires a setup which is closer to the original mode-locked afterburner than for alternating the OAM.

To adapt the method to modulate the handedness of OAM, the helical afterburner undulators should be tuned so that the frequency of the electron beam bunching is at the second harmonic of the undulators. The bunching established in the amplifier section must be greater than for polarisation modulation as no additional FEL interaction occurs in the afterburner.

An important consideration to adapt the setup for OAM modulation is the frequency spectrum of the OAM radiation. Mode-locking the radiation increases the bandwidth to that of an individual undulator module. Equation (4.6) gave the width of the frequency spectrum for the different harmonics. For a fixed bunching frequency, the width of the spectrum decreases with increasing harmonic number, h. In each afterburner tuned to a sub-harmonic of the electron bunching, the electrons now slip behind the radiation field two wavelengths per undulator period which means that the slippage enhancement factor, equation (7.3), and therefore the number of frequency modes established, equation (7.4), is less than for the undulators tuned to radiate at the fundamental wavelength with the same number of periods. This would suggest that the undulator modules should be kept short in order to increase the width of the spectrum and therefore the number of nodes. However, shorter undulators have greater coupling to the fundamental azimuthal mode and pure OAM modes are only generated for sufficiently large N_u - for further details see reference [67]. A solution is to increase the energy modulation period and therefore decrease the frequency mode spacing. This restricts the minimum pulse duration and switching rate of alternating OAM pulses.

Future work will fully develop the method to produce pulse trains. However, included now is the result of an initial simulation where an electron beam with a micro-bunching comb structure is sent through alternating handedness helical undulators. The electron beam was first prepared with a sinusoidal modulation of period $\lambda_m = 90$ nm $= 72\lambda_r$ and sent through a long amplifier section which established a maximum bunching factor $|b| \approx 0.6$ at the minima of the modulation. The radiation emitted in the amplifier was removed and the electron beam, now with a comb of micro-bunching, was sent through a short afterburner consisting of 6 helical undulators (3 of each handedness) each 18 periods long.

Figure 7.8 shows the power of the radiation, decomposed into a set of Laguerre-Gaussian modes. The pulses are each 150as in duration. This shows the handedness of OAM can be modulated through an adaption of the method used to flip the handedness of circular polarisation.

Future studies will look at refining this method and consider the minimum pulse

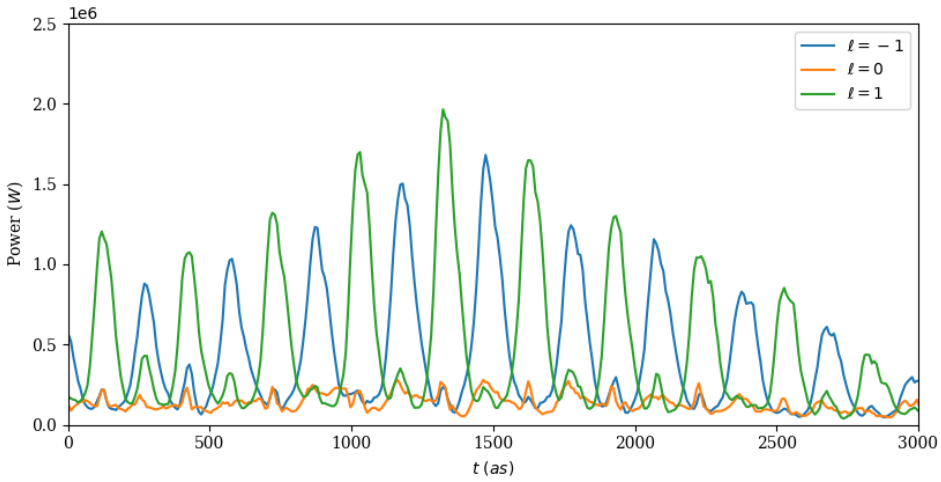

Figure 7.8: Power vs relative time t discomposed into azimuthal modes.

duration and maximum switching rate enabled in the scheme. It is also important that the radiation emitted in the amplifier section is removed from the final radiation pulse train. It may be possible to use reverse tapering and electron steering as was discussed in Chapter 6. However, this has not been demonstrated for an electron beam with an energy modulation and so requires further examination.

Chapter 8

Conclusion

This thesis presented three different schemes to diversify FEL output with a focus on the generation of higher-order transverse modes which carry OAM. Radiation emitted from an electron beam propagating through an undulator will carry OAM either if the electrons are bunched into a helix or when electrons are radiating at a higher harmonic in a helical undulator. This radiation is structured in phase and intensity which vary transversely.

The first novel method investigated in this thesis looked at altering mode competition in order to get a dominant OAM mode, where the initial seed for amplification came from initial shot noise in the electron beam. Interaction between the electrons and the Gaussian mode was suppressed through a longitudinal delay of the electrons equivalent to a phase shift. The longitudinal shift was combined with a rotational shift which allowed disruption of the Gaussian mode without suppressing a higher-order, $|\ell| > 0$, mode. Simulations of the method showed that this allowed the OAM mode to self-select for amplification. This scheme suggests that FELs can be used to emit OAM radiation at the fundamental wavelength without the need for an external seed, however, physical realisation of the rotation could not be achieved without debunching the electron beam. Although this scheme is not currently feasible, it does demonstrate the mechanisms of transverse mode selection in a FEL.

The harmonic emission of a helical undulator is emitted off-axis with transverse phase distributions which closely resemble the Laguerre-Gaussian modes. Similarly,

the higher harmonics of planar undulators are emitted as Hermite-Gaussian modes. In Chapter 6 this was exploited in order to produce radiation where the polarisation state of the radiation varies transversely. Beams with transverse polarisation distributions are called Poincaré beams; structuring the spatial polarisation state of light can result in additional beneficial properties, such as the ability to focus more tightly. Three different polarisation topologies were simulated, chosen by changing the type of undulator and the phase change between them. Generation of these beams in a FEL increases the wavelength range over which this radiation is available and the results presented in this thesis are a major advance in the type and properties of beams that may be created by FELs and we expect it to lead to significant advances in FEL applications, opening up hitherto inaccessible research possibilities in important new areas such as the discrimination of chiral enantiomer molecules.

The final method proposed in this thesis is a technique which, for the first time, extends the capabilities of a FEL to include polarisation modulated output at timescales that approach the atomic unit of time. This is a significant improvement to current polarisation switching rates and has the benefit of being available at a wide range of tunable wavelengths into the hard X-ray. In Chapter 7 FEL simulations demonstrate trains of FEL-generated radiation pulses in which each pulse alternates between orthogonal linear or circular polarisation states. The technique is demonstrated in the soft X-ray, generating pulse trains that alternate polarisation in tens of attoseconds. This is a profound improvement on that currently available. This is an important result, providing new output uniquely enabled by FELs, and it is expected to lead to significant advances in FEL applications. As discussed in Section 7.6, future work will focus on extending this method to produce pulse trains where the handedness of the OAM of each pulse alternates.

The work in this thesis has aimed to increase the diversity of radiation available at FEL facilities. Providing new output uniquely enabled by FELs is expected it to lead to significant advances in FEL applications. As such, there is much interest in tailoring the FEL output to new exotic regimes and the work covered in this thesis contributes to this goal.

Bibliography

[1] B. W. McNeil and N. R. Thompson, "X-ray free-electron lasers," *Nature Photonics*, vol. 4, pp. 814–821, 2010.

[2] P. Abbamonte, F. Abild-Pedersen, P. Adams, M. Ahmed, F. Albert, R. A. Mori, P. Anfinrud, A. Aquila, M. Armstrong, J. Arthur, *et al.*, "New science opportunities enabled by lcls-ii x-ray lasers," tech. rep., SLAC National Accelerator Lab., Menlo Park, CA (United States), 2015.

[3] P. Emma, R. Akre, J. Arthur, R. Bionta, C. Bostedt, J. Bozek, A. Brachmann, P. Bucksbaum, R. Coffee, F.-J. Decker, *et al.*, "First lasing and operation of an ångstrom-wavelength free-electron laser," *Nature Photonics*, vol. 4, no. 9, p. 641, 2010.

[4] E. A. Schneidmiller and M. V. Yurkov, "Obtaining high degree of circular polarization at x-ray free electron lasers via a reverse undulator taper," *Phys. Rev. ST Accel. Beams*, vol. 16, p. 110702, Nov 2013.

[5] N. R. Thompson and B. W. J. McNeil, "Mode locking in a free-electron laser amplifier," *Phys. Rev. Lett.*, vol. 100, p. 203901, May 2008.

[6] L. T. Campbell, B. W. J. McNeil, and S. Reiche, "Two-colour free electron laser with wide frequency separation using a single monoenergetic electron beam," *New Journal of Physics*, vol. 16, p. 103019, oct 2014.

[7] A. Burnett, M. Borghesi, A. Comley, M. Dean, S. Diaz-Moreno, D. Dye, J. Greenwood, A. Higginbotham, A. Kirrander, J. Marangos, M. McMahon, R. Minns, M. Newton, A. Orville, T. Penfold, A. Regoutz, I. Robinson, D. Rugg,

S. Schroeder, J. van Thor, S. Vinko, S. Wall, J. Wark, A. Z. Julia Weinstein, and X. Zhang, "UK XFEL science case," 2020.

[8] W. Ackermann, G. Asova, V. Ayvazyan, A. Azima, N. Baboi, J. Bähr, V. Balandin, B. Beutner, A. Brandt, A. Bolzmann, *et al.*, "Operation of a free-electron laser from the extreme ultraviolet to the water window," *Nature photonics*, vol. 1, no. 6, pp. 336–342, 2007.

[9] T. Ishikawa, H. Aoyagi, T. Asaka, Y. Asano, N. Azumi, T. Bizen, H. Ego, K. Fukami, T. Fukui, Y. Furukawa, *et al.*, "A compact x-ray free-electron laser emitting in the sub-angstrom region," *Nature Photonics*, vol. 6, no. 8, pp. 540–544, 2012.

[10] E. Allaria, R. Appio, L. Badano, W. Barletta, S. Bassanese, S. Biedron, A. Borga, E. Busetto, D. Castronovo, P. Cinquegrana, *et al.*, "Highly coherent and stable pulses from the FERMI seeded free-electron laser in the extreme ultraviolet," *Nature Photonics*, vol. 6, no. 10, pp. 699–704, 2012.

[11] E. Allaria, D. Castronovo, P. Cinquegrana, P. Craievich, M. Dal Forno, M. B. Danailov, G. D'Auria, A. Demidovich, G. De Ninno, S. Di Mitri, B. Diviacco, W. M. Fawley, M. Ferianis, E. Ferrari, L. Froehlich, G. Gaio, D. Gauthier, L. Giannessi, R. Ivanov, B. Mahieu, N. Mahne, I. Nikolov, F. Parmigiani, G. Penco, L. Raimondi, C. Scafuri, C. Serpico, P. Sigalotti, S. Spampinati, C. Spezzani, M. Svandrlik, C. Svetina, M. Trovo, M. Veronese, D. Zangrando, and M. Zangrando, "Two-stage seeded soft-X-ray free-electron laser," *Nature Photonics*, vol. 7, pp. 913 EP –, 10 2013.

[12] H.-S. Kang, C.-K. Min, H. Heo, C. Kim, H. Yang, G. Kim, I. Nam, S. Y. Baek, H.-J. Choi, G. Mun, B. R. Park, Y. J. Suh, D. C. Shin, J. Hu, J. Hong, S. Jung, S.-H. Kim, K. Kim, D. Na, S. S. Park, Y. J. Park, J.-H. Han, Y. G. Jung, S. H. Jeong, H. G. Lee, S. Lee, S. Lee, W.-W. Lee, B. Oh, H. S. Suh, Y. W. Parc, S.-J. Park, M. H. Kim, N.-S. Jung, Y.-C. Kim, M.-S. Lee, B.-H. Lee, C.-W. Sung, I.-S. Mok, J.-M. Yang, C.-S. Lee, H. Shin, J. H. Kim, Y. Kim, J. H. Lee, S.-Y. Park,

J. Kim, J. Park, I. Eom, S. Rah, S. Kim, K. H. Nam, J. Park, J. Park, S. Kim, S. Kwon, S. H. Park, K. S. Kim, H. Hyun, S. N. Kim, S. Kim, S.-m. Hwang, M. J. Kim, C.-y. Lim, C.-J. Yu, B.-S. Kim, T.-H. Kang, K.-W. Kim, S.-H. Kim, H.-S. Lee, H.-S. Lee, K.-H. Park, T.-Y. Koo, D.-E. Kim, and I. S. Ko, "Hard x-ray free-electron laser with femtosecond-scale timing jitter," *Nature Photonics*, vol. 11, no. 11, pp. 708–713, 2017.

[13] F. R. Elder, A. M. Gurewitsch, R. V. Langmuir, and H. C. Pollock, "Radiation from electrons in a synchrotron," *Phys. Rev.*, vol. 71, pp. 829–830, Jun 1947.

[14] H. Motz, "Applications of the radiation from fast electron beams," *Journal of Applied Physics*, vol. 22, no. 5, pp. 527–535, 1951.

[15] H. Motz, W. Thon, and R. N. Whitehurst, "Experiments on radiation by fast electron beams," *Journal of Applied Physics*, vol. 24, no. 7, pp. 826–833, 1953.

[16] R. M. Phillips, "The ubitron, a high-power traveling-wave tube based on a periodic beam interaction in unloaded waveguide," *IRE Transactions on Electron Devices*, vol. 7, no. 4, pp. 231–241, 1960.

[17] L. R. Elias, W. M. Fairbank, J. M. J. Madey, H. A. Schwettman, and T. I. Smith, "Observation of stimulated emission of radiation by relativistic electrons in a spatially periodic transverse magnetic field," *Phys. Rev. Lett.*, vol. 36, pp. 717–720, Mar 1976.

[18] D. A. G. Deacon, L. R. Elias, J. M. J. Madey, G. J. Ramian, H. A. Schwettman, and T. I. Smith, "First operation of a free-electron laser," *Phys. Rev. Lett.*, vol. 38, pp. 892–894, Apr 1977.

[19] W. Colson, "One-body electron dynamics in a free electron laser," *Physics Letters A*, vol. 64, no. 2, pp. 190–192, 1977.

[20] F. Hopf, P. Meystre, M. Scully, and W. Louisell, "Classical theory of a free-electron laser," *Optics Communications*, vol. 18, no. 4, pp. 413–416, 1976.

[21] N. M. Kroll and W. A. McMullin, "Stimulated emission from relativistic electrons passing through a spatially periodic transverse magnetic field," *Phys. Rev. A*, vol. 17, pp. 300–308, Jan 1978.

[22] I. B. Bernstein and J. L. Hirshfield, "Amplification on a relativistic electron beam in a spatially periodic transverse magnetic field," *Phys. Rev. A*, vol. 20, pp. 1661–1670, Oct 1979.

[23] P. Sprangle and R. A. Smith, "Theory of free-electron lasers," *Phys. Rev. A*, vol. 21, pp. 293–301, Jan 1980.

[24] W. Colson, "The nonlinear wave equation for higher harmonics in free-electron lasers," *IEEE Journal of Quantum Electronics*, vol. 17, no. 8, pp. 1417–1427, 1981.

[25] R. Bonifacio, F. Casagrande, and G. Casati, "Cooperative and chaotic transition of a free electron laser Hamiltonian model," *Optics Communications*, vol. 40, no. 3, pp. 219–223, 1982.

[26] T. J. Orzechowski, B. Anderson, W. M. Fawley, D. Prosnitz, E. T. Scharlemann, S. Yarema, D. Hopkins, A. C. Paul, A. M. Sessler, and J. Wurtele, "Microwave radiation from a high-gain free-electron laser amplifier," *Phys. Rev. Lett.*, vol. 54, pp. 889–892, Mar 1985.

[27] M. Hogan, C. Pellegrini, J. Rosenzweig, G. Travish, A. Varfolomeev, S. Anderson, K. Bishofberger, P. Frigola, A. Murokh, N. Osmanov, S. Reiche, and A. Tremaine, "Measurements of high gain and intensity fluctuations in a self-amplified, spontaneous-emission free-electron laser," *Phys. Rev. Lett.*, vol. 80, pp. 289–292, Jan 1998.

[28] A. Tremaine, X. J. Wang, M. Babzien, I. Ben-Zvi, M. Cornacchia, H.-D. Nuhn, R. Malone, A. Murokh, C. Pellegrini, S. Reiche, J. Rosenzweig, and V. Yakimenko, "Experimental characterization of nonlinear harmonic radiation from a visible self-amplified spontaneous emission free-electron laser at saturation," *Phys. Rev. Lett.*, vol. 88, p. 204801, May 2002.

[29] M. Altarelli, R. Brinkmann, and M. Chergui, "The European x-ray free-electron laser. Technical design report," Jul 2007.

[30] E. Prat, R. Abela, M. Aiba, A. Alarcon, J. Alex, Y. Arbelo, C. Arrell, V. Arsov, C. Bacellar, C. Beard, *et al.*, "A compact and cost-effective hard x-ray free-electron laser driven by a high-brightness and low-energy electron beam," *Nature Photonics*, vol. 14, no. 12, pp. 748–754, 2020.

[31] H.-S. Kang, C.-K. Min, H. Heo, C. Kim, H. Yang, G. Kim, I. Nam, S. Y. Baek, H.-J. Choi, G. Mun, *et al.*, "Hard x-ray free-electron laser with femtosecond-scale timing jitter," *Nature Photonics*, vol. 11, no. 11, pp. 708–713, 2017.

[32] R. W. Schoenlein, "New science opportunities enabled by LCLS-II x-ray lasers," Tech. Rep. SLAC-R-1053, SLAC National Accelerator Laboratory, 2015.

[33] R. Bonifacio, F. Casagrande, G. Cerchioni, L. de Salvo Souza, P. Pierini, and N. Piovella, "Physics of the high-gain FEL and superradiance," *La Rivista del Nuovo Cimento (1978-1999)*, vol. 13, no. 9, pp. 1–69, 1990.

[34] B. W. J. McNeil and G. R. M. Robb, "Self-amplified coherent spontaneous emission in the planar wiggler free-electron laser," *Phys. Rev. E*, vol. 65, p. 046503, Apr 2002.

[35] N. R. Thompson, "Improved temporal coherence and short pulse generation in free electron lasers," 2013.

[36] D. J. Dunning, "Methods for the generation of ultra-short free-electron laser pulses," 2015.

[37] R. Bonifacio, C. Pellegrini, and L. Narducci, "Collective instabilities and high-gain regime in a free electron laser," *Optics Communications*, vol. 50, no. 6, pp. 373–378, 1984.

[38] B. W. McNeil and N. R. Thompson, "X-ray free-electron lasers," *Nature photonics*, vol. 4, no. 12, pp. 814–821, 2010.

[39] R. Bonifacio, B. W. J. McNeil, and P. Pierini, "Superradiance in the high-gain free-electron laser," *Phys. Rev. A*, vol. 40, pp. 4467–4475, Oct 1989.

[40] J. H. Poynting *et al.*, "The wave motion of a revolving shaft, and a suggestion as to the angular momentum in a beam of circularly polarised light," *Proc. R. Soc. Lond. A*, vol. 82, no. 557, pp. 560–567, 1909.

[41] L. Allen, M. W. Beijersbergen, R. Spreeuw, and J. Woerdman, "Orbital angular momentum of light and the transformation of Laguerre-Gaussian laser modes," *Physical Review A*, vol. 45, no. 11, p. 8185, 1992.

[42] H. He, M. E. J. Friese, N. R. Heckenberg, and H. Rubinsztein-Dunlop, "Direct observation of transfer of angular momentum to absorptive particles from a laser beam with a phase singularity," *Phys. Rev. Lett.*, vol. 75, pp. 826–829, Jul 1995.

[43] A. Mair, A. Vaziri, G. Weihs, and A. Zeilinger, "Entanglement of the orbital angular momentum states of photons," *Nature*, vol. 412, no. 6844, pp. 313–316, 2001.

[44] S. Fürhapter, A. Jesacher, S. Bernet, and M. Ritsch-Marte, "Spiral interferometry," *Opt. Lett.*, vol. 30, pp. 1953–1955, Aug 2005.

[45] J. Wang, J.-Y. Yang, I. M. Fazal, N. Ahmed, Y. Yan, H. Huang, Y. Ren, Y. Yue, S. Dolinar, M. Tur, *et al.*, "Terabit free-space data transmission employing orbital angular momentum multiplexing," *Nature photonics*, vol. 6, no. 7, pp. 488–496, 2012.

[46] M. J. Padgett, "Orbital angular momentum 25 years on," *Opt. Express*, vol. 25, pp. 11265–11274, May 2017.

[47] A. M. Yao and M. J. Padgett, "Orbital angular momentum: origins, behavior and applications," *Adv. Opt. Photon.*, vol. 3, pp. 161–204, Jun 2011.

[48] J. B. Götte and S. M. Barnett, *Light beams carrying orbital angular momentum*, p. 1–30. Cambridge University Press, 2012.

[49] A. E. Siegman, "Lasers university science books," *Mill Valley, CA*, vol. 37, no. 208, p. 169, 1986.

[50] L. Allen, M. Padgett, and M. Babiker, "IV The orbital angular momentum of light," vol. 39 of *Progress in Optics*, pp. 291 – 372, Elsevier, 1999.

[51] L. Allen, M. W. Beijersbergen, R. J. C. Spreeuw, and J. P. Woerdman, "Orbital angular momentum of light and the transformation of Laguerre-Gaussian laser modes," *Phys. Rev. A*, vol. 45, pp. 8185–8189, Jun 1992.

[52] S. M. Barnett and L. Allen, "Orbital angular momentum and nonparaxial light beams," *Optics Communications*, vol. 110, no. 5, pp. 670 – 678, 1994.

[53] M. Beijersbergen, R. Coerwinkel, M. Kristensen, and J. Woerdman, "Helical-wavefront laser beams produced with a spiral phaseplate," *Optics Communications*, vol. 112, no. 5, pp. 321–327, 1994.

[54] G. Turnbull, D. Robertson, G. Smith, L. Allen, and M. Padgett, "The generation of free-space Laguerre-Gaussian modes at millimetre-wave frequencies by use of a spiral phaseplate," *Optics Communications*, vol. 127, no. 4, pp. 183–188, 1996.

[55] S. S. R. Oemrawsingh, J. A. W. van Houwelingen, E. R. Eliel, J. P. Woerdman, E. J. K. Verstegen, J. G. Kloosterboer, and G. W. 't Hooft, "Production and characterization of spiral phase plates for optical wavelengths," *Appl. Opt.*, vol. 43, pp. 688–694, Jan 2004.

[56] V. Bazhenov, M. Soskin, and M. Vasnetsov, "Screw dislocations in light wavefronts," *Journal of Modern Optics*, vol. 39, no. 5, pp. 985–990, 1992.

[57] S. Sasaki and I. McNulty, "Proposal for generating brilliant x-ray beams carrying orbital angular momentum," *Physical review letters*, vol. 100, no. 12, p. 124801, 2008.

[58] S. Sasaki, I. McNulty, and R. Dejus, "Undulator radiation carrying spin and orbital angular momentum," *Nuclear Instruments and Methods in Physics Re-*

search Section A: Accelerators, Spectrometers, Detectors and Associated Equipment, vol. 582, no. 1, pp. 43–46, 2007. Proceedings of the 14th National Conference on Synchrotron Radiation Research.

[59] J. Bahrdt, K. Holldack, P. Kuske, R. Müller, M. Scheer, and P. Schmid, "First observation of photons carrying orbital angular momentum in undulator radiation," *Phys. Rev. Lett.*, vol. 111, p. 034801, Jul 2013.

[60] E. Hemsing, M. Dunning, C. Hast, T. Raubenheimer, and D. Xiang, "First characterization of coherent optical vortices from harmonic undulator radiation," *Phys. Rev. Lett.*, vol. 113, p. 134803, Sep 2014.

[61] P. R. Ribič, B. Rösner, D. Gauthier, E. Allaria, F. Döring, L. Foglia, L. Giannessi, N. Mahne, M. Manfredda, C. Masciovecchio, *et al.*, "Extreme-ultraviolet vortices from a free-electron laser," *Physical Review X*, vol. 7, no. 3, p. 031036, 2017.

[62] P. Liu, J. Yan, A. Afanasev, S. V. Benson, H. Hao, S. F. Mikhailov, V. G. Popov, and Y. K. Wu, "Orbital angular momentum beam generation using a free-electron laser oscillator," 2020.

[63] E. Hemsing, A. Gover, and J. Rosenzweig, "Virtual dielectric waveguide mode description of a high-gain free-electron laser. I. theory," *Physical Review A*, vol. 77, no. 6, p. 063830, 2008.

[64] E. Hemsing, A. Gover, and J. Rosenzweig, "Virtual dielectric waveguide mode description of a high-gain free-electron laser. II. modeling and numerical simulations," *Physical Review A*, vol. 77, no. 6, p. 063831, 2008.

[65] E. Hemsing, P. Musumeci, S. Reiche, R. Tikhoplav, A. Marinelli, J. Rosenzweig, and A. Gover, "Helical electron-beam microbunching by harmonic coupling in a helical undulator," *Physical review letters*, vol. 102, no. 17, p. 174801, 2009.

[66] E. Hemsing, A. Knyazik, M. Dunning, D. Xiang, A. Marinelli, C. Hast, and J. B. Rosenzweig, "Coherent optical vortices from relativistic electron beams," *Nature Physics*, vol. 9, no. 9, p. 549, 2013.

[67] E. Hemsing, "Coherent photons with angular momentum in a helical afterburner," *Phys. Rev. Accel. Beams*, vol. 23, p. 020703, Feb 2020.

[68] J. A. J. A. Clarke, *The science and technology of undulators and wigglers*. Oxford series on synchrotron radiation ; 4, Oxford: Oxford University Press, 2004.

[69] E. W. Hemsing, *Generation and Amplification of Coherent Radiation with Optical Orbital Angular Momentum in a Free-Electron Laser*. PhD thesis, University of California, Los Angeles, Jan. 2011.

[70] S. Reiche, "Genesis 1.3: a fully 3D time-dependent FEL simulation code," *Nuclear Instruments and Methods in Physics Research Section A: Accelerators, Spectrometers, Detectors and Associated Equipment*, vol. 429, no. 1, pp. 243–248, 1999.

[71] S. Reiche, P. Musumeci, and K. Goldammer, "Recent upgrade to the free-electron laser code GENESIS 1.3," in *2007 IEEE Particle Accelerator Conference (PAC)*, pp. 1269–1271, 2007.

[72] L. Campbell and B. McNeil, "Puffin: A three dimensional, unaveraged free electron laser simulation code," *Physics of Plasmas*, vol. 19, no. 9, p. 093119, 2012.

[73] L. Campbell, B. McNeil, J. Smith, and P. Traczykowski, "An updated description of the FEL simulation code puffin," in *Proc. 9th International Particle Accelerator Conference (IPAC'18), Vancouver, BC, Canada, April 29-May 4, 2018*, no. 9 in International Particle Accelerator Conference, (Geneva, Switzerland), pp. 4579–4582, JACoW Publishing, June 2018.

[74] `https://github.com/UKFELs/Puffin`. Accessed: 2021-07-14.

[75] J. A. Clarke, D. Angal-Kalinin, N. Bliss, R. Buckley, S. Buckley, R. Cash, P. Corlett, L. Cowie, G. Cox, G. P. Diakun, D. J. Dunning, B. D. Fell, A. Gallagher, P. Goudket, A. R. Goulden, D. M. P. Holland, S. P. Jamison, J. K. Jones, A. S. Kalinin, W. Liggins, L. Ma, K. B. Marinov, B. Martlew, P. A. McIntosh, J. W. McKenzie, K. J. Middleman, B. L. Militsyn, A. J. Moss, B. D. Muratori, M. D. Roper, R. Santer, Y. Saveliev, E. Snedden, R. J. Smith, S. L.

Smith, M. Surman, T. Thakker, N. R. Thompson, R. Valizadeh, A. E. Wheelhouse, P. H. Williams, R. Bartolini, I. Martin, R. Barlow, A. Kolano, G. Burt, S. Chattopadhyay, D. Newton, A. Wolski, R. B. Appleby, H. L. Owen, M. Serluca, G. Xia, S. Boogert, A. Lyapin, L. Campbell, B. W. J. McNeil, and V. V. Paramonov, "CLARA conceptual design report," *Journal of Instrumentation*, vol. 9, pp. T05001–T05001, may 2014.

[76] B. W. McNeil, M. W. Poole, and G. Robb, "Inducing strong density modulation with small energy dispersion in particle beams and the harmonic amplifier free electron laser," in *Particle Accelerator Conference, 2005. PAC 2005. Proceedings of the*, pp. 1718–1720, 2005.

[77] E. Hemsing, A. Marinelli, and J. Rosenzweig, "Generating optical orbital angular momentum in a high-gain free-electron laser at the first harmonic," *Physical review letters*, vol. 106, no. 16, p. 164803, 2011.

[78] J. Morgan, B. Muratori, B. McNeil, P. Williams, and A. Wolski, "Orbital angular momentum from SASE," in *Proc. FEL'19*, no. 39 in Free Electron Laser Conference, pp. 218–221, JACoW Publishing, Geneva, Switzerland, nov 2019.

[79] Q. Zhan, "Cylindrical vector beams: from mathematical concepts to applications," *Adv. Opt. Photon.*, vol. 1, pp. 1–57, Jan 2009.

[80] A. M. Beckley, T. G. Brown, and M. A. Alonso, "Full Poincaré beams," *Opt. Express*, vol. 18, pp. 10777–10785, May 2010.

[81] E. J. Galvez, S. Khadka, W. H. Schubert, and S. Nomoto, "Poincaré-beam patterns produced by nonseparable superpositions of Laguerre–Gauss and polarization modes of light," *Appl. Opt.*, vol. 51, pp. 2925–2934, May 2012.

[82] R. Dorn, S. Quabis, and G. Leuchs, "Sharper focus for a radially polarized light beam," *Phys. Rev. Lett.*, vol. 91, p. 233901, Dec 2003.

[83] H. Rubinsztein-Dunlop, A. Forbes, M. V. Berry, M. R. Dennis, D. L. Andrews, M. Mansuripur, C. Denz, C. Alpmann, P. Banzer, T. Bauer, E. Karimi, L. Mar-

rucci, M. Padgett, M. Ritsch-Marte, N. M. Litchinitser, N. P. Bigelow, C. Rosales-Guzmán, A. Belmonte, J. P. Torres, T. W. Neely, M. Baker, R. Gordon, A. B. Stilgoe, J. Romero, A. G. White, R. Fickler, A. E. Willner, G. Xie, B. McMorran, and A. M. Weiner, "Roadmap on structured light," *Journal of Optics*, vol. 19, p. 013001, nov 2016.

[84] F. Bouchard, H. Larocque, A. M. Yao, C. Travis, I. De Leon, A. Rubano, E. Karimi, G.-L. Oppo, and R. W. Boyd, "Polarization shaping for control of nonlinear propagation," *Phys. Rev. Lett.*, vol. 117, p. 233903, Dec 2016.

[85] A. V. Nesterov and V. G. Niziev, "Laser beams with axially symmetric polarization," *Journal of Physics D: Applied Physics*, vol. 33, pp. 1817–1822, jul 2000.

[86] X. Hao, C. Kuang, T. Wang, and X. Liu, "Effects of polarization on the de-excitation dark focal spot in STED microscopy," *Journal of Optics*, vol. 12, p. 115707, oct 2010.

[87] B. Sick, B. Hecht, and L. Novotny, "Orientational imaging of single molecules by annular illumination," *Phys. Rev. Lett.*, vol. 85, pp. 4482–4485, Nov 2000.

[88] L. Novotny, M. R. Beversluis, K. S. Youngworth, and T. G. Brown, "Longitudinal field modes probed by single molecules," *Phys. Rev. Lett.*, vol. 86, pp. 5251–5254, Jun 2001.

[89] V. G. Niziev, R. S. Chang, and A. V. Nesterov, "Generation of inhomogeneously polarized laser beams by use of a Sagnac interferometer," *Appl. Opt.*, vol. 45, pp. 8393–8399, Nov 2006.

[90] S. Chen, X. Zhou, Y. Liu, X. Ling, H. Luo, and S. Wen, "Generation of arbitrary cylindrical vector beams on the higher order Poincaré sphere," *Opt. Lett.*, vol. 39, pp. 5274–5276, Sep 2014.

[91] A. G. Peele, P. J. McMahon, D. Paterson, C. Q. Tran, A. P. Mancuso, K. A. Nugent, J. P. Hayes, E. Harvey, B. Lai, and I. McNulty, "Observation of an x-ray vortex," *Opt. Lett.*, vol. 27, pp. 1752–1754, Oct 2002.

[92] A. G. Peele, K. A. Nugent, A. P. Mancuso, D. Paterson, I. McNulty, and J. P. Hayes, "X-ray phase vortices: theory and experiment," *J. Opt. Soc. Am. A*, vol. 21, pp. 1575–1584, Aug 2004.

[93] C. Hernández-García, A. Turpin, J. S. Román, A. Picón, R. Drevinskas, A. Cerkauskaite, P. G. Kazansky, C. G. Durfee, and I. nigo J. Sola, "Extreme ultraviolet vector beams driven by infrared lasers," *Optica*, vol. 4, pp. 520–526, May 2017.

[94] S. Matsuba, K. Kawase, A. Miyamoto, S. Sasaki, M. Fujimoto, T. Konomi, N. Yamamoto, M. Hosaka, and M. Katoh, "Generation of vector beam with tandem helical undulators," *Applied Physics Letters*, vol. 113, no. 2, p. 021106, 2018.

[95] R. P. Cameron, J. B. Götte, S. M. Barnett, and A. M. Yao, "Chirality and the angular momentum of light," *Phil. Trans. R. Soc. A*, vol. 375, p. 20150433, 2017.

[96] S. Franke-Arnold, J. Leach, M. J. Padgett, V. E. Lembessis, D. Ellinas, A. J. Wright, J. M. Girkin, P. Öhberg, and A. S. Arnold, "Optical ferris wheel for ultracold atoms," *Opt. Express*, vol. 15, pp. 8619–8625, Jul 2007.

[97] A. S. Arnold, "Extending dark optical trapping geometries," *Opt. Lett.*, vol. 37, pp. 2505–2507, Jul 2012.

[98] J. F. Nye, "Lines of circular polarization in electromagnetic wave fields," *Proc. R Soc. Lond. A*, vol. 389, p. 279, 1983.

[99] M. Beijersbergen, L. Allen, H. van der Veen, and J. Woerdman, "Astigmatic laser mode converters and transfer of orbital angular momentum," *Optics Communications*, vol. 96, no. 1, pp. 123 – 132, 1993.

[100] K. O. M. Dennis and M. Padgett, "Singular optics: optical vortices and polarization singularities," *Prog. Opt.*, vol. 53, pp. 293–363, 2009.

[101] B. E. A. Saleh and M. C. Teich, *Fundamentals of Photonics*. Wiley, New York, 2007.

[102] A. A. Lutman, J. P. MacArthur, M. Ilchen, A. O. Lindahl, J. Buck, R. N. Coffee, G. L. Dakovski, L. Dammann, Y. Ding, H. A. Dürr, *et al.*, "Polarization control in an x-ray free-electron laser," *Nature photonics*, vol. 10, no. 7, p. 468, 16.

[103] J. P. MacArthur, A. A. Lutman, J. Krzywinski, and Z. Huang, "Microbunch rotation and coherent undulator radiation from a kicked electron beam," *Phys. Rev. X*, vol. 8, p. 041036, Nov 2018.

[104] E. Ferrari, E. Roussel, J. Buck, C. Callegari, R. Cucini, G. De Ninno, B. Diviacco, D. Gauthier, L. Giannessi, L. Glaser, *et al.*, "Free electron laser polarization control with interfering crossed polarized fields," *Physical Review Accelerators and Beams*, vol. 22, no. 8, p. 080701, 2019.

[105] H. Deng, T. Zhang, L. Feng, C. Feng, B. Liu, X. Wang, T. Lan, G. Wang, W. Zhang, X. Liu, *et al.*, "Polarization switching demonstration using crossed-planar undulators in a seeded free-electron laser," *Physical Review Special Topics-Accelerators and Beams*, vol. 17, no. 2, p. 020704, 2014.

[106] S. Sasaki, "Analyses for a planar variably-polarizing undulator," *Nuclear Instruments and Methods in Physics Research Section A: Accelerators, Spectrometers, Detectors and Associated Equipment*, vol. 347, no. 1, pp. 83 – 86, 1994.

[107] A. B. Temnykh, "Delta undulator for Cornell energy recovery linac," *Phys. Rev. ST Accel. Beams*, vol. 11, p. 120702, Dec 2008.

[108] Y. Li, B. Faatz, and J. Pflüeger, "3D Polarization properties for crossed-planar undulators," *DESY print TESLA-FEL*, 2010.

[109] E. Hemsing, "Coherent photons with angular momentum in a helical afterburner," *Phys. Rev. Accel. Beams*, vol. 23, p. 020703, Feb 2020.

[110] S. Serkez, A. Trebushinin, M. Veremchuk, and G. Geloni, "Method for polarization shaping at free-electron lasers," *Phys. Rev. Accel. Beams*, vol. 22, p. 110705, Nov 2019.

[111] D. J. Dunning, B. W. J. McNeil, and N. R. Thompson, "Few-cycle pulse generation in an x-ray free-electron laser," *Phys. Rev. Lett.*, vol. 110, p. 104801, Mar 2013.

[112] E. Kur, D. J. Dunning, B. W. J. McNeil, J. Wurtele, and A. A. Zholents, "A wide bandwidth free-electron laser with mode locking using current modulation," *New Journal of Physics*, vol. 13, p. 063012, jun 2011.

[113] J. Li, J. Lu, A. Chew, S. Han, J. Li, Y. Wu, H. Wang, S. Ghimire, and Z. Chang, "Attosecond science based on high harmonic generation from gases and solids," *Nature Communications*, vol. 11, no. 1, pp. 1–13, 2020.

[114] D. Dunning, B. Mc Neil, N. Thompson, and P. Williams, "Start-to-end modelling of a mode-locked optical klystron free electron laser amplifier," *Physics of Plasmas*, vol. 18, no. 7, p. 073104, 2011.

[115] R. Bonifacio, R. Corsini, and P. Pierini, "Theory of the high-gain optical klystron," *Phys. Rev. A*, vol. 45, pp. 4091–4096, Mar 1992.

[116] S. Rozen, A. Comby, E. Bloch, S. Beauvarlet, D. Descamps, B. Fabre, S. Petit, V. Blanchet, B. Pons, N. Dudovich, and Y. Mairesse, "Controlling subcycle optical chirality in the photoionization of chiral molecules," *Phys. Rev. X*, vol. 9, p. 031004, Jul 2019.

[117] G. Schütz, W. Wagner, W. Wilhelm, P. Kienle, R. Zeller, R. Frahm, and G. Materlik, "Absorption of circularly polarized x rays in iron," *Phys. Rev. Lett.*, vol. 58, pp. 737–740, Feb 1987.

[118] G. van der Laan and A. I. Figueroa, "X-ray magnetic circular dichroism—a versatile tool to study magnetism," *Coordination Chemistry Reviews*, vol. 277-278, pp. 95 – 129, 2014. Following Chemical Structures using Synchrotron Radiation.

[119] M. Suzuki, N. Kawamura, and T. Ishikawa, "Application of optical scanner to switching of x-ray photon helicities at kHz range," *Review of Scientific Instruments*, vol. 74, no. 1, pp. 19–22, 2003.

[120] M. Först, C. Manzoni, S. Kaiser, Y. Tomioka, Y. Tokura, R. Merlin, and A. Cavalleri, "Nonlinear phononics as an ultrafast route to lattice control," *Nature Physics*, vol. 7, no. 11, p. 854, 2011.

[121] T. Kampfrath, A. Sell, G. Klatt, A. Pashkin, S. Mährlein, T. Dekorsy, M. Wolf, M. Fiebig, A. Leitenstorfer, and R. Huber, "Coherent terahertz control of antiferromagnetic spin waves," *Nature Photonics*, vol. 5, no. 1, pp. 31–34, 2011.

[122] J. Sánchez-Barriga, E. Golias, A. Varykhalov, J. Braun, L. V. Yashina, R. Schumann, J. Minár, H. Ebert, O. Kornilov, and O. Rader, "Ultrafast spin-polarization control of dirac fermions in topological insulators," *Phys. Rev. B*, vol. 93, p. 155426, Apr 2016.

[123] J. D. Bull, N. A. Jaeger, H. Kato, M. Fairburn, A. Reid, and P. Ghanipour, "40-GHz electro-optic polarization modulator for fiber optic communications systems," in *Photonics North 2004: Optical Components and Devices* (J. C. Armitage, S. Fafard, R. A. Lessard, and G. A. Lampropoulos, eds.), vol. 5577, pp. 133 – 143, International Society for Optics and Photonics, SPIE, 2004.

[124] Y. Yang, K. Kelley, E. Sachet, S. Campione, T. S. Luk, J.-P. Maria, M. B. Sinclair, and I. Brener, "Femtosecond optical polarization switching using a cadmium oxide-based perfect absorber," *Nature Photonics*, vol. 11, no. 6, p. 390, 2017.

[125] L. H. Nicholls, F. J. Rodríguez-Fortuño, M. E. Nasir, R. M. Córdova-Castro, N. Olivier, G. A. Wurtz, and A. V. Zayats, "Ultrafast synthesis and switching of light polarization in nonlinear anisotropic metamaterials," *Nature Photonics*, vol. 11, no. 10, pp. 628–633, 2017.

[126] K. Holldack, C. Schüssler-Langeheine, P. Goslawski, N. Pontius, T. Kachel, F. Armborst, M. Ries, A. Schälicke, M. Scheer, W. Frentrup, *et al.*, "Flipping the helicity of x-rays from an undulator at unprecedented speed," *Communications Physics*, vol. 3, no. 1, pp. 1–8, 2020.

[127] S. Serkez, A. Trebushinin, M. Veremchuk, and G. Geloni, "Method for polarization shaping at free-electron lasers," *Phys. Rev. Accel. Beams*, vol. 22, p. 110705, Nov 2019.

[128] A. A. Lutman, T. J. Maxwell, J. P. MacArthur, M. W. Guetg, N. Berrah, R. N. Coffee, Y. Ding, Z. Huang, A. Marinelli, S. Moeller, *et al.*, "Fresh-slice multicolour x-ray free-electron lasers," *Nature Photonics*, vol. 10, no. 11, pp. 745–750, 2016.

[129] A. Kirilyuk, A. V. Kimel, and T. Rasing, "Ultrafast optical manipulation of magnetic order," *Rev. Mod. Phys.*, vol. 82, pp. 2731–2784, Sep 2010.

[130] D. Dunning, N. Thompson, P. Williams, and B. McNeil, "Start-to-end simulations of SASE and HHG-seeded mode-locked FEL," *Cockcroft Preprints*, 2009.

[131] D. J. Dunning, B. W. J. Mc Neil, N. R. Thompson, and P. H. Williams, "Start-to-end modelling of a mode-locked optical klystron free electron laser amplifier," *Physics of Plasmas*, vol. 18, no. 7, p. 073104, 2011.

Appendix A

Publications

Conference Paper

- J. Morgan, B.W.J. McNeil, B.D. Muratori, P.Williams and A. Wolski., "Orbital angular momentum from SASE" *29th Free electron laser conference,* TUP072, 2019

Refereed Publications

- J.Morgan, E. Hemsing, B.W.J. McNeil and A. Yao., "Free electron laser generation of x-ray Poincaré beams," *New J. Phys.,* vol. 22, p. 072001, 2020
- J. Morgan and B.W.J. McNeil., "Attosecond polarization modulation of x-ray radiation in a free electron laser" *Phys. Rev. Accel. Beams,* vol. 24 p. 010701, 2021

ISBN: 978-3-95450-210-3 doi:10.18429/JACoW-FEL2019-TUP072

ORBITAL ANGULAR MOMENTUM FROM SASE

J. Morgan[1,2], B.W.J. M^{c}Neil[1,2], B.D. Muratori[2,3], P. Williams[2,3], A. Wolski[2,4]
[1]SUPA, Department of Physics, University of Strathclyde, Glasgow
[2]Cockcroft Institute, Warrington, UK
[3]ASTeC, STFC Daresbury Laboratory, Warrington, UK
[4]University of Liverpool, Liverpool, UK

Abstract

To reach very short wavelengths and high intensities of light, free-electron lasers, FELs, are used which produce radiation from amplified noise in an electron beam. In this SASE regime, mode competition dictates that the dominant transverse mode of the radiation will be Gaussian. A method is proposed to suppress the Gaussian mode via phase shifts which allows higher order Laguerre-Gaussian modes to be amplified. These modes are of interest as they carry orbital angular momentum, OAM. Techniques for generating OAM radiation with a FEL have been proposed previously, however, this is the first look at altering mode competition in order to get a dominant OAM mode starting from the initial shot noise in the electron beam.

INTRODUCTION

Recently, much attention has been paid to light which carries OAM. This light has helical phase-fronts characterized by $e^{il\phi}$, where ϕ is the azimuthal coordinate and l is an integer number named the topical charge. The magnitude of l gives the number of intertwined helices in the phase front and the sign of l gives the handedness of these helices. Conventional methods for generating OAM light require downstream optics which convert the radiation from a standard laser [1]. This has its limitations. The optical elements' damage threshold limits the brightness and wavelength of light which is transmitted and constraints arise from the lasers themselves. In contrast, in the FEL, the phase structure of light can be controlled through the manipulation of the electrons themselves and offers the benefit of having a wide range of wavelengths accessible.

Previous work has shown that OAM can be produced in a FEL through a variety of methods. Recently, OAM radiation has been produced at FERMI through harmonic lasing schemes involving helical undulators as well as using a spiral zone plate to convert the radiation downstream from normal FEL output [2]. Another method from Hemsing and colleges creates OAM radiation by first bunching electrons into a helix through second harmonic interaction with a helical undulator. [3].

The current methods for producing OAM radiation in a FEL have their limitations. The intensity of light from harmonic lasing schemes is less than that at the fundamental frequency [2]. Other methods rely on seeding the FEL either with an OAM seed laser for amplification or with a pre-bunched electron beam. When a FEL is seeded in this way, the output is restricted by the quality of seeds available. This causes difficulty at very short wavelengths as a seed may not be available at the required wavelength and the intensity of the seed must be large to overcome the initial shot noise in the beam. It would be useful, instead, for the initial seed for amplification to come from the shot noise in the electron beam itself. This work looks at the feasibility of just this, generating OAM through suppression of the Gaussian mode.

THEORY

Electrons enter the undulator with random phases due to shot noise in the electron gun. In the self-amplified-spontaneous emission (SASE) mode of operation, the initial amplitude due to the noise acts as a seed for the FEL interaction and is amplified. The incoherence of the electrons is mimicked by the radiation they produce. This radiation can be described by a superposition of the orthogonal Laguerre-Gaussian beams, $LG_{pl}(\phi,\hat{r})$,

$$E(\phi,\hat{r}) = \sum_{l=-\infty}^{\infty}\sum_{p=0}^{\infty} a_{pl} LG_{pl}(\phi,\hat{r}), \qquad (1)$$

where a_{pl} is the initial mode amplitude. The Laguerre-Gaussian, LG, modes are chosen as they provide a convenient mode basis and are often used in the study of OAM beams. These modes are written in terms of their OAM index l and the radial mode index p. The fundamental Gaussian mode is found when $p = l = 0$.

All of the modes will have a contribution from the initial electron density. However, due to their transverse profile, the higher order modes have longer gain lengths [4] with the shortest gain length belonging to the Gaussian mode. The Gaussian mode, therefore, dominates FEL interaction, suppressing the higher order modes, leading to the Gaussian mode of operation typical of a FEL. Here we demonstrate that suppressing the Gaussian mode will lead to the amplification of the higher order modes.

Suppression of the Gaussian Mode

It is possible to disrupt the interaction between electrons and radiation through a relative phase shift. A longitudinal delay of the electrons which shifts the electron phase relative to the fundamental wavelength by $\Delta\theta$ will shift the electrons relative to the nth harmonic by $n\Delta\theta$. It has been demonstrated that the exponential gain of the fundamental wavelength can be suppressed when $\Delta\theta$ is a non-integer multiple of 2π and can increase the power in higher harmonics [5]. Instead of considering the higher harmonics of

ISBN: 978-3-95450-210-3 doi:10.18429/JACoW-FEL2019-TUP072

the radiation, this work looks at the higher order transverse modes at the fundamental wavelength.

Examination of the transverse phase profile of the Laguerre-Gaussian modes indicates that a rotational shift, $\Delta\phi_r$, of the electron beam about the longitudinal axis results in a relative phase shift between the electrons and the transverse modes of $l\Delta\phi_r$. The total phase change, $\Delta\Psi_l$, between the electrons and the different l modes from the combination of longitudinal and rotational shifts is, therefore,

$$\Delta\Psi_l = \Delta\theta + l\Delta\phi_r \tag{2}$$

Eq. 2 describes how, through careful selection of $\Delta\theta$ and $\Delta\phi_r$, different relative phase changes between the electrons and the OAM modes can be achieved. If successive repetition of the shifts causes the exponential gain of the Gaussian mode to be disrupted - such that the gain length of the Gaussian mode is longer than of the higher order modes - then a dominant OAM mode will self-select for amplification.

RESULTS

Initial Results

The FEL is modeled using the FEL simulation code Puffin [6]. Presented first, is the result of rotating the electrons along the longitudinal axis according to the rotation matrix,

$$R(\phi_r) = \begin{bmatrix} \cos\phi_r & 0 & -\sin\phi_r & 0 \\ 0 & \cos\phi_r & 0 & -\sin\phi_r \\ \sin\phi_r & 0 & \cos\phi_r & 0 \\ 0 & \sin\phi_r & 0 & \cos\phi_r \end{bmatrix} \tag{3}$$

which acts on the phase space vector constructed from the vaiables (x, p_x, y, p_y), where x and y are the transverse coordinates, and p_x and p_y are the conjugate of momenta. The rotation is applied - along with a longitudinal shift - between undulator modules each around a gain length long. In order to alter mode competition to select for a LG_{01} mode, the shift pairs are chosen so that $\Delta\Psi_1 = 2\pi$. The set-up utilizes three alternating pairs of shifts, the longitudinal shifts, $\Delta\theta = \pi/2, \pi$ and $3\pi/2$ and the corresponding rotational shifts $\Delta\phi_r = 3\pi/2, \pi$ and $\pi/2$ respectively. These sections are repeated until the end of the undulator lattice.

The results of this set-up are displayed in Fig.1. Decomposition of the power into the different Laguerre-Gaussian modes demonstrates that suppressing the competing transverse modes means the LG_{01} mode dominates the interaction. This causes the LG_{01} mode to grow over an order of magnitude above the Gaussian mode. Also included in the figure is the bunching factor of the different helical modes calculated using [7],

$$b_l = \langle \exp(i\theta_j - il\phi) \rangle, \tag{4}$$

where the brackets indicate the ensemble average over the whole electron beam. The b_1 factor has exponential growth as the electrons propagate through the undulator while the bunching factors for the competing modes b_0 and b_{-1} grow

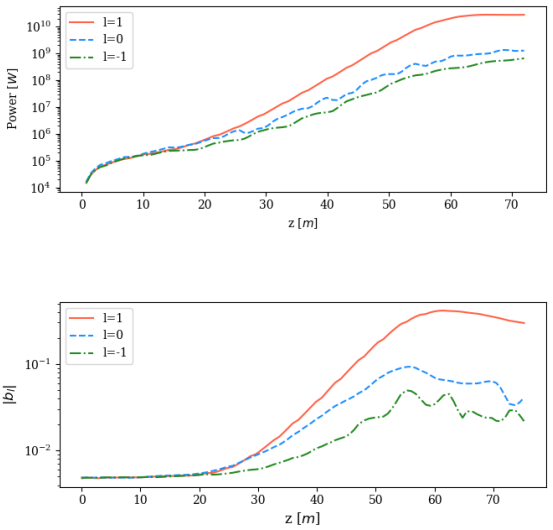

Figure 1: Time-averaged power decomposition of the fundamental frequency into Laguerre-Gaussian modes (top) and mean helical microbunching factor (bottom) when the phase shifts $\Delta\theta = \pi$, $\Delta\phi_r = \pi$; $\Delta\theta = 3\pi/2$, $\Delta\phi_r = \pi/2$; and $\Delta\theta = \pi/2$, $\Delta\phi_r = 3\pi/2$ are applied between undulator modules. This results in the most power being contained in the LG_{01} mode.

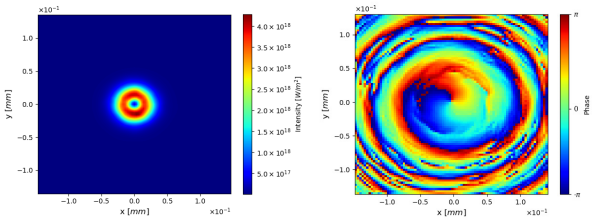

Figure 2: Intensity (left) and phase (right) at $z = 55.28\ m$ when the phase shifts $\Delta\theta = \pi$, $\Delta\phi_r = \pi$; $\Delta\theta = 3\pi/2$, $\Delta\phi_r = \pi/2$; and $\Delta\theta = \pi/2$, $\Delta\phi_r = 3\pi/2$ are applied between undulator modules.

at a slower rate. This set has not been optimized and further disruption of the Gaussian mode may be possible. Further evidence of the OAM mode is provided in Fig. 2 which shows a snapshot of the phase and intensity of radiation near saturation. The phase of the radiation has a transverse profile typical to the LG_{01} mode and the intensity is the expected doughnut structure of OAM modes.

How to Rotate an Electron Beam

The results presented above use a point transform to rotate the electron beam. Investigated here is a physical method to achieve such a transform. A beamline for rotating a beam through an arbitrary angle around the longitudinal axis can be constructed from a set of quadrupoles with appropriate tilt angles around that axis. The design that we present here is based on that of Talman [8], who used a similar system

ISBN: 978-3-95450-210-3 doi:10.18429/JACoW-FEL2019-TUP072

for achieving a "Möbius" transformation in a storage ring. The rotation matrix described by (3) can be created from,

$$\bar{M}\left(\frac{\phi_r}{2}+\frac{\pi}{4}\right)\bar{M}\left(-\frac{\pi}{4}\right)=R(\phi_r) \tag{5}$$

The matrices $\bar{M}$ are defined as,

$$\bar{M}(\theta)=R(\theta)MR^{-1}(\theta) \tag{6}$$

where:

$$M=\begin{bmatrix}\cos\mu & \beta\sin\mu & 0 & 0\\ -\frac{1}{\beta}\sin\mu & \cos\mu & 0 & 0\\ 0 & 0 & -\cos\mu & -\beta\sin\mu\\ 0 & 0 & \frac{1}{\beta}\sin\mu & -\cos\mu\end{bmatrix} \tag{7}$$

represents a phase advance through angles μ and $\mu+\pi$ in the transverse and horizontal spaces, respectively. The required transformation M can be achieved using a set of 5 quadrupoles arranged symetrically:

$$M=Q_1D_AQ_2D_BQ_3D_BQ_2D_AQ_1 \tag{8}$$

where Q_n is the transfer matrix for a quadrupole of focusing strength k_1L_n and $D_{A(B)}$ is the transfer matrix for a drift of length $L_{A(B)}$. A transformation $\bar{M}(\theta)$ can be constructed using the same set of quadrupole magnets, but with each set of quadrupoles tilted by an angle, θ, around the longitudinal axis.

Using the thin-lens approximation for the quadrupole magnets, the matrix M in (8) can be expressed in terms of the quadrupole strengths and drift lengths. Equation (7) then provides a set of constraints from which the quadrupole strengths and drift lengths can be found for a given μ and β. Not all values of μ and β admit physical solutions. However, a solution can be found for $\mu=\pi/2$, in which case the required focusing strengths are,

$$k_1L_1=\frac{L_B\xi}{L_A^2-L_B^2}\qquad k_1L_2=-k_1L_3=\frac{\xi}{L_B} \tag{9}$$

and the drift length L_B is given by:

$$L_B=\frac{2}{3}\left(\eta+\frac{1}{2}+\frac{1}{\eta}\right)L_A \tag{10}$$

The quantities ξ and η are defined as:

$$\xi^2=1+\frac{L_B}{L_A}\quad \eta^3=\frac{27}{16}\frac{\beta^2}{L_A^2}\left(1+\sqrt{1-\frac{32}{27}\frac{L_A^2}{\beta^2}}\right)-1 \tag{11}$$

A system to rotate a beam with the transfer matrix (3), can be constructed from two sets of five quadrupoles, with each set having the same drift length and quadrupole strength. In the first set, the quadrupoles are tilted by an angle $\phi_r/2+\pi/4$ around the longitudinal axis, where ϕ_r is the desired rotation angle in the beam; in the second set, the quadrupoles are tilted by an angle $-\pi/4$. To change the beam rotation angle requires changing the tilt angle of the first 5 quadrupoles: this may be done either mechanically or by constructing each magnet so as to resemble octupole magnets but with the current in the coils arranged to allow an arbitrary superposition of normal and skew quadrupole fields. A rotation of the field is then achieved by changing the ratio of normal to skew quadrupole field strengths.

An example of a rotation system has $L_A=0.35\ m$, $\mu=\pi/2$ and $\beta=1\ m$, the overall rotational beamline length is approximately 5 m and the maximum quadrupole strength is 2.53 m^{-1}. In practice, the length of the beamline is likely to increase when physical lengths are used for quadrupoles. Since there is no drift on either side of the set of five quadrupoles, the adjacent quadrupoles in the first and second sets may be combined into a single quadrupole.

DISCUSSION

Initial trials of the rotation system have been unsuccessful. The first issue concerns the total length of the rotation beamline. If the radiation diffracts too much between undulator modules, the interaction between the electrons and the radiation field is diminished and the Gaussian mode is not suppressed. This may not be a significant concern when the radiation wavelength is short and diffraction is low. There are also practical concerns due to the added length of the FEL, as the undulator line more than doubles in length due to the added shifts.

The second issue arising comes from the change in the longitudinal phase (z) position for different electrons. Variations in the transverse components of momentum change the z component of momentum p_z. Since the electrons will have different transverse momentum, depending on their distance from the beam radius, this causes a different longitudinal momentum variation for different electrons and leads to a debunching of the electron beam. Further work will examine if this debunching effect can be reduced.

CONCLUSION

The feasibility of generating light with OAM in a FEL from amplified shot noise in an electron beam is investigated. Trials in which a rotation of the electron beam is used to manipulate the relative phases between the electrons and the different OAM modes showed that suppressing a Gaussian mode will allow growth in the higher order $|l|=1$ modes. However, although physical realisation of the transform matrix (3) has been demonstrated, the resulting transverse momentum changes debunched the electron beam. Further work is needed to design a system which could be implemented.

ACKNOWLEDGEMENTS

We gratefully acknowledge the support of STFC's ASTeC department for HPC access. Using the STFC Hartree Centre; The Science and Technology Facilities Council Agreement Number 4163192 Release #3; and the John von Neumann Institutefor Computing (NIC) on JUROPA at Jülich Supercomputing Centre (JSC), under project HHH20.

ISBN: 978-3-95450-210-3 doi:10.18429/JACoW-FEL2019-TUP072

REFERENCES

[1] A. M. Yao and M. J. Padgett, "Orbital angular momentum: origins, behavior and applications," *Adv. Opt. Photon.*, vol. 3, no. 2, pp. 161-204, 2011. doi:10.1364/AOP.3.000161

[2] P. R. Ribič *et al.*, "Extreme-ultraviolet vortices from a free-electron laser," *Phys. Rev. X.*, vol. 7, no. 3, p. 031036, 2017. doi:10.1103/PhysRevX.7.031036

[3] E. Hemsing *et al.*, "Helical electron-beam microbunching by harmonic coupling in a helical un-dulator," *Phys. Rev. Lett.*, vol. 102, no. 17, p. 174801, 2009. doi:10.1103/PhysRevLett.102.174801

[4] E. Hemsing, A. Gover, and J. Rosenzweig, "Virtual dielectric waveguide mode description of a high-gain free-electron laser.ii. modeling and numerical simulations," *Phys. Rev. A.*, vol. 77, no. 6, p. 063831, 2008. doi:10.1103/PhysRevA.77.063831

[5] B. W. J. McNeil, M. W. Poole, and G. R. M. Robb, "Inducing Strong Density Modulation with Small Energy Dispersion in Particle Beams and the Harmonic Amplifier Free Electron Laser", in *Proc. PAC'05*, Knoxville, TN, USA, May 2005, paper RPPT021, pp. 1718–1720.

[6] L. Campbell and B. McNeil, "Puffin: A three dimensional,unaveraged free electron laser simulation code," *Phys. Plasmas*, vol. 19, no. 9, p. 093119, 2012. doi:10.1063/1.4752743

[7] E. Hemsing, A. Marinelli, and J. Rosenzweig, "Generatingoptical orbital angular momentum in a high-gain free-electronlaser at the first harmonic," *Phys. Rev. Lett.*, vol. 106, no. 16, p. 164803, 2011. doi:10.1103/PhysRevLett.106.164803

[8] R. Talman, "A proposed möbius accelerator," *Phys. Rev. Lett.*, vol. 74, no. 9, p. 1590, 1995. doi:10.1103/PhysRevLett.74.1590

FAST TRACK COMMUNICATION • OPEN ACCESS

Free electron laser generation of x-ray Poincaré beams

New Journal of Physics
The open access journal at the forefront of physics

Deutsche Physikalische Gesellschaft DPG
IOP Institute of Physics

Published in partnership with: Deutsche Physikalische Gesellschaft and the Institute of Physics

OPEN ACCESS

RECEIVED
24 March 2020

REVISED
13 May 2020

ACCEPTED FOR PUBLICATION
1 June 2020

PUBLISHED
21 July 2020

FAST TRACK COMMUNICATION

Free electron laser generation of x-ray Poincaré beams

Jenny Morgan[1,2,5], Erik Hemsing[3], Brian W J McNeil[1,2,4] and Alison Yao[1]

[1] University of Strathclyde (SUPA), Glasgow G4 0NG, United Kingdom
[2] Cockcroft Institute, Warrington, WA4 4AD, United Kingdom
[3] SLAC National Accelerator Laboratory, Menlo Park, California 94025, United States of America
[4] ASTeC, STFC Daresbury Laboratory, Warrington, WA4 4AD, United Kingdom
[5] Author to whom any correspondence should be addressed.

E-mail: jenny.morgan@strath.ac.uk

Keywords: free electron lasers, fully structured light, Poincaré beams

Abstract

An optics-free method is proposed to generate x-ray radiation with spatially variant states of polarization via an afterburner extension to a free electron laser. Control of the polarization in the transverse plane is obtained through the overlap of different coherent transverse light distributions radiated from a bunched electron beam in two consecutive orthogonally polarised undulators. Different transverse profiles are obtained by emitting at a higher harmonic in one or both of the undulators. This method enables the generation of beams structured in their intensity, phase, and polarization—so-called Poincaré beams—at high powers with tunable wavelengths. Simulations are used to demonstrate the generation of two different classes of light with spatially inhomogeneous polarization—cylindrical vector beams and full Poincaré beams.

1. Introduction

Polarization is important when considering light's interaction with matter. The majority of past research has concentrated on light with polarization which does not vary with transverse spatial coordinate, such as linear, elliptical or circular polarization. However, there has been growing interest in vector, or fully structured light (FSL) beams with spatially-varying polarization states [1–3] which can have additional, beneficial properties for a number of applications. For example, beams with radially orientated linear polarization can be focused more tightly than those with spatially homogeneous linear polarization, with applications in laser machining, optical nano-probing, and nano-lithography [1, 4, 5]. Beams with transversely structured polarization have also been shown to propagate more stably in self-focussing nonlinear media [6]. In general, the ability to control both the intensity and the polarization of FSL beams may provide a useful method for applications in material processing [7], microscopy [8], and in atomic state preparation, manipulation and detection [9, 10]. In this paper, a relatively simple method to generate tunable FSL into the x-ray using free electron lasers (FEL) [11] is described, opening up new, unexplored areas of atomic and molecular science. One such area is in the field of mirror image chiral molecules, either left or right handed, also called enantiomers. When subjected to FSL, a discriminatory optical force in opposite directions can result for each enantiomer [12].

In the simplest form, FSL beams can be described by a vector superposition of two orthogonally polarised spatial eigenmodes:

$$\boldsymbol{E}(\boldsymbol{r},\phi) = E_1(\boldsymbol{r},\phi)\hat{\boldsymbol{e}}_1 + \mathrm{e}^{\mathrm{i}\beta}E_2(\boldsymbol{r},\phi)\hat{\boldsymbol{e}}_2 \tag{1}$$

where β is the phase between the two modes and $\hat{\boldsymbol{e}}_1$ and $\hat{\boldsymbol{e}}_2$ are orthogonal polarization vectors. For cylindrically symmetric beams, a Laguerre–Gaussian (LG) set of spatial eigenmodes and circular polarization basis is adopted, where $\hat{\boldsymbol{e}}_1 = \hat{\mathbf{e}}_\mathrm{L} = (\hat{\boldsymbol{e}}_x + \mathrm{i}\hat{\boldsymbol{e}}_y)/\sqrt{2}$ and $\hat{\boldsymbol{e}}_2 = \hat{\mathbf{e}}_\mathrm{R} = (\hat{\boldsymbol{e}}_x - \mathrm{i}\hat{\boldsymbol{e}}_y)/\sqrt{2}$ correspond to left and right-handed circular polarization vectors, respectively. The resultant spatial distribution of the polarization is controlled by the superposition of the eigenmodes:

$$E_1(\boldsymbol{r},\phi) = \epsilon_\mathrm{L} LG_{p\mathrm{L}}^{\ell_\mathrm{L}}; \quad E_2(\boldsymbol{r},\phi) = \epsilon_\mathrm{R} LG_{p\mathrm{R}}^{\ell_\mathrm{R}} \tag{2}$$

where $\epsilon_{\rm L}$ and $\epsilon_{\rm R}$ are the field mode amplitudes, p is the radial index, and ℓ is the orbital angular momentum (OAM) index of the mode [13]. Taking the modes at the beam waist w_0 and assuming $p = 0$, the LG modes may be written as [14]:

$$LG_0^{\ell}(\boldsymbol{r}, \phi) = \sqrt{\frac{2}{\pi w_0^2 |\ell|!}} \left(\frac{\sqrt{2}r}{w_0}\right)^{|\ell|} \exp\left(-\frac{r^2}{w_0^2} + \mathrm{i}\ell\phi\right), \tag{3}$$

where: $r = \sqrt{x^2 + y^2}$ is the radial coordinate, and $\phi = \tan^{-1}(y/x)$ is the azimuthal coordinate.

If either E_1 or E_2 is zero, then the resultant beam is an LG mode with spatially uniform circular polarization. If the two modes have equal amplitudes and the same OAM ($\ell_{\rm L} = \ell_{\rm R}$), the resultant beam will have spatially uniform linear polarization. If they have equal amplitudes and equal but opposite OAM ($\ell_{\rm L} = -\ell_{\rm R}$), however, the resultant cylindrical vector (CV) beam [1, 3] will have an azimuthally varying linear polarization distribution that may be radial, azimuthal or spiral, depending on the phase difference β. If the two modes have different magnitudes of OAM the resultant 'full Poincaré' beam will carry a net OAM and the polarization will vary in both the azimuthal and radial coordinates and may contain all states of polarization: linear; elliptical; and circular [2]. Typical examples are the so-called 'lemon' and 'star' beams [15]. Note that for beams with Cartesian symmetry, the profiles may be better expressed in as Hermite–Gaussian (HG) modes [16] and with linear polarization vectors $\hat{\boldsymbol{e}}_1 = \hat{\boldsymbol{e}}_x$, $\hat{\boldsymbol{e}}_2 = \hat{\boldsymbol{e}}_y$.

The generation of such beams commonly relies upon methods that use external conversion optics to superimpose orthogonally-polarised transverse modes, including interferometric techniques [17, 18], q-plates [6, 19], and liquid crystal spatial light modulators [20]. While earlier works have produced OAM vortex beams in the x-ray [21, 22], there are, as yet, insufficient optical methods to superimpose OAM beams to generate the Poincare' x-ray beams described here. CV beams have been demonstrated in the ultraviolet using higher harmonic generation [23].

2. Generation of Poincaré beams using a free electron laser

In this paper, a new FEL method for generating bright, tunable, coherent Poincaré beams is proposed without the need for any external conversion optics. This optics-free method allows the extension of Poincaré beam generation into the x-ray regime for the first time. It is shown that by combining techniques of polarization and transverse mode shaping with FEL 'afterburners', coherent harmonic emission processes can be used to generate several classes of Poincaré beams—including radially polarized CV beams and 'star' Poincaré beams—with minimal changes to the overall facility layout. This approach enables the generation of wavelength-tunable, narrowband x-ray FSL beams in modern FEL facilities providing, for example, high resolution spectroscopy or scanning over narrow atomic/molecular resonances with structured light pulses.

FELs use highly relativistic electron beams (e-beams) propagating through undulating magnetic fields (undulators) to generate intense, tunable pulses of light. The wavelength range of FELs is broad and easily tunable, with current shorter wavelength facilities operating from the VUV down to hard x-rays [24–29]. The radiation output is typically a transverse Gaussian mode with nearly full transverse coherence and a spatially homogeneous polarization that is determined by the magnetic undulator fields (planar, helical, or elliptical). Polarization control is thus enabled by undulators with tunable polarity (e.g. [30–32]), or by a short tunable undulator section placed immediately downstream. This 'afterburner' undulator uses an FEL e-beam that has a strong coherent bunching from the previous lasing stage to generate coherent light with a high degree of adjustable polarization [33]. The primary FEL radiation pulse energy can also be strongly suppressed (but the e-beam bunching preserved) by using an undulator with reverse-tapering [34] and by e-beam steering [35], so that only the radiation pulse generated in the afterburner is delivered to experiments.

Currently, such schemes rely on transverse Gaussian afterburner emission at the first harmonic in which the e-beam bunching wavelength, $\lambda_{\rm b}$, matches the fundamental afterburner radiation wavelength resonance, $\lambda_{\rm b} = \lambda_{\rm r} = \lambda_{\rm u}(1 + K^2)/2\gamma^2$, where $\lambda_{\rm u}$ is the afterburner period, K is its rms undulator parameter, and γ is the e-beam relativistic factor. By radiating at harmonics however, where $\lambda_{\rm b} = \lambda_{\rm r}/h$ with $h > 1$ an integer, the transverse mode properties of the afterburner emission can be tailored to enable the generation of FSL beams. For example, in helical undulators that generate circularly polarized light, the coherent emission at harmonics is well-characterized by an LG mode with a helical phase and OAM index $\ell = \mp(h - 1)$ [36]. Both the sign of ℓ and the circular polarization vector $(\hat{\boldsymbol{e}}_x \mp \mathrm{i}\hat{\boldsymbol{e}}_y)/\sqrt{2}$ of the radiation are determined by the direction of the e-beam trajectory and therefore on the left $(-)$ or right $(+)$ handedness of the undulator. For planar undulators, the emission is linearly polarised, and the harmonic intensity profiles resemble an HG mode basis set.

Here, we propose extending this concept to two consecutive orthogonally polarised afterburners, individually adjustable in their strength, polarization, and relative phase. The two radiation pulses emitted from each of the two undulators overlap spatially and temporally. Previous versions of this crossed undulator setup have experimentally demonstrated polarization control at the fundamental [37, 38]. In the method described here, the electrons emit higher-order transverse modes at the second harmonic in one or both of the afterburners. This results in an FSL beam with an output field described by the superpostion of modes, as in equation (1). The phase difference, β, between the two modes can also be controlled by using a small magnetic phase-shifter between the two afterburners. This also allows phase-shifts due to the slippage between modules to be compensated, or the polarization pattern to be modified or rotated. Such a setup can be constructed from two Delta-type (or Apple-II) afterburner undulators [39, 40], provided that they have sufficient adjustment of their K parameters to access harmonics—extending the practicality of these undulators to enable transverse polarization control.

3. Simulations results

The FEL simulation code Puffin [41] is used to model the setup shown in figure 1. In contrast to most other FEL codes, Puffin does not average the electron motion over an undulator period, allowing modeling of both planar and helical harmonic emission arising from electron motion at the sub-undulator period scale. The setup is modeled using parameters based on the LCLS-II project at SLAC [42], with electron beam energy 4 GeV, peak current $I_0 = 1$ kA, and beam radius $\sigma_x = 26\,\mu$m. The undulator period is $\lambda_u = 3.9$ cm and each afterburner section has $N_u = 20$ undulator periods.

Time-independent (steady-state) simulations were used to demonstrate the method. This mode does not model the full temporal duration of the electron beam. However, as demonstrated in other crossed undulator methods, temporal pulse effects should not significantly affect the results, as the bunching factor on entering the afterburners is orders of magnitude larger than any beam shot-noise, and the relative slippage between electrons and radiation pulses is less than the coherence length [43]. The electrons are first pre-bunched in a reverse-tapered FEL section with $\lambda_b = 1.25$ nm. This achieves a bunching factor $|b| = 0.45$, while also reducing the FEL output power to 1 MW, three orders of magnitude lower than without the undulator taper. The process for pre-bunching electrons in a reverse tapered undulator has been described previously [34]. The electron beam bunching process does not differ significantly from the standard FEL process with the exception of the reduced radiation power. Steering the e-beam to further reduce the contribution from the background power is not modeled [35], and the radiation generated in the FEL section is simply removed. The pre-bunched beam then enters the afterburner Delta undulators, which can be adjusted for linear or circular polarization and tuned so that the electron bunching is at either the fundamental or second harmonic. Three polarization distributions that generate FSL beams are now presented using this setup.

3.1. Vector beams

In the first example, a pair of cross-polarized planar afterburners is simulated. They are both tuned to a fundamental resonance of $\lambda_r = 2.5$ nm, so that the e-beam is bunched and radiates at the second harmonic, generating the field $\boldsymbol{E}(\boldsymbol{r}, \phi) = \epsilon_1 \mathrm{HG}_{10}\hat{\boldsymbol{e}}_{\boldsymbol{x}} + \mathrm{e}^{\mathrm{i}\beta}\epsilon_2 \mathrm{HG}_{01}\hat{\boldsymbol{e}}_{\boldsymbol{y}}$. With $\epsilon_1 = \epsilon_2$, this superposition is seen in figure 2 to create an annular intensity profile with a radial polarization distribution for $\beta = 0$. The polarization map was constructed by calculating the Stokes parameters:

$$\begin{aligned} S_0 &= |E_x|^2 + |E_y|^2 = |E_R|^2 + |E_L|^2, \\ S_1 &= |E_x|^2 - |E_y|^2 = 2\ \mathrm{Re}(E_R^* E_L), \\ S_2 &= 2\ \mathrm{Re}(E_x^* E_y) = 2\ \mathrm{Im}(E_R^* E_L), \\ S_3 &= 2\ \mathrm{Im}(E_x^* E_y) = |E_R|^2 - |E_L|^2, \end{aligned} \tag{4}$$

where the subscripts denote the appropriate linear or circular field components [44]. S_0 is the parameter describing temporal intensity. The linear horizontal/vertical, diagonal linear, and circular polarization are described by S_1, S_2, and S_3, respectively.

The ellipticity, χ, and the orientation, ψ, of a polarization ellipse at each point on the transverse plane can then be calculated [45], where:

$$\chi = \frac{1}{2}\sin^{-1}\left(\frac{S_3}{S_0}\right), \quad \psi = \frac{1}{2}\tan^{-1}\left(\frac{S_2}{S_1}\right). \tag{5}$$

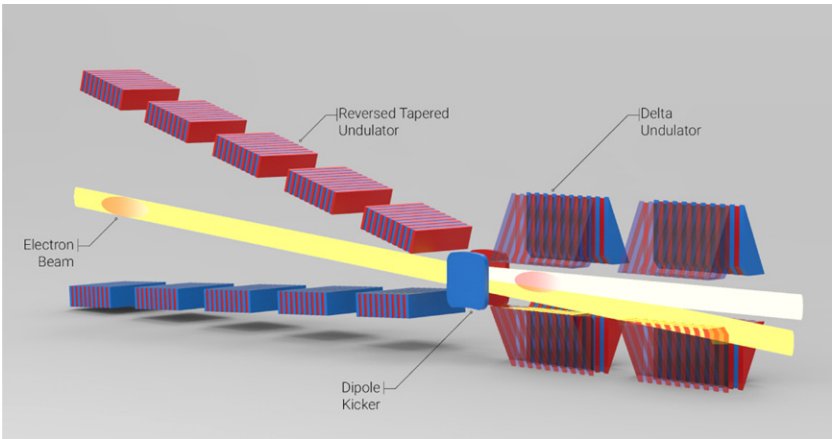

Figure 1. Schematic of the method. A relativistic electron beam is initially bunched using a reverse-tapered undulator. This suppresses the generation of the linearly polarised radiation. A dipole kicker (or off-axis quadrupole lattice) then redirects the electron beam into two Delta undulators tuned so that the electron bunching is at an harmonic of their fundamental resonant wavelength. The Delta undulators can then be adjusted for different polarizations and tuning to generate light with transversely inhomogeneous polarization—fully structured light.

The polarization ellipses are then plotted at various points across the intensity profile. The normalised stokes vector capturing the spatial polarization for these crossed planar harmonic undulators can be written as,

$$\boldsymbol{s} = \frac{1}{S_0}\begin{pmatrix} S_1 \\ S_2 \\ S_3 \end{pmatrix} = \begin{pmatrix} \cos(2\phi) \\ \cos(\beta)\sin(2\phi) \\ \sin(\beta)\sin(2\phi) \end{pmatrix}. \tag{6}$$

Note that for $\beta \neq 0$, the polarization distribution can also contain circular components.

Similarly, with crossed helical undulators tuned so that the bunching is at the second harmonic, one obtains $\ell_{\mathrm{R}} = -1$ and $\ell_{\mathrm{L}} = 1$. If the undulators are the same length and the bunching factor does not change significantly between them, the modes have equal amplitude, $\epsilon_{\mathrm{L}} = \epsilon_{\mathrm{R}}$. We then obtain,

$$\boldsymbol{s} = \begin{pmatrix} \cos(\beta - 2\phi) \\ \sin(\beta - 2\phi) \\ 0 \end{pmatrix}. \tag{7}$$

The S_3 parameter vanishes, so the beam has only linear polarization states which vary with ϕ. The generated vector 'vortex beam' is also shown in figure 2.

We note that, in order for this description to accurately model the final FSL output, the radiation emitted in each undulator should be well-described by a pure modes. In reference [46], it was shown that with sufficiently large K and periods N_{u} in a helical afterburner, coherent radiation from a pre-bunched e-beam is well approximated by an LG mode in the limit that the e-beam radius satisfies $\sigma_x > \gamma_z\sqrt{N_{\mathrm{u}}}/k$, such that the emission angles are dominated by the e-beam and not the undulator emission. The undulators must also be kept relatively short to reduce the diffraction of the radiation so that the the transverse sizes of the modes do not significantly differ.

It is seen from figure 2 that CV beams are generated when the orthogonal afterburners both radiate at the second harmonic. Due to the relationship between the polarization and the transverse modes, only certain CV polarization distributions are available using this setup. For example, the second harmonic emission does not produce y-polarised HG_{10} modes, or $\ell_{\mathrm{L}} = -1$ modes with left-circular polarization (i.e., no 'lemon' beams) [47, 48].

The power of the final radiation pulses in figure 2 is of the order of 0.3 MW, which is consistent with the second harmonic power calculated in [46]. For a single helical afterburner the radiated coherent power is

$$P = 4P_b b^2 \frac{I_0}{\gamma I_A}\left(\frac{K^2}{1+K^2}\right)^2 \ln\left(\frac{1+4N^2}{4N^2}\right) \tag{8}$$

where P_b is the peak e-beam power, $I_A = 17$ kA is the Alfven current, and $N = k\sigma_x^2/L_{\mathrm{u}}$ is the Fresnel number of the e-beam with $k = 2\pi/\lambda_b$, and $L_{\mathrm{u}} = N_{\mathrm{u}}\lambda_{\mathrm{u}}$ the length of the undulator. This power is the same magnitude as the radiation emitted at the fundamental of the upstream reverse-tapered FEL, highlighting the need to steer the pre-bunched electron beam to avoid overlap with the radiation emitted during

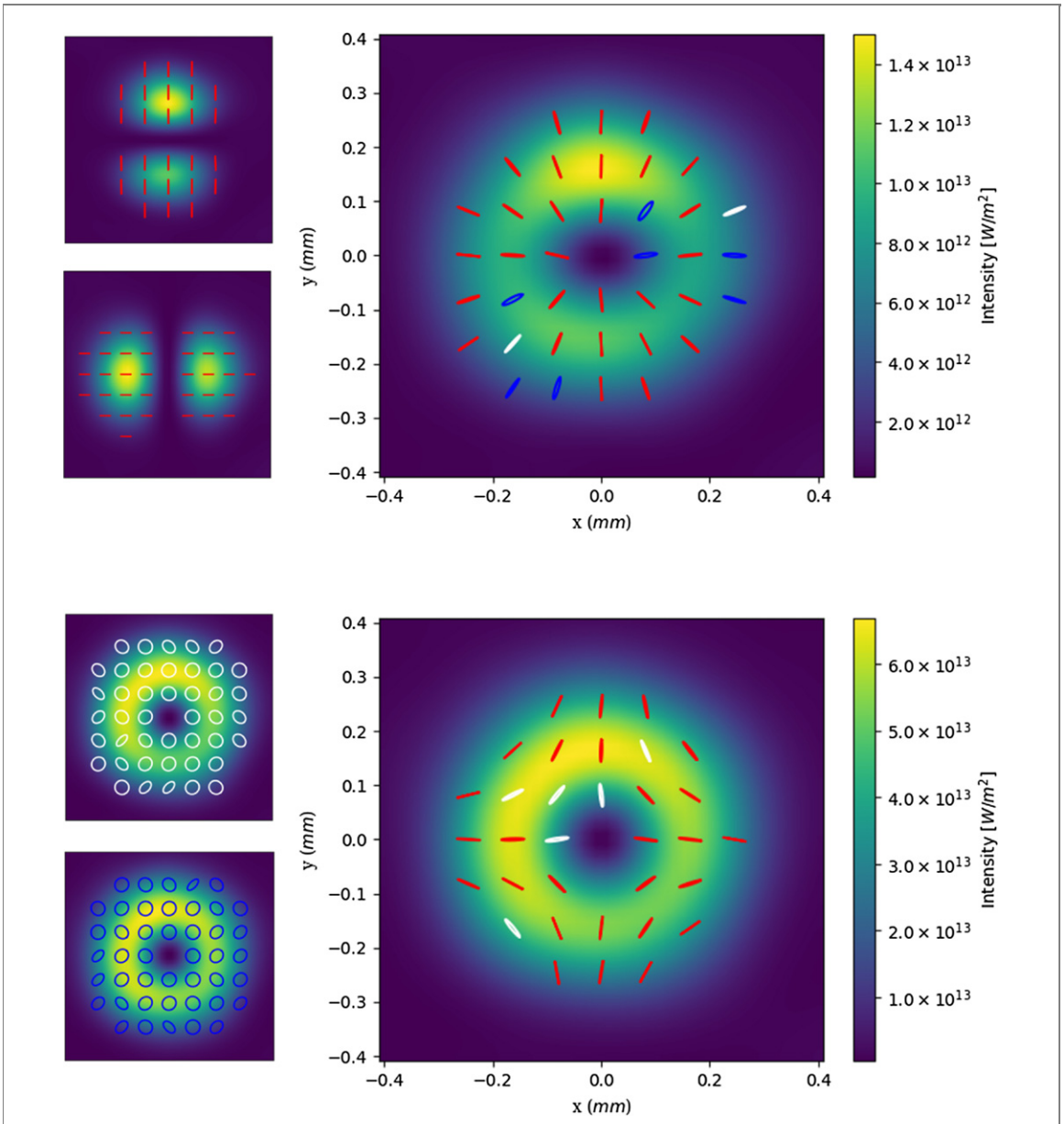

Figure 2. Simulation of cylindrical vector polarizations. The electrons are bunched at the second harmonic of the Delta undulators to give orthogonal linear (top) and circular (bottom) polarization. The radiation polarization emitted from each Delta undulator is plotted schematically on the (left) two plots and the combined field simulated from both undulators on the (right) plot. Red, blue and white lines correspond to linear, right-circular and left-circular polarization respectively.

pre-bunching. We note from equation (8) that with strong focusing to reduce $\sigma_x < 26\,\mu$m, the power output can be greatly improved. As the electrons are bunched before the afterburner, the short undulators needed to account for diffraction still provide high powers, although the power scaling for a single undulator favors small N. If a longer afterburner section is desirable, or if required parameters lead to greater diffraction, one solution is to split the first Delta undulator into two sections and sandwich the second Delta undulator between these two sections. This leads to better overlap of the two polarised beams.

3.2. Full Poincaré beams

The second class of light with spatially inhomogeneous polarization considered is full Poincaré beams created from a superposition of $\mathrm{LG}_0^{\pm 1}$ and LG_0^0 (Gaussian) radiation with orthogonal circular polarizations. From equation (2), the Stokes vector then becomes,

$$\boldsymbol{s} = \begin{pmatrix} \dfrac{2\sqrt{2}rw_0}{2r^2 + w_0^2}\ \cos(\beta - \phi) \\ \dfrac{2\sqrt{2}rw_0}{2r^2 + w_0^2}\ \sin(\beta - \phi) \\ \pm\dfrac{2r^2 - w_0^2}{2r^2 + w_0^2} \end{pmatrix}, \tag{9}$$

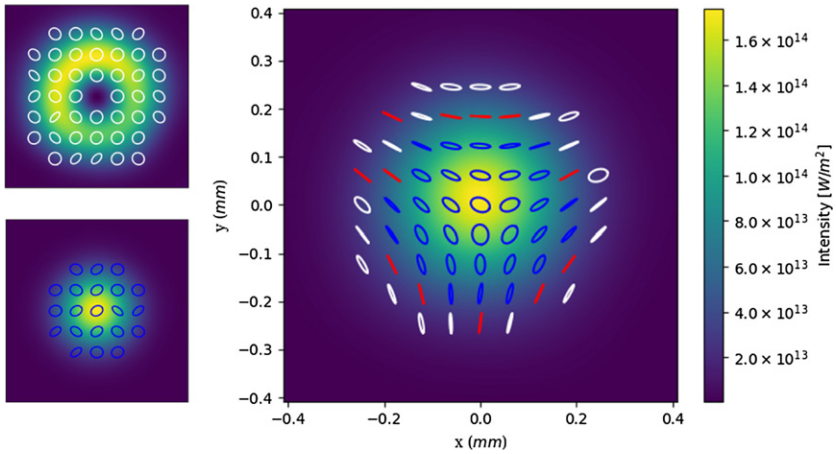

Figure 3. Poincaré polarization distribution downstream of the afterburner. The Delta undulators are set to have orthogonal circular polarizations. The electrons are bunched at the second harmonic of the first undulator and the fundamental of the second undulator. The radiation emitted in each Delta undulator is plotted (left) along with the combined field from both undulators (right).

where the + and − signs correspond to $(\ell_L, \ell_R) = (1, 0)$ and $(\ell_L, \ell_R) = (0, -1)$, respectively. On axis, $r = 0$, the polarization is purely circular while the at the radius $r = w_0/\sqrt{2}$, the polarization is purely linear, with orientation depending on ϕ. Figure 3 shows the 'star' Poincaré beam output generated in the $(\ell_L, \ell_R) = (1, 0)$ case. To achieve this combination, the second undulator is tuned so that its fundamental resonance matches the bunching wavelength at $\lambda_r = 1.25$ nm and the radiation emitted is Gaussian. The first undulator is tuned to $\lambda_r = 2.5$ nm, radiating at the second harmonic as before. The electrons radiate with higher power at the fundamental than at the second harmonic. To compensate and balance the powers between the two radiation beams, the Delta undulator emitting at the fundamental is detuned from resonance to reduce its power output. Detuning the undulator will affect the mode size and therefore polarization structure. Specific undulator detuning is a topic for future studies and will depend on the specific application.

4. Conclusion

The three x-ray polarization topologies demonstrated here are not the full range of pulses available with the two Delta undulator arrangement. In addition to varying the polarization and undulator resonance, other factors can change the polarization distribution. Both the phase and power ratio between the different transverse modes can be adjusted which, for example, could be used to create elliptical vector beams. Slightly detuning the resonance of one undulator will push the radiation further off axis, which can be used to control the mode overlap [37]. Finally, radiating at even higher harmonics of a helical undulator will generate the higher order LG modes producing yet more variants, though the power drops with increasing harmonic number [46].

We note that this method can generate Poincaré beams at any operational wavelength of an FEL facility. The advantage of the afterburner configuration is that it is both simple and cost effective to implement as the afterburners can be added to existing FEL facilities, or may already exist as the last couple undulator sections. Furthermore, the method could be combined with other methods. For example, consideration of temporal or short pulse effects can be envisaged that alter the FSL in the temporal domain (e.g., [49]) adding a further dimension for potential experimental exploitation.

Acknowledgments

We are grateful to funding from the Science and Technology Facilities Council (Agreement Number 4163192 Release#3); ARCHIEWeSt HPC, EPSRC Grant EP/K000586/1; EPSRC Grant EP/M011607/1; John von Neumann Institute for Computing (NIC) on JUROPA at Jülich Supercomputing Center (JSC), project HHH20. EH was supported by U.S. Department of Energy Contract No. DE-AC02-76SF00515 and Award No. 2017-SLAC-100382.

ORCID iDs

Brian W J McNeil https://orcid.org/0000-0002-7267-611X

References

[1] Zhan Q 2009 *Adv. Opt. Photon.* **1** 1–57
[2] Beckley A M, Brown T G and Alonso M A 2010 *Opt. Express* **18** 10777–85
[3] Galvez E J, Khadka S, Schubert W H and Nomoto S 2012 *Appl. Opt.* **51** 2925–34
[4] Dorn R, Quabis S and Leuchs G 2003 *Phys. Rev. Lett.* **91** 233901
[5] Rubinsztein-Dunlop H *et al* 2016 *J. Opt.* **19** 013001
[6] Bouchard F, Larocque H, Yao A M, Travis C, De Leon I, Rubano A, Karimi E, Oppo G L and Boyd R W 2016 *Phys. Rev. Lett.* **117** 233903
[7] Nesterov A V and Niziev V G 2000 *J. Phys. D: Appl. Phys.* **33** 1817–22
[8] Hao X, Kuang C, Wang T and Liu X 2010 *J. Opt.* **12** 115707
[9] Sick B, Hecht B and Novotny L 2000 *Phys. Rev. Lett.* **85** 4482–5
[10] Novotny L, Beversluis M R, Youngworth K S and Brown T G 2001 *Phys. Rev. Lett.* **86** 5251–4
[11] McNeil B W J and Thompson N R 2010 *Nat. Photon.* **4** 814–21
[12] Cameron R P, Götte J B, Barnett S M and Yao A M 2017 *Phil. Trans. R. Soc.* A **375** 20150433
[13] Yao A M and Padgett M J 2011 *Adv. Opt. Photon.* **3** 161–204
[14] Barnett S M and Zambrini R 2007 *Quantum Imaging* ed K I Kobolov (Singapore: Springer)
[15] Nye J F 1983 *Proc. R. Soc.* A **389** 279
[16] Beijersbergen M, Allen L, van der Veen H and Woerdman J 1993 *Opt. Commun.* **96** 123–32
[17] Niziev V G, Chang R S and Nesterov A V 2006 *Appl. Opt.* **45** 8393–9
[18] Chen S, Zhou X, Liu Y, Ling X, Luo H and Wen S 2014 *Opt. Lett.* **39** 5274–6
[19] Cardano F, Karimi E, Marrucci L, de Lisio C and Santamato E 2013 *Opt. Express* **21** 8815–20
[20] Maurer C, Jesacher A, Fürhapter S, Bernet S and Ritsch-Marte M 2007 *New J. Phys.* **9** 78
[21] Peele A G, McMahon P J, Paterson D, Tran C Q, Mancuso A P, Nugent K A, Hayes J P, Harvey E, Lai B and McNulty I 2002 *Opt. Lett.* **27** 1752–4
[22] Peele A G, Nugent K A, Mancuso A P, Paterson D, McNulty I and Hayes J P 2004 *J. Opt. Soc. Am.* A **21** 1575–84
[23] Hernández-García C, Turpin A, Román J S, Picón A, Drevinskas R, Cerkauskaite A, Kazansky P G, Durfee C G and Sola I J 2017 *Optica* **4** 520–6
[24] Ackermann W *et al* 2007 *Nat. Photon.* **1** 336–42
[25] Emma P *et al* 2010 *Nat. Photon.* **4** 641
[26] Ishikawa T *et al* 2012 *Nat. Photon.* **6** 540–4
[27] Allaria E *et al* 2012 *Nat. Photon.* **6** 699–704
[28] Allaria E *et al* 2013 *Nat. Photon.* **7** 913
[29] Kang H S *et al* 2017 *Nat. Photon.* **11** 708–13
[30] Allaria E *et al* 2014 *Phys. Rev.* X **4** 041040
[31] Roussel E *et al* 2017 *Photonics* **4** 29
[32] Henderson J, Campbell L, Freund H and McNeil B 2016 *New J. Phys.* **18** 062003
[33] Lutman A *et al* 2016 *Nat Photon* **10** 468–72
[34] Schneidmiller E A and Yurkov M V 2013 *Phys. Rev. Spec. Top. Accel. Beams* **16** 110702
[35] MacArthur J P, Lutman A A, Krzywinski J and Huang Z 2018 *Phys. Rev.* X **8** 041036
[36] Sasaki S and McNulty I 2008 *Phys. Rev. Lett.* **100** 124801
[37] Ferrari E *et al* 2019 *Phys. Rev. Spec. Top. Accel. Beams* **22** 080701
[38] Deng H *et al* 2014 *Phys. Rev. Spec. Top. Accel. Beams* **17** 020704
[39] Sasaki S 1994 *Nucl. Instrum. Methods Phys. Res.* A **347** 83–6
[40] Temnykh A B 2008 *Phys. Rev. Spec. Top. Accel. Beams* **11** 120702
[41] Campbell L and McNeil B 2012 *Phys. Plasmas* **19** 093119
[42] Schoenlein R W 2015 *New Science Opportunities Enabled by LCLS-II X-ray Lasers Tech. Rep. SLAC-R-1053 SLAC* National Accelerator Laboratory
[43] Li Y, Faatz B and Pflüeger J 2010 3D polarization properties for crossed-planar undulators *DESY Print TESLA-FEL*
[44] Dennis M, O'Holleran K and Padgett M 2009 *Prog. Opt.* **53** 293–363
[45] Saleh B E A and Teich M C 2007 *Fundamentals of Photonics* (New York: Wiley)
[46] Hemsing E 2020 *Phys. Rev. Spec. Top. Accel. Beams* **23** 020703
[47] Afanasev A and Mikhailichenko A 2011 On generation of photons carrying orbital angular momentum in the helical undulator (arXiv:1109.1603)
[48] Katoh M, Fujimoto M, Kawaguchi H, Tsuchiya K, Ohmi K, Kaneyasu T, Taira Y, Hosaka M, Mochihashi A and Takashima Y 2017 *Phys. Rev. Lett.* **118** 094801
[49] Serkez S, Trebushinin A, Veremchuk M and Geloni G 2019 *Phys. Rev. Spec. Top. Accel. Beams* **22** 110705

Attosecond polarization modulation of x-ray radiation in a free-electron laser

J. Morgan*
University of Strathclyde (SUPA), Glasgow G4 0NG, United Kingdom and Cockcroft Institute, Warrington, WA4 4AD, United Kingdom

B. W. J. McNeil
University of Strathclyde (SUPA), Glasgow G4 0NG, United Kingdom; Cockcroft Institute, Warrington, WA4 4AD, United Kingdom; and ASTeC, STFC Daresbury Laboratory, Warrington, WA4 4AD, United Kingdom

(Received 18 August 2020; accepted 7 January 2021; published 14 January 2021)

A new method to generate short wavelength free-electron laser output with modulated polarization at attosecond timescales is presented. Simulations demonstrate polarization switching timescales that are four orders of magnitude faster than the current state of the art and, at x-ray wavelengths, approaching the atomic unit of time of approximately 24 attoseconds. Such polarization control has significant potential in the study of ultrafast atomic and molecular processes. The output alternates between either orthogonal linear or circularly polarized light without the need for any polarizing optical elements. This facilitates operation at the high brightness x-ray wavelengths associated with FELs. As the method uses an afterburner configuration it would be relatively easy to install at existing FEL facilities, greatly expanding their research capability.

DOI: 10.1103/PhysRevAccelBeams.24.010701

I. INTRODUCTION

The polarization of light is a fundamental property which affects its interactions with matter. These interactions are used experimentally to investigate various properties of matter such as the chirality of molecules and crystal structures [1,2]. Additionally, light's polarization is essential in the study of magnetism, for example, short polarized pulses can be used to manipulate magnetic moments and investigate the timescales of angular momentum exchange [3]. Current experiments can demand greater spatial [4] and/or temporal [5] control and flexibility of the polarization than the generation of purely circular, elliptical or linearly polarized light. In particular, fast temporal switching of light's polarization is desirable for techniques such as polarization modulation spectroscopy, notably, x-ray magnetic circular dichroism (XMCD) [6–8] and may offer control over material excitations including lattice vibrations [9], charge and spin [10,11].

Ultrafast switching of the polarization properties of light is a nontrivial task as conventional polarizing elements are quasistatic devices at ultra-fast timescales. While some conventional polarizing elements can be controlled by electric currents [12], these are limited by their electronic components to gigahertz switching speeds and also see large energy losses.

In the drive to further decrease switching rates, recent research using plasmonic technologies has further decreased linear polarization switching to 800 fs [13] and circular polarization switching to pico-second timescales [14]. However, these techniques are based on the active control of polarizing elements and operate primarily at visible wavelengths or longer. As wavelengths shorten beyond the ultraviolet, polarizing optics are more limited with modulation timescales being determined primarily by the light generation method.

In electron accelerator based light sources, which can generate light into the hard x-ray, it is the motion of the radiating electrons propagating through magnetic undulators that determines the polarization of the photon beam. For example, circular polarization modulation with a ~2 ns switching rate has been demonstrated in a synchrotron by controlling electron bunch orbits through twin undulators [15]. Methods of generating x-rays with temporally varying polarization from the output of free-electron lasers, FELs, include 100 fs switching using a chirped electron beam [16]. Femto-second isolated pulses with different polarization can be generated with the fresh slice method described in [17].

*jenny.morgan@strath.ac.uk

It can be envisaged that significant improvement on temporal polarization switching timescales to those comparable to atomic processes will enable experimental investigation of these processes. In XMCD, for example, the polarization switching rate of x-rays limits the observable processes to those occurring slower than the switching cycle [8]. In this paper, a method is described which could improve the polarization switching rate of both linear and circularly polarized high brightness x-rays toward the attosecond timescale regime and comparable to the period of a ground state electron in the Bohr hydrogen atom, the atomic unit of time ≈24 as. We speculate that pulses of such timescales could be used to develop novel methods, perhaps similar to XMCD, that can improve temporal resolutions to below that of the exchange interaction responsible for magnetic order [3].

The method modulates the polarization of light radiated from a free-electron laser. Trains of radiation pulses are generated in which each pulse alternates between orthogonal linear or circular polarization states. FELs are widely tuneable devices operating down to the hard x-ray wavelength range [18] and the method reported here should be applicable over this full range. Simulations are carried out here in the soft x-ray generating radiation pulse trains with alternate orthogonal polarization pulse timescales of tens of attoseconds.

II. FEL THEORY

In a high-gain FEL a relativistic electron beam propagates through magnetic undulators and emits electromagnetic radiation (light) with a resonant wavelength $\lambda_r = \lambda_u(1 + \bar{a}_u^2)/2\gamma_0^2$, where λ_u is the undulator period, $\bar{a}_u$ is the rms undulator parameter and γ_0 is the electron beam's relativistic factor. The light is amplified via a collective interaction which causes the electrons to micro-bunch at the resonant wavelength and to emit coherently [18]. The initial nonuniform phase distribution of electrons, or shot-noise, can provide the initial seed which is subsequently amplified in the process of self-amplified spontaneous emission, giving a temporally noisy output [19]. The relative propagation of a radiation wavefront through the electrons of one λ_r every λ_u, referred to as "slippage," allows interaction between different regions of the electron bunch and radiation pulse. This correlates the phase of the radiation output at a length determined by the cooperation length $l_c = \lambda_r/4\pi\rho$—the relative slippage in an exponential gain length through the undulator $l_g = \lambda_u/4\pi\rho$. Here ρ, the FEL parameter, determines the strength of the FEL interaction [19].

The FEL process generates high-power radiation with its polarization determined by the magnetic undulator field—either planar, elliptical or helical. A typical X-ray FEL facility uses planar undulators to micro-bunch the electrons. Polarization control can be enabled by adding additional undulators placed downstream of the main planar undulator amplification section once microbunching has been established [20]. Such additional downstream undulators, or "afterburners," are increasingly being explored as a method to tailor FEL output in many ways not limited to polarization control, e.g., short pulse generation [21,22] and transverse phase manipulation [23]. They provide solutions to enable specific experimental output requirements with minimal changes to an existing facility and therefore at relatively low cost.

III. POLARIZATION MODULATED PULSE TRAINS: METHOD

To generate FEL output with modulated polarization, we propose an afterburner design consisting of a series of few period, alternate orthogonally polarized undulator modules as shown in Fig. 1. The undulators are separated by electron delay chicanes which can introduce additional slippage between the electron bunch and the radiation field. Both of the orthogonal, polarized radiation fields emitted in the afterburner are mode-locked which creates trains of short pulses [21]. The orthogonally polarized pulse trains are shifted temporally with respect to each other so that the

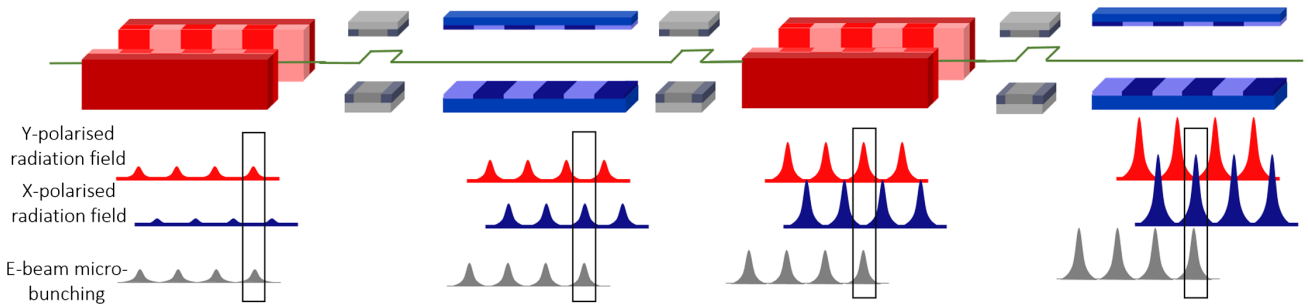

FIG. 1. Schematic layout of a section of afterburner used to generate a radiation pulse train with alternating x and y linear polarization. In each undulator, those regions of the electron beam with modulated microbunching emit coherently. Chicanes delay the electron beam between undulator modules so that those sections of high microbunching overlap with the appropriately polarized pulse for the undulator in which they are propagating.

combined pulse train consists of a series of alternate, orthogonally polarized pulses.

Mode-locking in a FEL, first proposed in [21] and compacted into a mode-locked afterburner configuration in [22], creates trains of short radiation pulses via a process analogous with mode-locking in conventional cavity lasers [24]. In the mode-locked afterburner, normal FEL amplification occurs first in an electron beam prepared with an energy modulation, $\gamma(t) = \gamma_0 + \gamma_m \cos(\omega_m t)$. This generates a periodic microbunching structure in the electron beam at the energy modulation period by creating higher FEL gain at the minima of the energy modulated beam. Chicane delays between the short undulator sections in the afterburner then map the electron beam microbunching comb onto the radiation modal pulses.

Here, a similar mapping of the microbunched comb to the mode-locked radiation generated in the orthogonally polarized afterburner modules is used to generate alternately polarized pulse trains. Figure 1 shows a schematic of how these pulse trains are generated in a planar undulator afterburner. Chicanes placed between undulator modules are chosen to delay the high microbunched regions of the electron beam to the polarized radiation pulses corresponding to the similarly polarized undulator in which they interact. The orthogonally polarized radiation pulses do not interact with the electrons in this undulator module so that they simply experience free propagation. The orthogonally polarized undulators then effectively behave as additional alternate chicane delays.

The combined slippage of the electrons with respect to a radiation wavefront between undulator modules of the same polarization should therefore be the modulation period λ_m. The temporal separation of the pulses of radiation with the same polarization is then $T = \lambda_m/c$ and the relative times of these pulses are

$$t_1 = nT. \tag{1}$$

The orthogonally polarized pulses will then have pulse peaks at relative times:

$$t_2 = t_0 + t_1 + \Delta T \tag{2}$$

where $\Delta T = s/c$ is the time for the radiation to propagate the slippage length, $s = \lambda_m/2$, through the electron bunch. t_0 is a constant which may shift the radiation pulse trains relative to each other. This relative shift is achieved by adjusting the slippage between consecutive orthogonally polarized undulators to be $s + ct_0$ and $s - ct_0$. Here, we chose $t_0 = 0$ representing the case where we have equal slippage between undulator modules and therefore there is equal spacing between all pulses.

IV. SIMULATIONS

The method is modeled using the FEL simulation code PUFFIN [25] using the parameters based on the LCLS-II project at SLAC [26] as listed in Table I. Dispersion effects within the chicanes are included in the model although chicanes which reduce dispersion and dispersionless chicanes are being developed [27,28].

A. Alternating linear polarization

The method is first demonstrated using an afterburner with alternating x and y planar undulators that will emit correspondingly linearly polarized light. An electron beam, with a Gaussian current profile, is first prepared with a sinusoidal energy modulation of period $\lambda_m = 40\ \text{nm} = 32\lambda_r$. This is applied via the initial conditions of the beam before any FEL interaction is simulated. Start to end simulations with full modeling of the energy modulation is left for future work. However, pre-modulation at longer wavelengths is relatively straightforward and similar modulation as presented here for a nonideal electron beam has previously been demonstrated [29,30].

As with the mode-locked afterburner of [22], the electron microbunching comb is then developed in a SASE FEL "preamplifier." The simulation modeled an x-polarized undulator similar to that found at most current FEL facilities. The power growth in this preamplifier stage is inhibited by the electron beam energy modulation. On subsequent injection into the afterburner, the power growth in the pulsed regions becomes exponential due to their overlap with the high quality electron beam regions being maintained. There is therefore much greater radiation power generated in the afterburner than in the preamplifier. The point at which the electron beam is extracted from the preamplifier—after 900 undulator periods—is chosen so that the radiation is two orders of magnitude smaller than

TABLE I. Simulation parameters.

Parameter	Value
Electron beam energy [GeV]	4
Peak current, I_0 [kA]	1
rms energy spread σ_γ/γ	1.25×10^{-4}
Normalized emittance [mm-mrad]	0.45
rms beam size σ_x [μm]	26
Undulator period λ_u [cm]	3.9
Resonant wavelength λ_r [nm]	1.25
Modulation wavelength λ_m [nm]	40.0
Modulation amplitude γ_m/γ_0	1.2×10^{-3}
rms undulator parameter $\bar{a}_u$	1.72
ρ parameter	1.2×10^{-3}
Afterburner	
Number of undulator periods per module	8
Chicane Delays [nm]	10
Number of undulator modules	36

the final saturated radiation power in the following afterburner.

Both the x and orthogonal y polarized undulator modules in the afterburner are 8 periods long, each separated by a chicane that delays the electrons by a further 8 resonant wavelengths. The total electron delay is then $s = 16\lambda_r = \lambda_m/2$ between successive undulator modules and λ_m between undulators of the same polarization. This maintains overlap between the electron microbunching comb and the alternating orthogonally polarized radiation as shown in Fig. 1, leading to the amplification of radiation spikes. The orthogonal radiation spikes so generated should not interfere with each other due to their orthogonal polarization. However, as both fields are emitted by the same electron beam source, which sees only small changes between undulator modules, fluctuations in the power of one pulse train envelope should be similar to its orthogonal counterpart.

Figure 2 shows a section of the radiation power profiles and spectrum of the x and y polarized fields after 36 afterburner undulator modules (16 of each polarization). The additional slippage between undulator modules leads to a frequency spectrum that is broader than typical FEL output and discretized into frequency modes with modes spacing, $\Delta\omega_s$, as determined by the time taken for the radiation to travel the total slippage length between the same polarized undulators. The radiation pulse peaks arise from the constructive interference between the frequency modes whose phase has been fixed by the modulation, $\Delta\omega_m = \Delta\omega_s$. This is the principle of mode-locking as described in [21,24].

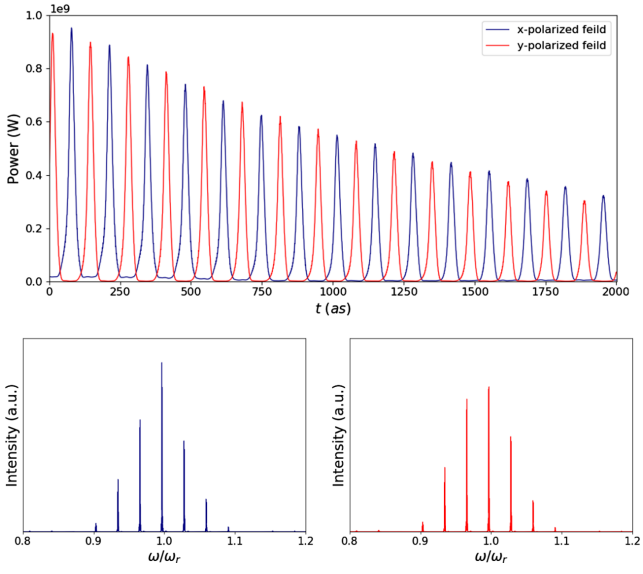

FIG. 2. Top: power vs relative time t for the x and y polarized fields and Bottom: the corresponding spectra after 36 undulator-chicane modules.

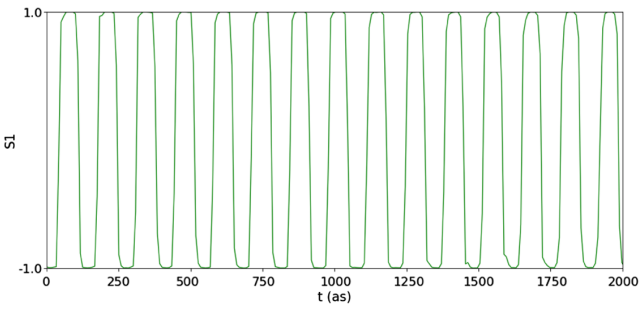

FIG. 3. The on-axis normalized Stokes parameter s_1 as a function of relative time t after 36 undulator-chicane modules. It is seen that s_1 flips between positive and negative values with extremes at $|s_1| \approx 1.0$, indicating high degree of polarization modulation.

As the undulator modules have equal lengths, both the x and y polarized fields have approximately the same pulse FWHM duration of $\tau_p \approx 19$ as and with peak powers of $P_{pk} \approx 1$ GW. The separation between each pulse is approximately 67 as corresponding to a polarization switching rate of 15 PHz.

A normalized Stokes parameter, s_1, is used to examine the degree of linear polarization in the pulses, where: $s_1 = (|E_x|^2 - |E_y|^2)/(|E_x|^2 + |E_y|^2)$ is the intensity difference between the x and y polarized fields normalized to the total intensity of the field. Values of $s_1 = \pm 1.0$ then indicate fully linear x or y polarization, respectively. This is plotted as a function of time in Fig. 3 where it is seen that the polarization is highly modulated, flipping between the two polarization states. The high degree of polarization contrast is seen at the peak powers, $|s_1| \approx 1.0$. Across the full pulse train, $|s_1| > 0.95$ at the peak powers, demonstrating a high degree of polarization modulation.

B. Alternating circular polarization

Pulses with polarization alternating between left and right-hand circular polarization have also been modeled. The amplifier section, which pre-bunches the electrons using SASE, remains an (x-polarized) planar undulator similar to that above. The afterburner now consists of orthogonal left and right circularly polarized helical undulators.

Figure 4 shows the power profiles for the left-hand circular, LCP, and right-hand circular, RCP, polarization. The pulses now alternate between orthogonal circular polarization with the same FWHM pulse duration τ_p and rate as the linearly polarized case above. The stokes parameter, $s_3 = (|E_R|^2 - |E_L|^2)/(|E_R|^2 + |E_L|^2)$, which gives the degree of circular polarization is plotted in Fig. 5. Across the pulse peaks, there is a high degree of circular polarization, $|s_3| > 0.9$. This is very promising as many ultrafast polarization switching techniques cannot achieve full-handedness reversal.

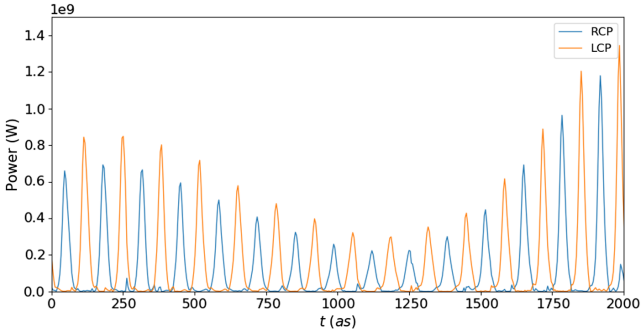

FIG. 4. Power spectrum for left and right hand polarization vs relative time at the end an afterburner with alternating polarized helical undulator modules.

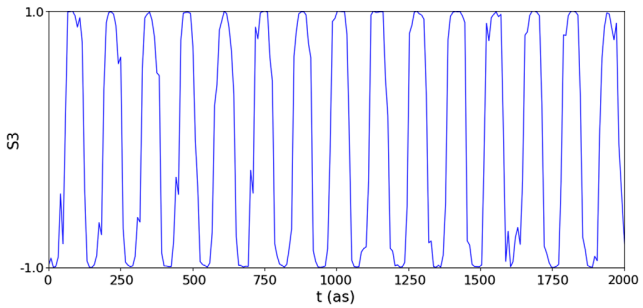

FIG. 5. The on-axis normalized Stokes parameter s_3 as a function of relative time t after 36 undulator-chicane modules. It is seen that s_3 flips between positive and negative values with extremes at $|s_3| \approx 1.0$, indicating high degree of polarization modulation.

V. CONCLUSIONS

This paper demonstrates a novel method to generate attosecond polarization modulation in a short wavelength FEL without the need for any optical components. This represents a considerable improvement in wavelength and timescales over any other methods currently available, and could be expected to drive forward new experimental opportunities in fundamental science. The simulation parameters used considered soft x-ray pulses similar to the LCLS-II, however, this is by no means the limit of the wavelengths available with this set up. Extrapolating from the simulations of a hard x-ray mode-locked afterburner as presented in [22], the same parameters adapted to generate alternating polarized pulses here would generate pulse separation times of 5 as, approximately one fifth of the atomic unit of time. Discussion of scaling the mode-locked afterburner to yet higher photon energies provided in [22] should also apply to the methods described here. Given the broad scaling of FEL wavelength operation, the method described will also be applicable to longer wavelengths, again opening up new experimental opportunities.

As well as operating across a broad range of wavelengths, the method could be adapted to meet other specific experimental requirements. The temporal shift between pulse trains of orthogonal polarizations may be controlled to bring alternating pulses close together followed by a longer time interval. The time duration of the different pulse types may also be altered by the length of the different types of undulators to generate pulse trains with a pulse of one polarization followed by a shorter pulse with the orthogonal polarization. However, it is noted that this will also result in different pulse powers and bandwidths which would need further consideration.

This method also provides a promising broader avenue to tailor FEL output and provide bespoke radiation for experiments. Further development of the method will include alternating other pulse properties such as the wavelength, e.g., using the work of [31], or orbital angular momentum of the pulses [32]. While experimental implementation of mode-locking has not yet been trialed, it may be advantageous to consider alternating pulse structure capabilities when upgrading FELs to include mode-locking.

ACKNOWLEDGMENTS

We are grateful to funding from the Science and Technology Facilities Council (Agreement Number 4163192 Release#3); ARCHIEWeSt HPC, EPSRC Grant No. EP/K000586/1; EPSRC Grant No. EP/M011607/1; John von Neumann Institute for Computing (NIC) on JUROPA at Jülich Supercomputing Centre (JSC), Project No. HHH20.

[1] N. Berova, P. L. Polavarapu, K. Nakanishi, and R. W. Woody, *Comprehensive Chiroptical Spectroscopy: Applications in Stereochemical Analysis of Synthetic Compounds, Natural Products, and Biomolecules* (John Wiley & Sons, New York, 2012), Vol. 2.

[2] U. Hergenhahn, E. E. Rennie, O. Kugeler, S. Marburger, T. Lischke, I. Powis, and G. Garcia, Photoelectron circular dichroism in core level ionization of randomly oriented pure enantiomers of the chiral molecule camphor, J. Chem. Phys. **120**, 4553 (2004).

[3] A. Kirilyuk, A. V. Kimel, and T. Rasing, Ultrafast optical manipulation of magnetic order, Rev. Mod. Phys. **82**, 2731 (2010).

[4] H. Rubinsztein-Dunlop *et al.*, Roadmap on structured light, J. Opt. **19**, 013001 (2017).

[5] S. Rozen, A. Comby, E. Bloch, S. Beauvarlet, D. Descamps, B. Fabre, S. Petit, V. Blanchet, B. Pons, N. Dudovich, and Y. Mairesse, Controlling Subcycle Optical Chirality in the Photoionization of Chiral Molecules, Phys. Rev. X **9**, 031004 (2019).

[6] G. Schütz, W. Wagner, W. Wilhelm, P. Kienle, R. Zeller, R. Frahm, and G. Materlik, Absorption of Circularly Polarized X-rays in Iron, Phys. Rev. Lett. **58**, 737 (1987).

[7] G. van der Laan and A. I. Figueroa, X-ray magnetic circular dichroisma versatile tool to study magnetism, Coord. Chem. Rev. **277–278**, 95 (2014), following Chemical Structures using Synchrotron Radiation.

[8] M. Suzuki, N. Kawamura, and T. Ishikawa, Application of optical scanner to switching of x-ray photon helicities at khz range, Rev. Sci. Instrum. **74**, 19 (2003).
[9] M. Först, C. Manzoni, S. Kaiser, Y. Tomioka, Y. Tokura, R. Merlin, and A. Cavalleri, Nonlinear phononics as an ultrafast route to lattice control, Nat. Phys. **7**, 854 (2011).
[10] T. Kampfrath, A. Sell, G. Klatt, A. Pashkin, S. Mährlein, T. Dekorsy, M. Wolf, M. Fiebig, A. Leitenstorfer, and R. Huber, Coherent terahertz control of antiferromagnetic spin waves, Nat. Photonics **5**, 31 (2011).
[11] J. Sánchez-Barriga, E. Golias, A. Varykhalov, J. Braun, L. V. Yashina, R. Schumann, J. Minár, H. Ebert, O. Kornilov, and O. Rader, Ultrafast spin-polarization control of dirac fermions in topological insulators, Phys. Rev. B **93**, 155426 (2016).
[12] J. D. Bull, N. A. Jaeger, H. Kato, M. Fairburn, A. Reid, and P. Ghanipour, 40-GHz electro-optic polarization modulator for fiber optic communications systems, in *Photonics North 2004: Optical Components and Devices*, Vol. 5577, edited by J. C. Armitage, S. Fafard, R. A. Lessard, and G. A. Lampropoulos, International Society for Optics and Photonics (SPIE, New York, 2004), pp. 133–143.
[13] Y. Yang, K. Kelley, E. Sachet, S. Campione, T. S. Luk, J.-P. Maria, M. B. Sinclair, and I. Brener, Femtosecond optical polarization switching using a cadmium oxide-based perfect absorber, Nat. Photonics **11**, 390 (2017).
[14] L. H. Nicholls, F. J. Rodríguez-Fortuño, M. E. Nasir, R. M. Córdova-Castro, N. Olivier, G. A. Wurtz, and A. V. Zayats, Ultrafast synthesis and switching of light polarization in nonlinear anisotropic metamaterials, Nat. Photonics **11**, 628 (2017).
[15] K. Holldack, C. Schüssler-Langeheine, P. Goslawski, N. Pontius, T. Kachel, F. Armborst, M. Ries, A. Schälicke, M. Scheer, W. Frentrup *et al.*, Flipping the helicity of x-rays from an undulator at unprecedented speed, Commun. Phys. **3**, 61 (2020).
[16] S. Serkez, A. Trebushinin, M. Veremchuk, and G. Geloni, Method for polarization shaping at free-electron lasers, Phys. Rev. Accel. Beams **22**, 110705 (2019).
[17] A. A. Lutman, T. J. Maxwell, J. P. MacArthur, M. W. Guetg, N. Berrah, R. N. Coffee, Y. Ding, Z. Huang, A. Marinelli, S. Moeller *et al.*, Fresh-slice multicolour x-ray free-electron lasers, Nat. Photonics **10**, 745 (2016).
[18] B. W. McNeil and N. R. Thompson, X-ray free-electron lasers, Nat. Photonics **4**, 814 (2010).
[19] R. Bonifacio, L. De Salvo, P. Pierini, N. Piovella, and C. Pellegrini, Spectrum, Temporal Structure, and Fluctuations in a High-Gain Free-Electron Laser Starting from Noise, Phys. Rev. Lett. **73**, 70 (1994).
[20] A. A. Lutman, J. P. MacArthur, M. Ilchen, A. O. Lindahl, J. Buck, R. N. Coffee, G. L. Dakovski, L. Dammann, Y. Ding, H. A. Dürr *et al.*, Polarization control in an x-ray free-electron laser, Nat. Photonics **10**, 468 (2016).
[21] N. R. Thompson and B. W. J. McNeil, Mode Locking in a Free-Electron Laser Amplifier, Phys. Rev. Lett. **100**, 203901 (2008).
[22] D. J. Dunning, B. W. J. McNeil, and N. R. Thompson, Few-Cycle Pulse Generation in an X-ray Free-Electron Laser, Phys. Rev. Lett. **110**, 104801 (2013).
[23] E. Hemsing, Coherent photons with angular momentum in a helical afterburner, Phys. Rev. Accel. Beams **23**, 020703 (2020).
[24] A. E. Siegman, *Lasers* (University Science Books, Mill Valley, CA, 1986), Vol. 37, p. 169.
[25] L. Campbell and B. McNeil, Puffin: A three dimensional, unaveraged free electron laser simulation code, Phys. Plasmas **19**, 093119 (2012).
[26] R. W. Schoenlein, New Science Opportunities Enabled by LCLS-II X-ray Lasers, SLAC National Accelerator Laboratory Tech. Report No. SLAC-R-1053, 2015.
[27] J. Clarke, J. Jones, and N. Thompson, A compact, modular electron beam delay line for use in novel free-electron laser schemes, Conf. Proc. C **1205201**, 1759 (2012).
[28] N. Thompson, XFEL isochronous chicanes: Feasibility study, in *Proc. FEL'19*, Free Electron Laser Conference No. 39 (JACoW Publishing, Geneva, Switzerland, 2019), pp. 658–660.
[29] D. Dunning, N. Thompson, P. Williams, and B. McNeil, Start-to-end simulations of SASE and hhg-seeded mode-locked FEL, in *Proceedings of FEL09 Conference, Liverpool* (2009), pp. 165–168.
[30] D. J. Dunning, B. W. J. Mc Neil, N. R. Thompson, and P. H. Williams, Start-to-end modelling of a mode-locked optical klystron free electron laser amplifier, Phys. Plasmas **18**, 073104 (2011).
[31] L. T. Campbell, B. W. J. McNeil, and S. Reiche, Two-colour free electron laser with wide frequency separation using a single monoenergetic electron beam, New J. Phys. **16**, 103019 (2014).
[32] E. Hemsing, A. Marinelli, and J. B. Rosenzweig, Generating Optical Orbital Angular Momentum in a High-Gain Free-Electron Laser at the First Harmonic, Phys. Rev. Lett. **106**, 164803 (2011).